Touchless Potential Sensing for Electrostatic Actuation in Cislunar Space

by

Kaylee Champion

B.S., University of Texas, 2021

M.S., University of Colorado, 2023

A thesis submitted to the

Faculty of the Graduate School of the

University of Colorado in partial fulfillment

of the requirements for the degree of

Doctor of Philosophy

Department of Aerospace Engineering Sciences

2026

Committee Members:

Prof. Hanspeter Schaub

Prof. Robert Marshall

Prof. Zoltan Sternovsky

Prof. Jade Morton

Dr. Vivek Dwivedi

Kaylee Champion, (Ph.D., Aerospace Engineering Sciences)

Touchless Potential Sensing for Electrostatic Actuation in Cislunar Space

Thesis directed by Prof. Hanspeter Schaub

Lunar exploration is in a period of expansion, with multiple nations launching missions and planing to return humans to the lunar surface and orbit. This increased activity raises concerns about orbital congestion, collision risk, and debris management. In addition, spacecraft orbiting the moon are exposed to highly variable plasma environments, increasing the risk of electrostatic discharges. Electrostatic actuation techniques proposed for Geosynchronous Earth Orbits applications can be extended to cislunar space to mitigate debris. To determine electrostatic forces, previously validated touchless potential sensing techniques can be used to determine the potential of a target debris object while also providing insight into discharge risk and lunar dust behavior.

Electron based touchless potential sensing methods have been analyzed in previous studies, and a key limitation is the difficulty in detecting electron emissions. Furthermore, interactions in the solar wind such as Debye shielding and barrier formations have not been considered. Simulation tools are used to generate strategies to increase the observability of electron emissions and characterize the impact of cislunar spacecraft-plasma interactions on touchless potential sensing. These results also benefit cislunar missions with instruments or components sensitive to the plasma environment.

Experimental methods to simulate flowing plasma and spacecraft wakes in the ECLIPS vacuum chamber are developed and used to validate a simple model of spacecraft wake formations around single and multiple spacecraft. Additional proximity interactions such as sheath overlap and electron emission recollection are shown to impact charging and electrostatic forces. Simplified approximations of the interactions are proposed to enable efficient charging analysis applicable to any system with multiple charged components.

Dedication

To Tony “Popo” Grones.

Acknowledgements

I would first like to thank my advisor, Dr. Hanspeter Schaub, for his support through this program. Thank you for pushing me to achieve at a high level and encouraging me in moments of doubt.

Thank you Dr. Álvaro Romero-Calvo for passing down invaluable knowledge during my first year and providing an example of a great scientist. Thank you to my committee, Dr. Robert Marshall, Dr. Zoltan Sternovsky, Dr. Jade Morton, and Dr. Vivek Dwivedi for the helpful feedback and support for this work.

I would also like to thank all the mentors I have been lucky to have through the NSTGRO fellowship, Mark Hasegawa, Jayne Griffin, Dr. Emily Willis, and Dr. Allen Andersen. I am a better researcher because of the opportunity I had to work with all of you. I am particularly grateful to my undergraduate research advisor, Dr. Srinivas Bettadpur. I would never have stumbled into this area of work without your support and wonderful mentorship.

I am especially grateful for the friends I have made through this program, both in the AVS lab and outside of it. The nights watching reality TV, camping, skiing, hiking, and playing games with you all have been the highlight of these last few years.

Finally, I want to thank my family for consistently supporting me and feeding my love of space. Thanks to Bevo, who stresses me out but also provides moments of entertainment and warmth. Most of all, I want to thank Karlie. Thank you for taking a leap of faith to Colorado and choosing to share your life with me.

Contents

Chapter

Tables

Table

Figures

Figure

Chapter 1

Introduction

1.1 Motivation

Enthusiasm for lunar and cislunar exploration is growing, as signaled by programs and missions like NASA's Artemis program [43], Intuitive Machine's Odysseus spacecraft, the Indian Space Agency's Chandrayaan spacecraft [130], the Chinese National Space Administration's Chang'E spacecraft [119], Russia's Luna missions [141], South Korea's Danuri orbiter, Japan's SLIM spacecraft [191], and dozens more missions planned in the coming years,[1] (Fig. 1.1). While this enthusiasm signals an exciting period of expanded lunar exploration, it also comes with increases in congestion around the Moon and therefore greater risk of collisions. As such, it is urgent and critical that opportunities to mitigate such risks are explored.

Cislunar space is typically defined as the region between GEO and the Moon, including the area immediately around the Moon's orbit. This is a large region; however, some lunar orbits are more desirable than others, including the near-rectilunar halo orbit (NRHO) planned for Lunar Gateway [63] and stable and quasi-stable frozen orbits in LLO [116, 146, 151]. In these orbits, congestion develops despite a lower number of satellites compared to those in LEO or GEO orbits. In fact, the Chandrayaan-2 spacecraft in a LLO has had to perform as least three collision avoidance maneuvers since entering orbit in 2022 to avoid the Lunar Reconnaissance Orbiter (LRO) and Danuri.[2] A simulation study indicates that a presence of just 10 satellites in LLO can lead to

[1] Fly me to the Moon
[2] Chandraayan-2 article

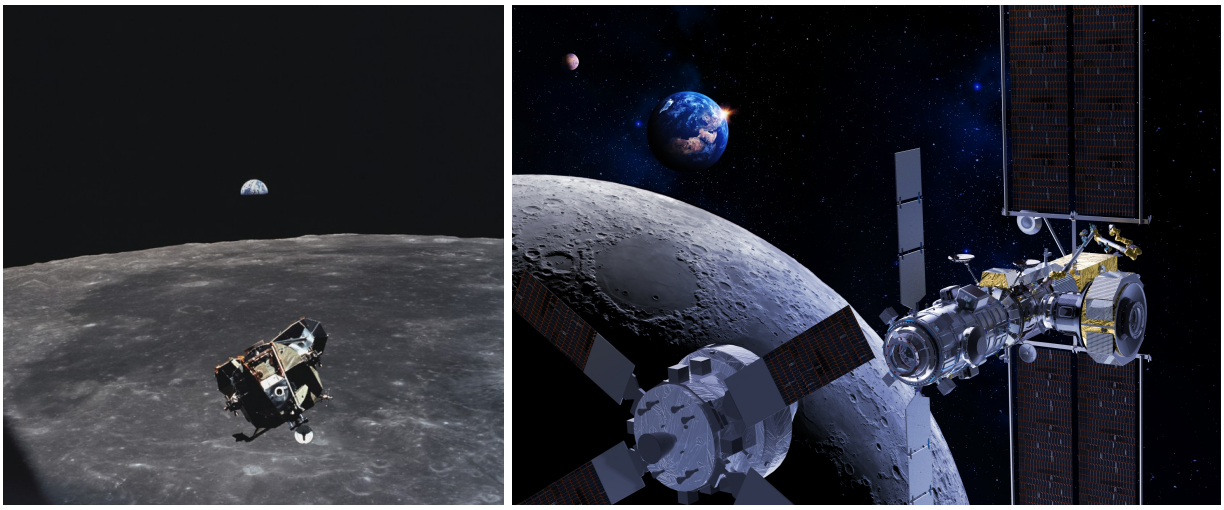

(a) Apollo 11 Eagle lunar landing module photographed by Michael Collins

(b) Orion docking with Lunar Gateway (credit: Thales Alenia Space/Briot)

Figure 1.1: Historic (left) and future (right) lunar missions

yearly collision avoidance maneuvers, approximately matching the three maneuvers in four year performed by Chandrayaan-2 [44].

To complicate collision avoidance, estimating the number of satellites and their locations in lunar orbit is a challenge for several reasons: there is not a cohesive catalog of spacecraft orbiting the Moon, complex cislunar orbits can make it difficult to predict trajectories, the bright glare from the Moon makes it difficult to visually detect objects (sometimes referred to as the "cone of shame"), and signals are difficult to detect from Earth [13, 15]. In fact, it is unknown if the Eagle Lunar Module Ascent Stage from Apollo 11 is still orbiting the Moon [138]. Without knowledge of the other objects orbiting the Moon, determining when a collision avoidance maneuver needs to be conducted becomes nearly impossible, and the risk of collisions increases. Plus, with no atmospheric drag to eventually de-orbit satellites in stable orbits, debris can persist indefinitely, amplifying the risk of damage to future spacecraft in a similar region [26, 28]. When debris does fall to the lunar surface, it is not slowed by atmospheric drag and impacts the surface faster than a bullet, endangering both manned and unmanned structures on the surface of the Moon.

Due to the difficulty of tracking objects in cislunar space and the unforgiving consequences

of a collision, lunar orbit debris must be prevented or safely managed. It should be noted that mitigating debris around the moon is not as straightforward as debris mitigation in Low Earth Orbit (LEO) or Geosynchronous Earth Orbit (GEO), where debris is deorbited and burned up in the atmosphere or re-orbited to a prescribed graveyard orbit, respectively. As a result, there are not yet guidelines for End-of-Life (EOL) disposal strategies for Moon orbiting spacecraft, several methods to manage lunar debris are under investigation. One method, particularly for Low Lunar orbit (LLO) objects is to deorbit the spacecraft in a controlled manner such that they impact a pre-determined zone on the surface of the moon such as a designated "graveyard crater" [5, 27]. Another option is to move spacecraft to a new cislunar graveyard orbit. For example, on of the proposed disposal strategies for the Lunar Gateway station is to transfer it to a Distant Retrograde Orbit (DRO) [137]. Another option is to transfer the spacecraft to a heliocentric orbit that will not intercept Earth or Moon orbits. This option is likely viable for spacecraft stationed around an Earth-Moon Lagrange point [8, 144]. Last, the spacecraft can be set on an Earth reentry trajectory, but this can require significant fuel and poses a risk to spacecraft in GEO and LEO orbits [144].

Active debris removal and relocation concepts that could be applied to cislunar spacecraft include laser ablation [177], momentum transfer using ion beams [104], and capture using nets [70, 176], harpoons [53], or tethers [11]. Most of these concepts involve making contact with the debris or using impulsive forces, which risks collisions between the uncontrolled, potentially spinning target and controlled servicer. In contrast, touchless methods protect the integrity of the servicing and target spacecraft. One such proposed touchless servicing methods utilizes spacecraft charging.

Spacecraft interact with the plasma and radiation environment in space, charging and developing a surface potential. Two charged spacecraft then exert an electrostatic force on each other, which can be used to touchlessly maneuver debris. Higher levels of charging, and larger electrostatic forces, can also be actively induced using an electron beam. Investigations of electrostatic actuation have largely taken place in hot, sparse plasma environments such as GEO, Medium Earth Orbit (MEO), and interplanetary space [9, 18, 23, 81, 91, 92, 96, 103, 123, 162, 170].

Spacecraft charging can have negative consequences, as electrostatic discharges (ESD) on

conductive surfaces, within surface dielectrics, or between two docking spacecraft can damage components and is the leading cause of spacecraft anomalies due to the space environment [106]. Charged spacecraft can also exert unexpected electrostatic forces and torques on each other during proximity operations, which introduces unexpected perturbations that can require extra maneuvers and fuel to counteract [208]. In the cislunar regime, a lunar lander contaminated with regolith can contaminate the Moon-orbiting vehicle it docks with. The surface potential of the ascending lander influences the lunar dust trajectories and contamination danger, as is shown with simulations of the Human Lander System docking with the Lunar Gateway [118]. To determine the electrostatic forces during electrostatic actuation, avoid arc discharges during docking, and conduct analysis of lunar dust contamination, the potential of the nearby target object can be determined using various touchless potential sensing methods.

While electrostatic actuation and touchless potential sensing methods have been significantly investigated, translating this technology to the cislunar plasma environment is not trivial. The Moon's ambient plasma changes as the Moon orbits the Earth, and spacecraft-plasma interactions that occur in dense, flowing plasma have not been considered when investigating the technologies of interest. In this work, outstanding questions relevant to electrostatic actuation and touchless potential sensing are addressed, and spacecraft-plasma interactions unique to the cislunar environment are characterized to determine if and how this technology could be applied to address safety and science goals around the Moon.

1.2 Background and Previous Work

1.2.1 Cislunar Plasma

The Moon orbits through Earth's magnetosphere and out into the flowing solar wind, passing through a range of plasma environments. Several missions have helped characterize the cislunar plasma environments, including the Apollo missions [4, 66, 215], the Wind spacecraft [148], the Lunar Reconnaissance Orbiter (LRO) [192], and the twin Acceleration, Reconnection, Turbulence,

Table 1.1: Cislunar regions mean characteristic parameters [117]

Region	$\mathbf{n_e}$ $\mathbf{(1/m^3)}$	$\mathbf{T_e}$ **(eV)**	$\mathbf{v_i}$ **(km/s)**	$\mathbf{n_i}$ $\mathbf{(1/m^3)}$	$\mathbf{T_i}$ **(eV)**	$\lambda_\mathbf{D}$ **(m)**
Magnetotail Lobes	2.0E5	48	170	2.0E5	290	115.2
Plasmasheet	2.2E5	150	110	2.0E5	780	194.1
Magnetosheath Dayside	9.5E6	18	350	8.0E6	94	10.2
Solar Wind Dayside	6.0E6	11	420	6.0E6	7	10.1
Solar Wind Wake 100 km - 500 km	7.3E4	6	260	8.1E4	320	213.1
Solar Wind Wake 600 km - 2000 km	5.5E4	160	650	6.5E4	1400	127.5
Solar Wind Wake 2000 km - 12000 km	1.1E6	29	370	1.1E6	130	38.2
Solar Wind Wake >12000 km	2.5E6	19	400	3E6	66	20.5

and Electrodynamics of the Moon's Interaction with the Sun (ARTEMIS) spacecraft [7]. Measurements from the ARTEMIS spacecraft are analyzed and binned in the Design Specification for the Natural Environment (DSNE) document produced by NASA [117], which identifies four plasma regions: solar wind, magnetosheath, magnetotail lobes, and plasma sheet. The average parameters in these regions in shown in Table 1.1, and a further discussion of the environments is presented in Section 3.2.

The solar wind is the plasma flowing from the sun and is located outside of Earth's magnetosphere with the interplanetary magnetic field [97, 147]. The plasma sheet is a region of hot plasma in the Earth's magnetotail that magnetically maps to the auroral oval and splits the magnetotail into its top and bottom lobes. The plasma sheet mainly consists of accelerated solar wind and can contain ionospheric ions when there is significant magnetospheric activity [14]. The magnetotail lobes are located within the magnetopause and mainly consist of plasma outflow from the ionosphere [74, 100]. The magnetosheath is the transition region between the solar wind and magnetotail located between the bow shock and magnetopause [127]. The regions and interactions of Earth's magnetosphere and the cislunar environment are an active area of research; interested readers are referred to Refs. [29, 64, 155] for a more thorough review. Figure 1.2(a) depicts these regions using figures of the Moon with respect to Earth's magnetic field. The magnetic field is shown in blue and solar wind in light brown. In addition to orbiting through several regions, the Moon alters the plasma environment. In the solar wind and magnetosheath, the Moon absorbs and

reflects plasma, leaving a low density, complex structure on the eclipse side of the Moon, known as the lunar wake (Fig. 1.2(b)) [79].

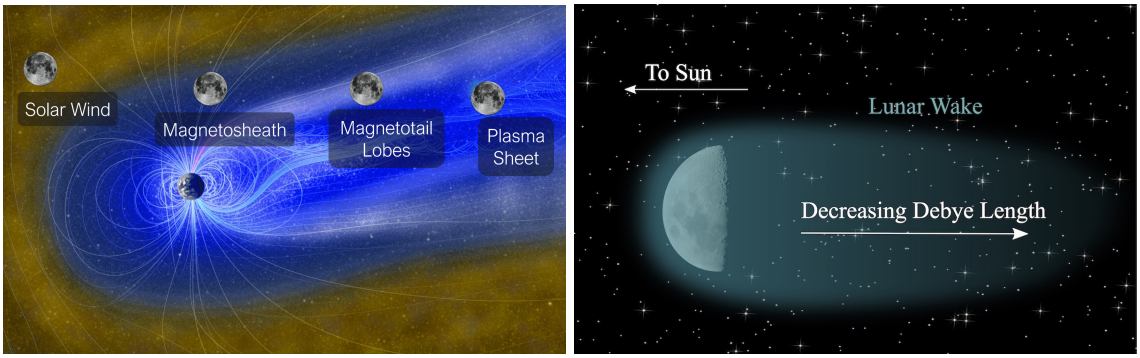

(a) Cislunar Environments (Moon not to scale) (b) Lunar wake

Figure 1.2: Lunar plasma environments and interactions

Due to the different sources of plasma and interactions in each region, the magnetotail lobes and plasmasheet contain high-energy, low-density plasma, similar to the GEO environment, while the magnetosheath and solar wind consist of lower-energy, denser plasma compared to the GEO-like environments. It is in these latter environments that interactions not previously considered for touchless potential sensing or electrostatic actuation studies occur, including short Debye lengths, spacecraft wakes, and nonmonotonic sheaths.

1.2.2 Spacecraft Charging and Electrostatic Actuation

Interactions between spacecraft, energetic plasma, and the radiation environment generate surface currents and potentials. The magnitude of a spacecraft surface's potential is dependent on its geometry, material properties, and sunlit area [65, 110]. Thus, two spacecraft or electrically disconnected surfaces in the same environment can charge differently, leading to a risk of arc discharges as previously discussed. In fact, approximately 40% of satellite missions that end prematurely due to the space environment are terminated as a result of an electrostatic discharge [106]. To mitigate this, it is advised that all spacecraft surfaces are electrically connected to prevent differential charging; however, this is not always possible due to factors such as frayed electrical connections,

resistive surface materials such as radiative paints, and exposed solar panel components that can lead to differential charging [158]. Arcing during docking procedures is also a risk, particularly if one spacecraft is in the shadow of the other because eclipsed spacecraft typically charge more negative than sunlit craft due to the lack of photoelectron emissions and ion flux [134, 198, 201]. For example, simulations of Lunar Gateway docking with Orion indicate that a potential difference of over 9 kV can occur between the two bodies [134].

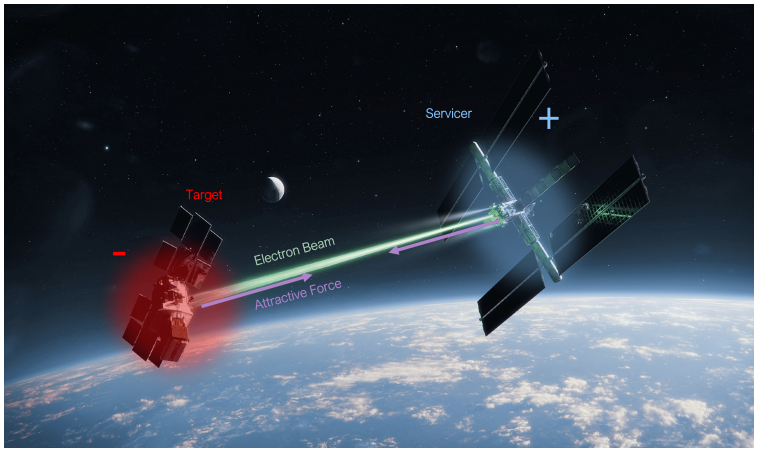

Figure 1.3: Electrostatic Tractor Concept

Spacecraft charging has been a subject of research since the beginning of the space age, with Sputnik 3 taking the first measurements of its own potential (-6.4 V at 795 km altitude) [107]. Other spacecraft missions such as Spacecraft Charging at High Altitudes (SCATHA) and the SPEAR-1 rocket payload have induced charging through electron beam emissions and biasing of components [102, 109, 111]. The concept of induced charging has been proposed to enable touchless electrostatic applications such as moving space debris [18, 81, 91, 92, 96], detumbling a target [10, 21, 22, 34], inflating thin structures [181], enabling close proximity coulomb formation flying [9, 23, 103, 123, 162, 170], and hovering above a charged body in space [16, 154]. In this work, electrostatic actuation is implemented through the electrostatic tractor concept (Fig. 1.3). During electrostatic tractor operations, a servicing spacecraft is equipped with an electron beam that is aimed at a target. By emitting electrons, the servicer charges itself positively, and by impacting

the target with electrons, the target ideally charges negatively. It is possible for the electron beam to generate more electron emissions than the number of impacting electrons, which can charge the target positively. To ameliorate this, charge control methods have been investigated to charge the target to a desired, likely negative, potential [194]. The resulting attractive electrostatic force is then used to touchlessly maneuver the target. Spacecraft typically charge within milliseconds to seconds, depending on their geometry and the ambient plasma. Therefore, the electrostatic tractor requires continuous beam impacts to maintain the potentials generated. The electrostatic tractor has been extensively investigated for application in GEO space [18, 81, 91, 96, 168, 169, 171] and within spacecraft wake formations in LEO space [131–133].

Electrostatic actuation studies typically prescribe potentials to the spacecraft or utilize charging equations to determine the surface potentials that can form. The presence of a highly charged object changes the ambient plasma environment, and therefore the charging behavior of other nearby objects. This has previously been shown in complex spacecraft-plasma interaction software, but these simulations can take hours to days to complete. It would therefore be beneficial to characterize the changes in current during electrostatic actuation operations when highly charged objects are near each other and generate simple approximations that can be used in analytic surface charging calculations. Chapter 6 presents approximations of these interactions and their impact on charging, with some of the interactions validated with experiments enabled in Chapter 5.

1.2.3 Touchless Potential Sensing

Before electrostatic actuation can be implemented, the potential of the other spacecraft involved must be known to determine the electrostatic forces. Several techniques exist to touchlessly determine the potential of a surface from varying separation distances. Ferguson et al. [61] proposes using ground- surface material glow, bremsstrahlung X-ray emissions, and radio and optical emissions from arcs to estimate surface charging and arcing behavior of spacecraft in GEO from ground or Low Earth Orbit. Lunar Probe Electron Reflectometer data is utilized to study the energy dependent electron loss cone and secondary electrons accelerated from the lunar surface to determine

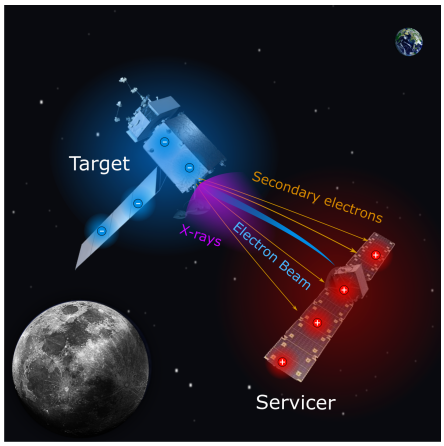

(a) Secondary electron and X-ray method

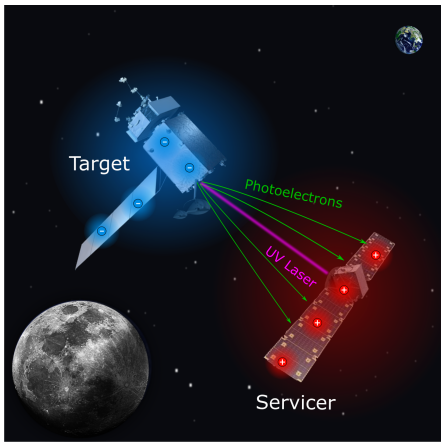

(b) Secondary electron and photoelectron method

Figure 1.4: Active potential sensing concepts using an electron beam and VUV laser

the difference in potential between the lunar surface and spacecraft at kilometers of separation [76–79, 153]. In experiments, technologies such as as non-contact voltmeters, scanning electron microscopes,[3] and electrostatic probes are utilized to contactlessly determine surface potential at separation distances of millimeters to centimeters [3, 86, 115, 163]. For electrostatic actuation and determining the risk of arcing or lunar dust contamination during docking, the potential of the spacecraft should be determined from tens of meters. To implement this, three methods have been investigated: secondary electron (SE), photoelectron (PE), and X-ray.

To determine the potential of a target using secondary electron emissions, an electron beam is aimed at the surface of interest to generate secondary electrons that leave the surface with a continuous energy distribution up to the energy of the impacting electron, but the majority of emissions are generated with an energy of a few electron-volts. If the target is charged negatively, the secondaries are then repelled and accelerated to an energy approximately equal to the target's surface potential V_T. If the servicer is charged positively, the electron emissions are attracted and further accelerated by the servicer's surface potential V_S such that once the emissions reach

[3] As a general overview, in Ref. [86], the contrast in images generated scanning electron microscope (SEM) measurements from a distance of μm are first calibrated for varying potentials on a measured surface, then utilized to determine the surface's potentials.

the servicer, their energy is approximately equal to the difference in potential between the two spacecraft ($V_S - V_T$). The photoelectron method is similar to the secondary electron method, except a vacuum ultraviolet (VUV) laser is used to generate photoelectron emissions instead of secondary electron emissions from the surface. The low energy photoelectrons again reach the servicer with an energy approximately equal to the difference in spacecraft potentials.

An electrostatic analyzer (ESA) type instrument can be used to measure the energy of the emissions. Electrostatic analyzers are frequently used on spacecraft missions to determine the energy distribution of charged particles [112, 210]. For example, the SPAN top-hat ESA instrument on Parker Solar Probe is capable of sweeping through a distribution of electrons in less than a second with 10% to 20% energy resolution [101] and the top-hat ESA instrument on the THEMIS-ARTEMIS spacecraft can sweep through a distribution in less than a second with an energy resolution of 15% to 20% [136]. A retarding potential analyzer (RPA) has been used in touchless potential sensing experiments and has been flown on several missions including New Horizons with a 1% resolution for 1 keV particles [135] and the Pioneer Venus Orbiter with a 20% to 30% resolution from 0-50 eV [105]. The servicer can also determine its own potential using existing technology such as RPAs [112], electron spectrometers [67], and electric field double probes [173]. Once the potential of the servicer and difference in potentials is known, the target's potential can be determined. It should be emphasized that while new technology does not have to be developed from scratch for touchless potential sensing, limitations in the instruments such as low acceptance angles for top-hat ESAs and small maximum energy measurements for RPAs will likely need to be addressed to implement this technology.

The energy of the electron beam is also altered as it traverses from the servicer to the target. The beam is attracted to the servicer and loses energy equal to the servicer's potential upon being emitted. Then, the beam is repelled from the negative target and again loses energy equal to the target's potential. Thus, when the beam lands on the target, its energy E_{land} is equal to the initial energy of the beam E_b minus the difference in potential between the spacecraft ($E_b - V_S + V_T$). If the beam is not more energetic than the difference in potentials, it will be deflected and not

impact the target. In addition to generating secondaries, high energy impacting electrons can also generate bremsstrahlung radiation, or stopping radiation. As the electrons enter the material, they can be deflected about atoms and lose energy, which is emitted as a Bremsstrahlung radiation X-ray photon. Through this process, the X-ray photons are emitted with a range of energies up to the landing energy of the impacting electrons. Therefore, if the maximum energy of the X-ray emissions is measured using an X-ray sensor, the potential difference between the two spacecraft can again be determined, leading to the target's potential being solved for. However, the X-ray signal at the maximum energy is too weak and noisy to be deciphered because a small number of photons are emitted at the maximum energy and photons with energies near the maximum value are largely emitted in directions pointing away from the incident electron direction (which typically means the photons are not emitted towards the servicer). To determine the maximum energy, the distribution of X-ray energies are measured, fit to the theoretical energy distribution for bremsstrahlung X-ray emissions, and the resulting y-intercept is the approximate maximum energy [80, 202, 207]. X-ray sensors have been flown extensively on spacecraft [69, 108, 129, 172] and have been proposed to image the magnetosphere [30, 42].

The methods described are active potential sensing scenarios where equipment is used to generate the emissions for sensing. SEs, PEs, and X-rays can all be generated naturally by the plasma and radiation environment, which can then be used to passively sense the potential of the spacecraft. The passively emitted signal is generally lower, and in some cases the signal may be too low to distinguish from the plasma and/or radiation environment; however, there are scenarios when it is still be feasible to sense among the ambient plasma and radiation environment [17, 126, 206]. In addition, passive sensing of electron emissions can be used to determine the surface potential of the target, but passive sensing of X-rays can only be used to determine the relative change in potential of the target. Because the energy of plasma electrons is a spectrum, the X-ray spectrum is difficult to fit for determining the target's potential; however, if the target charges negatively the emitted radiation can be diminished. The change in X-ray photon measurements, coupled with measurements of the ambient plasma, can then be used to track changes in target potential [205].

Table 1.2: Comparison of active sensing methods

Method	Advantages	Disadvantages
Secondary Electrons (SEs) from electron beam	- Most accurate (10s of V) - Favored by low-energy electron beams	- Large beam deflections - Detectability dependent on system geometry and potentials
X-rays from electron beam	- Detectability weakly dependent on system geometry - Less deflection of high energy beam - Reduced influence of surface contamination	- Less accurate (100s of V) - Requires energetic electron beams - X-ray sensor can saturate
Photoelectrons (PEs) from VUV Laser	- Most accurate (10s of V) - Laser not deflected - Observable and controllable	- Generally, lower emitted current - Cannot charge servicer positively - Detectability dependent on system geometry and potentials

Passive sensing is useful if the servicer is not equipped with an electron gun or VUV laser but has of the instruments that can be used to detect emissions, or if the target spacecraft is active and impacting it with an electron beam could create unwanted charging.

The touchless potential sensing methods have been verified in experiments and have varying benefits and challenges, as shown in Table 1.2. SEs and PEs allow for the most accurate estimation of the target's potential (within 10s of Volts), while X-ray emissions have errors of the order of 100 Volts [205]. X-ray emissions favor higher energy electron beams and can be detected as long as the electron beam impacts the target [80, 205], but electron emission trajectories are highly dependent on the target geometry and can only be detected at a fraction of positions about the object. In addition, SE emissions favor low energy electron beams that are more susceptible to deflection by the electric field about the spacecraft. Around a uniformly charged target, secondaries have been detected at ≈10% of relative locations in vacuum chamber experiments [19, 160]. VUV lasers are not deflected by the ambient electric field, so PE emissions have been detected at ≈20% of relative locations in experiments with a uniformly charged target [159]. Detecting electron emissions becomes even more difficult once differential potentials arise, as the changing electric field suppresses electron emissions and alters the emission trajectories [20, 160].

The low observability of electron emissions is the limiting factor for touchless potential sensing using electron emissions. Previous work has characterized electron trajectories about objects of varying shapes [20], compared and combined sensing processes using SE and X-ray emissions [205],

and revealed that differential potentials on a spacecraft can prevent electron emissions from leaving a target's surface [160]. However, strategies to actively increase the observability of a target's electron emissions have not been investigated. Chapter 2 presents an investigation into the observability of secondary electron and photoelectron emissions about a target and strategies to actively emit and detect these emissions.

Furthermore, previous studies have assumed that the plasma environment can be negated, which can be an appropriate assumption in GEO and similar environments, but, as mentioned in Section 1.2.1, the presence of dense, flowing plasma in the solar wind and magnetosheath environment presents new interactions that may be beneficial or detrimental to touchless potential sensing and cannot be neglected. Therefore, Chapters 3 and 4 characterize these interactions to determine the feasibility of and trends in touchless potential sensing.

1.3 Summary of Contributions

The overarching purpose of this research is to create further insight into the emission and charging behavior of spacecraft in cislunar space and strengthen the capabilities of touchless potential sensing and electrostatic actuation. To implement this, outstanding questions relevant to touchless potential sensing and electrostatic actuation are addressed, and the impact of dense flowing plasma on these concepts is evaluated.

The goals of this dissertation are summarized as follows:

(1) Touchlessly determine the potential of a nearby target using electron emissions in changing environments

   (a) Improve the observability of electron emissions, particularly around complex geometry and differentially charged spacecraft (Chapter 2)

   (b) Determine how to appropriately model the potential field in cislunar solar wind and the impact of short Debye lengths on touchless potential sensing (Chapter 3)

(c) Characterize barriers from nonmonotonic sheaths, wakes, and electron beams and their impact on sensing operations (Chapter 4)

(2) Address proximity interactions during charging

(a) Develop vacuum chamber wake experiments to validate wake behavior during sensing and charging operations (Chapter 5)

(b) Simulate electrostatic actuation charging behavior and generate approximations for multi-body behaviors that can be implemented in charging equations (Chapter 6)

Chapter 2

Touchless Potential Sensing of Complex Shapes and Differential Potentials

2.1 Motivation

The methods for touchless potential sensing (secondary electron (SE), photoelectron (PE), and x-ray) present different advantages and disadvantages. Namely, the SE and PE methods enable the highest accuracy measurements, with errors on the order of ten volts in prior experiments while the x-ray method has an accuracy on the order of 100 Volts. Conversely, x-ray emissions have been detected anytime the electron beam has impacted a side of the target not facing away from the detector, while the electron emissions used for the SE and PE methods may only be detected at a limited number of locations around a target. In this chapter, the *observability* of a target is defined as the fraction of relative positions in which emissions can be detected. So, the observability of the SE and PE emissions is a limiting factor for these methods regardless of the plasma environment. This is particularly evident when the target's geometry has several components or differential potentials arise. Therefore, strategies to improve the observability of electron emissions are investigated.

Previous work has characterized electron trajectories about objects of varying shapes [20], compared and combined sensing using SE and x-ray emissions [205], and revealed that differential potentials on a spacecraft can prevent electron emissions from leaving a target's surface. For example, a solar panel more negatively charged than the main body of a target is shown to deflect electron emissions from the main body back into the surface of the target, preventing the servicer from detecting the electrons [160]. To build off of this work, validated sensing models

from Refs. [159, 160] are implemented in a SIMION model with spacecraft on the order of meters separated by tens of meters during touchless sensing operations. The impact of relative positions, changes in potentials, and differential potentials on observability are first investigated. Then, emission equipment, specifically an electron gun and VUV laser, are implemented to determine how the equipment should be manipulated to excite detectable emissions. This is the first comprehensive analysis of how equipment and configurations can be tailored to more consistently detect electron emissions in a realistic, high-potential environment.

This chapter first provides an overview of how a servicer and target are modeled in SIMION. Then, electron emissions are generated across the main body of the target, and the spacecraft potentials and positions are varied to investigated how changing these parameters impacts the measured electron emissions and if a strategy for positioning the servicer can be developed. Last, an electron beam and VUV laser are inserted in the simulation, and the impact of the equipment parameters on signal is studied to determine how the equipment should controlled to increase the chance of generating observable electron emissions.

2.2 Modeling Approach

2.2.0.1 SIMION

SIMION[1] is a charged particle trajectory software package utilized to investigated charged beam and electron emission trajectories in electrostatic fields. Matlab is employed to configure the PA geometry, launch the SIMION simulation, and analyze the results through the use of Window's batch files. This implementation allows several SIMION setups to be defined and automatically run with minimal interference. This is useful for investigating the behavior of the electron beam or electron emissions efficiently over a large range of parameters.

SIMION computes the trajectory of each charged particle from Newton's second law

$$\frac{\mathrm{d}\mathbf{v}}{\mathrm{d}t} = \frac{q}{m}\mathbf{E}, \tag{2.1}$$

[1] SIMION webpage

where $\mathbf{v}$, q, and m are respectively the particle velocity, charge, and mass, $\mathbf{E}$ is the electric field, and t is the time. Relativistic corrections are implemented when v^2/c^2 exceeds 10^{-10}, with c being the speed of light. The electric field is derived from the electrostatic potential field V as

$$\mathbf{E} = \nabla V, \tag{2.2}$$

while V is computed by solving Laplace's equation

$$\nabla^2 V = 0 \tag{2.3}$$

in the simulation domain. SIMION employs a Cartesian mesh, and the electric field boundary conditions are determined by a constant potential (Dirichlet) or constant electric field (Neummann). The components potentials can be individually adjusted in SIMION, and the additive property of the Laplace equation is utilized to determine the potential field, which is saved as a **potential array** (PA).

Electron emissions are not available by default in SIMION and are implemented by means of Lua user defined functions. These functions appropriately inject electron emissions into the simulation when a surface is impacted by electrons or representative VUV photons. Previous work presents detailed descriptions of the emission process, validation against experimental results, and related SIMION particle tracing simulation for SEs [160] and PEs [159], which is implemented in this work. There are several tools available to study charged particle interactions and emission behavior that have built in emission models, such as Geant4[2], CASINO[51], and Penelope[2] ; however, the goal of this work is not fundamental analysis of electron or x-ray emissions. The focus is on efficiently analyzing the trajectory of particles through potentials field for sensing or other experimental purposes. Therefore, SIMION is the most appropriate tool for investigations in this work in which the particle trajectories are of interest without including full-scale plasma dynamics.

[2] Penelope webpage

2.2.1 Potential Array Generation

To appropriately model the potential field around a spacecraft in a plasma environment, the boundary must be defined sufficiently far away such that the boundary conditions do not significantly impact the potential field calculations. In space environments, the appropriate distance is often defined by the Debye length λ_D. In other words, a Dirichlet boundary condition (constant potential on the boundary) of 0 V is defined approximately λ_D from the spacecraft. In hazardous charging environments, such as GEO and the cislunar plasmasheet and magnetotail lobes regions, the Debye length ranges from ≈100 m to several hundred meters based on parameters from [50, 117, 158]. To properly define the spacecraft components, elements on the order of centimeters are required, but defining a computational space with a width of several hundred meters using centimeter sized elements is computationally inefficient. Therefore, a *fine potential array (PA)* with a resolution of centimeters is defined within a *coarse PA* with a resolution of meters, as shown in Fig. 2.1. The internal fine PA captures the nearby potential field due to the geometry of the system and the boundary conditions are defined based on the potential distribution solution in the coarse PA, while the outer, coarse PA captures the decay of the electrostatic potential field.[3]

In the fine PA, spacecraft are defined according to their geometry (Fig. 2.1(a)). To generate the entire electrostatic field with elements on the order of a few meters, the spacecraft are defined in the coarse PA as spheres with equivalent self capacitance as the spacecraft models (Fig. 2.1(b)), referred to as effective spheres. The self capacitance C of the spacecraft is found using the Multi-Sphere Method (MSM)[95, 179, 180], and the radius R_{eff} of the effective sphere is

$$R_{\text{eff}} = \frac{C}{4\pi\epsilon_0}, \tag{2.4}$$

where ϵ_0 is the permittivity of free space.

The size of the fine PA is variable to optimize computational efficiency without sacrificing accuracy. The boundary is defined to be approximately 3 spacecraft widths from the complex geometry models because the electrostatic environment surrounding complex spacecraft shapes can

[3] See SIMION `field_emission` example available with the software for further discussion of a fine PA nested within a coarse PA.

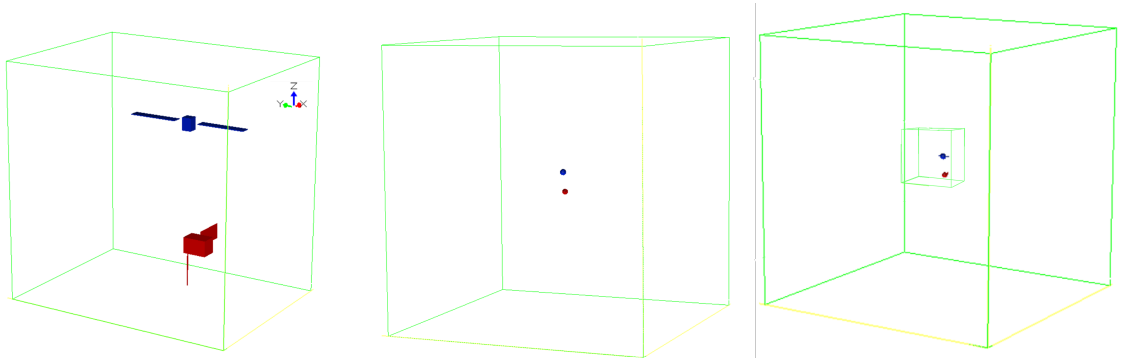

(a) Fine PA (b) Coarse PA (c) Initialization

Figure 2.1: SIMION spacecraft fine and coarse PAs, and an initialization of the fine PA in the coarse PA.

be approximated with an effective sphere if the distance is larger than 2 to 3 craft radii [99, 168]. The width of the spacecraft is defined using the longest end-to-end distance of the spacecraft (typically tens of meters) to ensure changes in attitude do not decrease the distance from the spacecraft surface to the fine PA boundary.

The target's position and attitude in the fine PA is held constant to keep the target's surfaces aligned with the Cartesian PA elements. In SIMION, misalignment with the PA elements results in jagged surfaces that may alter the SE and PE trajectories. To further improve accuracy, the electrode surface enhancement feature is utilized in both the coarse and fine PA, which allows electrode points to be defined in partial grid units and can improve the accuracy of the potential field by at least an order of magnitude[4] .

The simulation is initialized with the fine PA positioned such that the spacecraft and their effective spheres in the coarse PA are in the same position, as shown in Fig. 2.1(c). The potential field surrounding the spherical, charged spacecraft is first solved throughout the entire coarse PA to characterize the general potential field decay. The potential field values from the coarse PA at the location of the fine PA boundary are then assigned as Dirichlet boundary conditions on the individual fine PA boundary elements, and the potential field due to the spacecraft geometry in the

[4] See SIMION `surface_enhancement` example available with the software.

fine PA is resolved. In addition, the effective spheres are set to 0 V and moved such that they are in contact with a corner of the coarse PA to prevent the spheres from influencing the final particle trajectories. Now, the charged particles can be initialized and their trajectories simulated.

2.2.2 Mesh Independence Analysis

Analysis is conducted to ensure that the results are consistent independently of the resolution of the mesh. In other words, the mesh size does not change the results of the simulation. In this analysis, the servicer is based on the SSL-1300 spacecraft, and the target is based on the GOES-R spacecraft. The SSL-1300 model consists of a 2.5 x 2.5 x 3 m cube main body and two 12.1 x 2.3 x 0.4 m solar panels. The GOES-R model consists of a 4 x 4 x 6 m main body, an 8.3 x 4 x 0.4 m solar panel, and an 8.3 x 0.4 x 0.4 m boom. These spacecraft are not intended to exactly match the SSL-1300 and GOES-R spacecraft, only to serve as a general representation of spacecraft that may be found in GEO and cislunar space. The radii of the spheres with equivalent capacitance to the models are 4.80 m for SSL-1300 and 4.44 m for GOES-R.

The servicer can be equipped with an electron gun or VUV laser and are assumed to have aluminum surfaces. For this setup, the Sanders and Inouye SE yield model is used to define the secondary electron yield as a function of beam energy. The maximum yield δ_{max} and energy at maximum yield E_{max} are set at 0.97 and 300 eV, respectively, based on the values for aluminum [110]. A photoelectron emission effective yield of 0.058 and reflectance of 0.85 for the VUV laser defined in Section 2.4 are implemented [62, 159].

The element size is halved, or the resolution is doubled, until the solution is altered less than 10% by increasing the resolution. This is done for a separation distance of 20 m between a -4 kV servicer and -13 kV target with the servicer's electron beam pointing directly at the target's body. An electron beam energy of 11 keV is utilized, and the number of secondaries impacting the 2.5 x 2.5 m side of the servicer's body facing the target is recorded. Table 2.1 shows the results of the mesh independence analysis along with the final element and boundary sizes.

Table 2.1: Mesh Independence Analysis

Parameter	**Initial Size**	**Initial Run Time**	**Final Size**	**Final Run Time**	**Detected SE Percent Difference**
Final PA element size	20 cm	20 s	40 cm	10 s	5%
Coarse PA element size	1 m	40 s	2 m	10 s	8%
Boundary distance	400 m	40 s	200 m	10 s	3%

2.2.3 Differentially Charged Spacecraft

Modeling spacecraft with differential potentials introduces another level of complexity to the SIMION simulations because the singular sphere used to determine the coarse PA cannot be used to represent multiple potentials. To resolve this, representative spheres of each component of the spacecraft are generated and utilized for the coarse PA. The GOES-R model represents the target in this project, so the solar panel and boom can charge independently of all other components. The representative spheres have radii of 2.96 m, 2.49 m, and 1.21 m for the main body, solar panel, and boom, respectively. The spheres are then placed at the center point of the component's location, and the coarse PA and fine PA are resolved as previously described. To ensure that this is appropriate, a potential of -13 kV is set for all components of the target and -4 kV for the servicer, and the simulation described in the previous section is repeated. It is found that the detected secondaries remain the same, validating that discretizing the spheres in the coarse PA is appropriate for modeling differential potentials.

2.2.4 Environmental Considerations

The spacecraft-plasma interactions are not included in SIMION; however, the interactions with the ambient space environment in GEO and the cislunar plasmasheet or magnetotail lobes show that this model is appropriate. As previously mentioned, the external boundaries are located approximately a Debye length (≈200 m) from the spacecraft. The separation distances investigated in this project are less than 20 m, approximately an order of magnitude less than the Debye length. Therefore, Debye shielding is considered a secondary effect and can be neglected.

The gyroradius, or the radius of the circular motion of a non-relativistic charged particle in

a magnetic field, is

$$r_g = \frac{v_\perp m_e}{q_e B} \tag{2.5}$$

where $v_\perp$ is the velocity perpendicular to the magnetic field, m_e is the mass of an electron in kilograms, q_e is the elementary charge, and B is the magnetic field strength in Teslas. The thermal velocity of an electron is

$$v_\perp = v_e = \sqrt{\frac{2k_B T_e}{m_e}}, \tag{2.6}$$

where k_B is the Boltzmann's constant and T_e is the electron temperature. The geomagnetic field in GEO orbit is 100 nT, resulting in gyroradii of 100–3000 m for electron energies from 10 to 10^4 eV assuming the electron velocity is entirely perpendicular to the magnetic field [160]. The field in the plasmasheet may be on the order of 20 nT [139], resulting in gyroradii of 355-11000 m for for electron energies from 10 to 10^4 eV. This is again larger than the maximum separation distance and is considered a secondary effect.

The distance at which particles travel between collisions is characterized by the mean free path λ_{mfp}. The mean free path of particles in a Maxwellian plasma is [124]

$$\lambda_{\text{mfp}} = \frac{48\sqrt{6/\pi} N_D \lambda_D}{\ln(9N_D)}, \tag{2.7}$$

where N_D is the Debye number, or the number of particles in a sphere with radius equal to the Debye length

$$N_D = \frac{4}{3}\pi n_e \lambda_D^3, \tag{2.8}$$

where n_e is the electron number density. The mean free path in GEO is approximately 3.5E5 km for worst case GEO data, and is approximately 2.7E9 km for mean plasma sheet characteristics [117]. Therefore, assuming a collisionless, vacuum model is appropriate in these environments.

2.3 Servicer Relative Position

2.3.1 Simulation Setup

The trajectories of electron emissions are highly dependent on the target's geometry. In general, there are regions about a target in which electron emissions can penetrate, while there may be other regions the emissions are deflected from. This alters the fraction of positions around the target in which the servicer can intercept electron emissions trajectories, which as a reminder is referred to as the *observability* in this work. In general, the servicer must also detect enough current to resolve the target's potential. In plasma, the current must be distinguishable from the plasma electrons. For more insight into the magnitude of current required, see Chapter 4, which investigates if currents in select sensing scenarios are large enough to distinguish from the plasma environment. Regardless, the *changes* in measured electron emissions or methods to more consistently detect electron emissions from a target is the focus of this chapter. The emission trajectories around various spacecraft geometries have previously been investigated [17], and it has been shown that the emission trajectories are independent of the target's potential if the target is uniformly charged [205]. However, these simulations did not include a servicing spacecraft or a differentially charged target. Therefore, the impact of varying servicer and target potentials or differential potentials on the observability without the inclusion of an electron gun or VUV laser is first characterized. In other words, positioning the servicer in a location around the target where it is possible to intercept electron emissions is the first step to determine the target's potential using these emissions. Therefore, this sections investigates how changing the spacecraft potentials and positions changes the measured electron emissions when electrons are generated uniformly from the main body of the target. This creates results independent of the electron beam and VUV laser parameters, and the ways in which the emission equipment should be altered is investigated in Section 2.4.

In this section, low energy electron emissions are generated uniformly over the main body of a target spacecraft. SE emission energies can be modeled using the Chung-Everhart probability

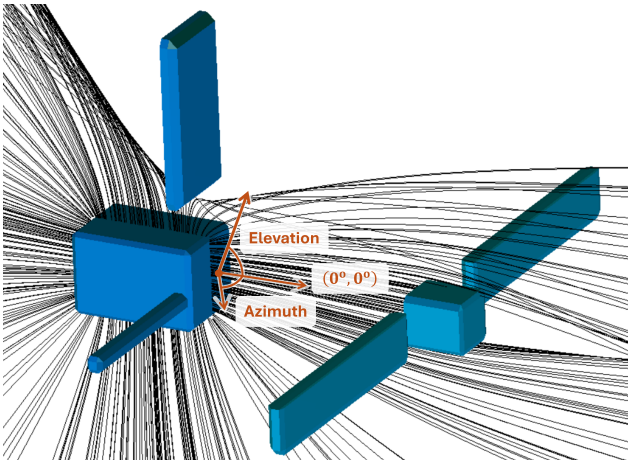

Figure 2.2: Vertical cut-view of electron emission trajectories (black) between the target (left) and servicer (right), and the azimuth and elevation coordinates implemented in this work.

density function, with a peak at one third the work function of the material [41], and PE emission energies are typically between 1-3 eV [113]. Aluminum is assigned as the surface material of the target with a work function of 4 eV [121], so the representative electron emissions are initialized with an energy of 1.3 eV. An example of a vertical cut-view of the electron emissions is shown in Fig. 2.2. Because the electrons are generated across the entire body of the target, there is not a direct correlation between the number of particles impacting the servicer and the detected current. Therefore, the results are presented in this section with units the number of particles detected by the servicer, not current.

The servicer and target are modeled at a constant center-to-center separation distance of 15 m. In each assigned servicer-and-target surface potential, the servicer is moved through all possible azimuth and elevation angles, $\pm 180°$ and $\pm 90°$, respectively, in $10°$ steps while facing the center of the target for a total of 703 runs in SIMION for each setup. This is equivalent to the targeting rotating through all positions near a stationary servicer. The target's solar panel is aligned with the $90°$ elevation axis, and the boom is aligned with the -90° azimuth axis, as shown in Fig. 2.2. The number of electrons impacting the surface of the main body of the servicer facing the target is recorded, and the servicer is considered to have detected electron emissions when at least one particle impact is recorded.

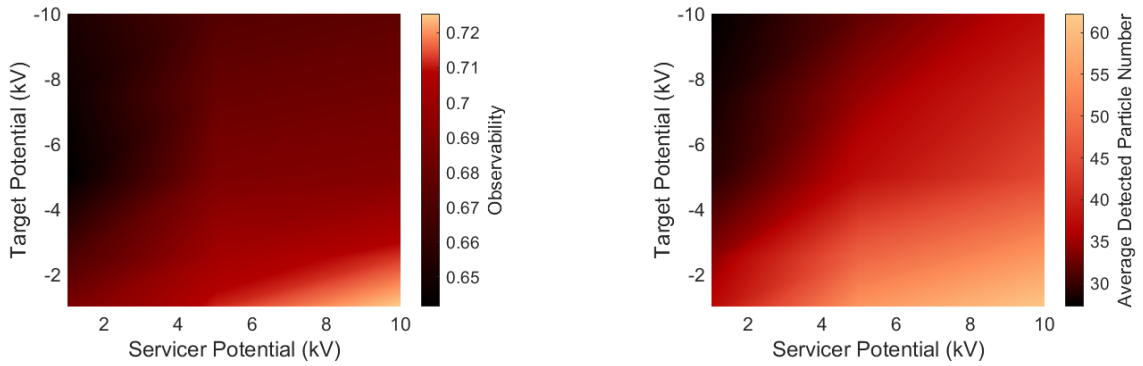

(a) Fraction of locations in which electron emissions are observable

(b) Average detected particle count

Figure 2.3: The fraction of locations particles are detected around the target (left) and average number of particles detected (right).

2.3.2 Uniform Servicer and Target Potentials

To explore the effect of a charged servicer, the potential of the servicer and target are tested at 1, 2.5, 5, 7.5, and 10 kV and -1, -2.5, -5, -7.5, and -10 kV, respectively, at all relative positions for a total of 9,063 runs.

The observability, which is again the fraction of positions around the target in which the servicer can intercept electron emissions trajectories, shown in Fig. 2.3(a), is generally higher for a more positive servicer and lower for a more negative target, with the highest observability for a -1 kV target and 10 kV servicer and the lowest observability for a -10 kV target and 1 kV servicer. This occurs because the electron emissions are accelerated by the negatively charged target, making them less susceptible to the electric field generated by the servicer's more positive surface potential. Despite this, the fraction of observable locations only varies between 0.67 and 0.75, a 12% change between the worst and best case, which indicates that the spacecraft potentials do not significantly change the emissions trajectories. This presents both pros and cons for touchless potential sensing. Unfortunately, biasing a servicer more positively does not significantly increase the observability of a target. However, the regions in which electron emissions should be expected from a uniformly charged target can be determined for one set of servicer and target potentials and reliably utilized

to set keep in and keep out zones for a servicer during touchless potential sensing operations. This also means that if the spacecraft potentials change during electrostatic actuation operations the location of the servicer about the target can be kept the same and it should continue to detect electron emissions. The regions in which electron emissions can be detected varies for different spacecraft geometry, so this must be determined for specific spacecraft missions.

Fig. 2.3(b) shows the average number of particles detected when the target is observable. This is representative of the average signal the servicer receives when it can detected emissions from the target. This is determined summing the number of particles detected for a servicer-and-target surface potential configuration and dividing by the number of times in which the servicer detects current. As a reminder, the number of detected particles is recorded for 703 servicer positions around the target for every servicer-and-target surface potential configuration. If the servicer detects more than one particle emitted from the target in a setup, this is included in the number of times the servicer can detect a current from the target. The average number of detected particles increases nearly linearly with servicer and target potential. This combined with the observability results indicates that the general zones in which the servicer can detect electron emissions remains stable, but a more positive servicer can draw in nearby electron emissions to increase the strength of the signal. This conclusion only holds when the emission current remains the same, as would be expected when actively emitting electrons or detecting naturally emitted PEs. When sensing passively emitted SEs, previous work has shown that increasing the servicer's potential can significantly *decrease* the SE emissions from a target [35]. This will also be discussed more in depth in Chapter 3.

2.3.3 Differential Target Potentials

It is shown that biasing the servicer more positive does not significantly change the target's observability. However, a differentially charged target is expected to alter the electron trajectories and thus the observability. To explore this, the potential of the target's solar panel and boom are individually varied from -33 kV to 7 kV (±20 kV with respect to the main body) in 10 kV

steps, for a total of 25 surface potential combinations. The target's main body is held at -13 kV, and the servicer is held at -4 kV for all simulations. These values are selected based on the surface potentials expected when Lunar Gateway and Orion dock [134]. This range of positions and differential potentials results in a total of 17,575 simulations in SIMION.

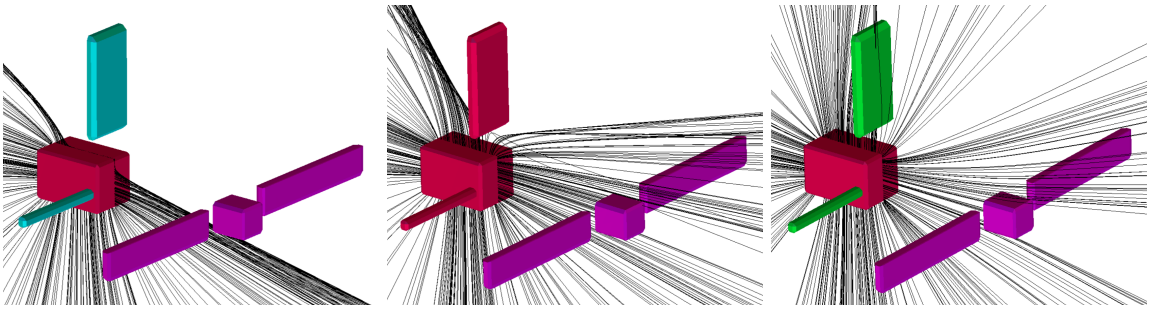

(a) -23 kV components (b) -13 kV components (c) -3 kV components

Figure 2.4: Vertical cut-view of electron trajectories (black) between a target (left) with variable component potentials and a servicer (right).

Nascap-2k simulations completed in Ref. [60] predict maximum differential charging up to 20 kV in GEO substorm conditions. It is likely that if differential potentials of this magnitude occur, arc discharges or dielectric breakdown would occur and work to resolve the potential difference. Therefore, 20 kV differential potentials serves as a bounding case for what may be expected in GEO-like plasma environments.

Figure 2.4 shows vertical cut-views of electron emissions from the main body of the target with varying component potentials. The electron emissions from the uniformly charged target (-13 kV components) are deflected by the solar panel and boom. The negatively biased solar panel (-23 kV components) exacerbates this effect by suppressing electron emissions such that they are reflected back into the surface of the target. This effectively decreases the total emitted current from the main body and further limits the regions in which electron emissions can reach a servicer. Alternatively, if the components are biased more positively than the main body (-3 kV components), the electrons are attracted towards the components. This widens the regions emissions pass through, increasing observability. It should be emphasized that the target's components only need to be

biased positively with respect to the main body, not with respected to zero in order for the emissions to be attracted towards the component.

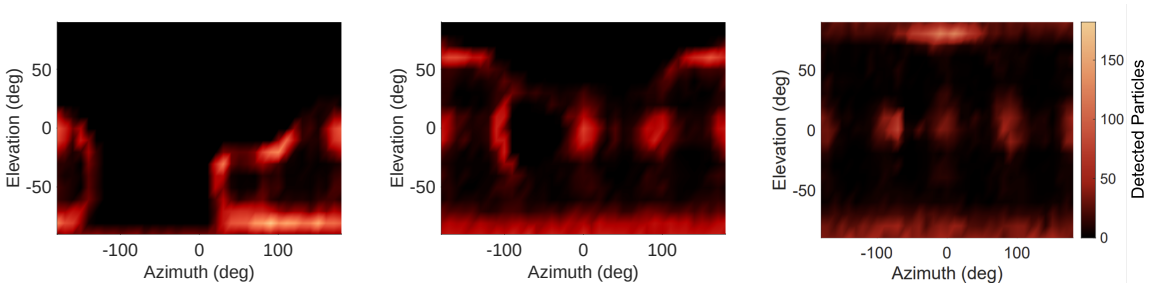

(a) -33 kV components (b) -13 kV components (c) 7 kV components

Figure 2.5: Number of electron emission particles detected by a -4 kV servicer at various locations around a target with a -13 kV main body.

The detected particles for three of the twenty-five simulated target surface potentials are shown in Fig. 2.5. For the uniformly charged target (-13 kV components), it is best to be parallel to the flat surfaces of the main body and maximize the distance from extruding components to the servicer. When both components are negatively biased (-33 kV components), the electrons are repelled at such a magnitude that it is no longer beneficial for the servicer to be parallel to a flat surface of the target. In this case, the servicer should instead prioritize maximizing the distance from the components to the servicer. Furthermore, the concentration of electron emissions is largest for the most negative components, despite the fact that some of the electron emissions are deflected back into the surface of the target. In other words, the negative components act as a focusing mechanism, which can increase the detected electron emissions current. Conversely, when both components are positively based (7 kV components), it again becomes beneficial for the servicer to position itself parallel to the flat surface. However, the optimal positions are near the components, not farther away, and the magnitude of particle impacts is lower in nearly all detectable regions.

These results indicate that if a target is differentially charged, the regions in which electron emissions can be detected is no longer consistent. Fortunately, there may be regions in which

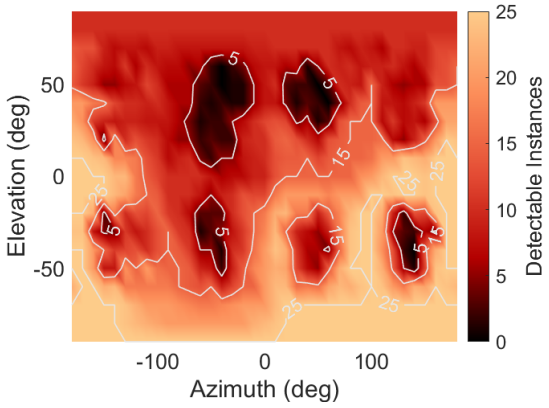

Figure 2.6: Number of times the servicer is able to detect electron emissions at each tested location, noted as detectable instances on the colorbar, when varying potentials are set on the target's solar panel and boom. 25 differential target potentials are tested, so 25 instances indicates the servicer detects electrons for all tested differential potentials at the defined position.

electron emissions are more likely to be detected despite differential potentials. Figure 2.6 shows the number of target surface potential combinations, referred to as instances in the color bar, in which electron emissions can reach the servicer at each location. If 25 detectable instances occur at a specified azimuth and elevation, then emissions can be detected for all target differential potentials tested. There are 25 detectable instances in the locations surrounding ≈130° azimuth and -40° elevation. In this area, the servicer is near the corner of the target's main body opposite of the servicer and boom. This effectively shields the electron emissions from the target component's electric field, allowing the servicer to detect emissions regardless of differential potentials. Electron emissions are also consistently detected around 180° azimuth with 0° elevation and -90° elevation, when the servicer is parallel to faces of the target that are also shielded from the components. This then leads to a relatively simple strategies to detect electron emissions from a spacecraft that may have differential potentials; the servicer should increase the distance between the possibly differentially charged components and itself. This may be feasible for scenarios in which the servicer is free to move to all relative locations about a target, such as electrostatic actuation operations. In other scenarios, such as docking, in which the servicer should remain near the docking port, the servicer can approach the target in a region with a larger number of detectable instances.

Table 2.2: Equipment parameters

Parameter	**Electron Beam**	**VUV Laser**
Energy (E_B)	1 to 30 keV	7.7 eV
Current (I_B)	1 μA	N/A
Flux (f_{ph})	N/A	9.7E14 photons/s
Deflection Angle (γ)	-2° to 2°	-2° to 2°
Half Angle (ϕ)	0.2° to 2°	0.2° to 2°

The appropriate servicer locations about the target varies with target geometry and must be evaluated for specific target geometry. It is also possible for unexpected differential potentials to form on the target, which can deflect electrons away from a region previously considered reliable for detecting electron emissions. To increase the reliability of sensing despite differential potentials, the servicer can sweep through relative positions until electron emissions are detected, or x-ray emissions can be used to determine the surface potential with a higher uncertainty until electron emissions are detected. Preliminary results indicate that combining the x-ray method with SE or PE emissions can decrease sensing time and increase observability [37, 193, 205], and combining multiple sensing strategies with guidance controls is recommended for future work.

2.4 Electron Emission Equipment Parameters

2.4.1 Simulation Setup

Positioning the servicer about the target so that electron emissions can be detected is the first step to accurately determining the target's potential; however, the electron beam or VUV laser is not expected to fully envelop the target. As a result, even if the servicer is in the correct position, it is possible for the beam or laser to miss the region where emitted electrons reach the servicer, referred to as a *source region*. Previous experiments have not investigated how changing the electron beam or VUV parameters can be manipulated to find a source region. Therefore, the impact of equipment parameters, shown in Table 2.2, on detected electron emission current from a uniformly charged target is investigated to determine how the equipment can be manipulated to impact a source region. Once the best-case equipment parameters are define, the servicer is moved in the

same manner as described in Section 2.3.1 to quantify the change in observability with different equipment parameters. Last, differential potentials are defined on the target to investigate how the source region and emission equipment performance may change.

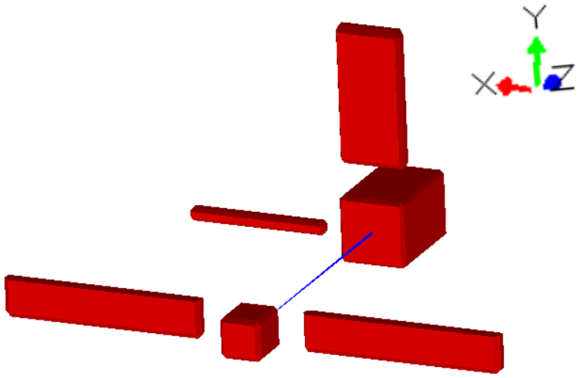

Figure 2.7: Electron beam trajectory with no deflection.

In this section, the servicer is held at an azimuth and elevation of 0°. If there is no deflection, the electron beam and VUV laser impact the center of the target's body, as shown in Fig. 2.7. It should be noted that the VUV laser itself likely cannot alter its deflection angle or half angle, and it is assumed that an external setup, such as a movable platform or opaque cover, is capable of changing these parameters. In Section 2.3.3 it is shown that, in this location, electron emissions can reach the servicer for nine of the twenty-five surface potential combinations: when the components are equipotential with the main body or more positively charged.

The beam current, VUV laser photon flux, and VUV laser energy is held constant in this section. For charging purposes, changing the beam current can change the potential of the spacecraft. The effect of the beam current on the charging process is discussed in Chapter 6, and it is shown that a beam current of 1 μA is expected to minimally change the potential of a target of a similar size to the target spacecraft used here in most average cislunar plasma environments. For sensing purposes, increasing these values increases the electron emission current. Because the focus of this section is evaluating how the equipment parameters changes the detected current, the amount of current detected does not change the conclusions and the listed parameters are held

constant. This also means that the currents presented are not representative of the entire range of currents that can be expected during sensing operations. The current required to distinguish the electron emission current from the plasma electrons is investigated in Chapter 4.

2.4.2 Uniform Target Potential

2.4.2.1 Singular Position

Figures 2.8 and 2.9 show the detected SE current as a function of the electron beam parameters and detected PE current as a function of the VUV laser parameters, respectively. For both, the maximum current is detected when the deflection angle is +2° in the x and y direction. The x and y-axes are defined the same as previously shown in Fig. 2.7, so this deflection directs the beam towards both the boom and solar panel. The SEs and PEs generated on this corner of the target body are repelled by the boom and solar panel into the face of the servicer, making this the *source region* for this uniformly charged servicer-target orientation. As the deflection angles strays from the source region, the detected emission current decreases regardless of other parameters. Therefore, an appropriate deflection angle must be achieved, or emissions will not be detected.

Increasing the half angle of the equipment increases the probability that at least part of the beam impacts the source region, therefore increasing the observability. In fact, when the half angle of the VUV laser's beam is 2°, current is detected at every deflection angle except -2° in the x and y direction. It should be considered that for a wider beam only part of the beam impacts the source region, decreasing the detected current. In the range of half angles explored, the order of magnitude of the maximum detected emission current remains the same, but the detected current is expected to decrease as the half angle increases. This effect can be accounted for by increasing the beam current, minimizing the landing energy to increase the SE current, or increasing the VUV laser energy to increase PE current. Once the source region is determined with a wide beam, the half angle could also be decreased to increase the detected current.

Minimizing the landing energy increases the number of deflection angles at which SE current

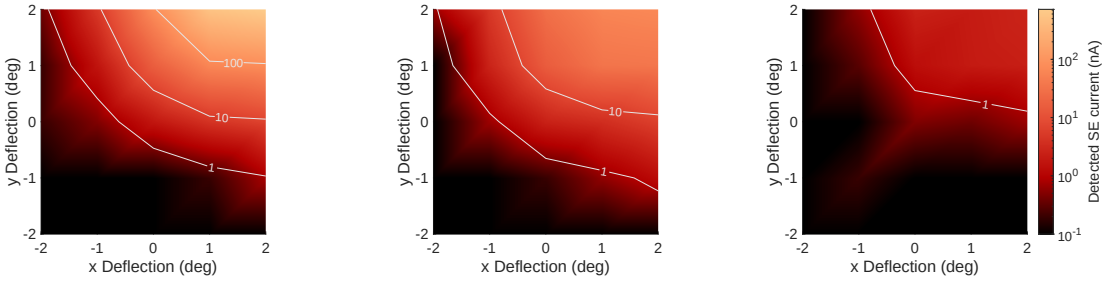

(a) E_B=10 kV, E_{land}=1 kV, ϕ=0.2° (b) E_B=14 kV, E_{land}=5 kV, ϕ=0.2° (c) E_B=18 kV, E_{land}=9 kV, ϕ=0.2°

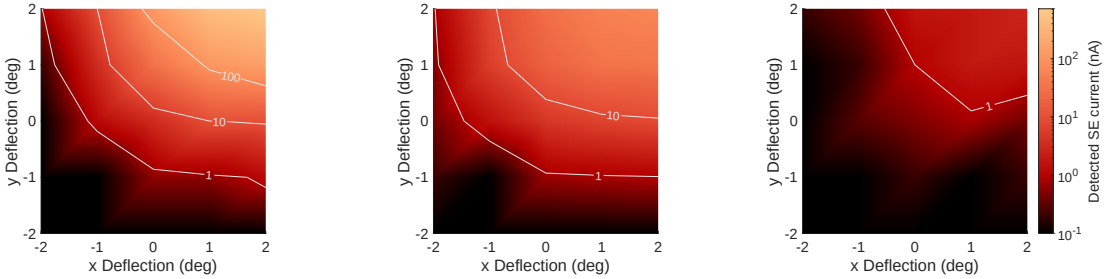

(d) E_B=10 kV, E_{land}=1 kV, ϕ=1° (e) E_B=14 kV, E_{land}=5 kV, ϕ=1° (f) E_B=18 kV, E_{land}=9 kV, ϕ=1°

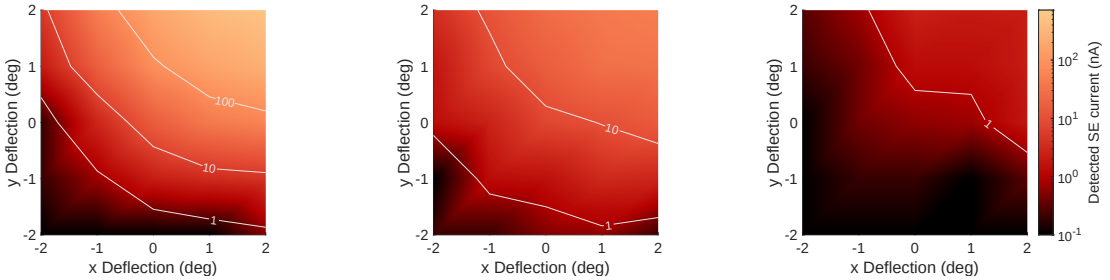

(g) E_B=10 kV, E_{land}=1 kV, ϕ=2° (h) E_B=14 kV, E_{land}=5 kV, ϕ=2° (i) E_B=18 kV, E_{land}=9 kV, ϕ=2°

Figure 2.8: Detected secondary electron current in nA for uniform spacecraft potentials.

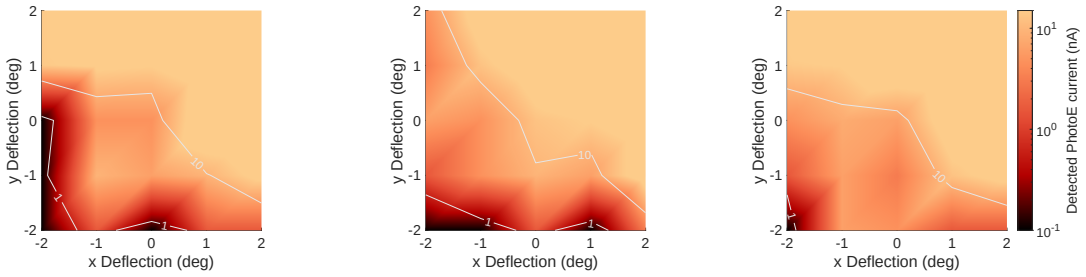

(a) ϕ=0.2° (b) ϕ=1° (c) ϕ=2°

Figure 2.9: Detected photoelectron current in nA for uniform spacecraft potentials.

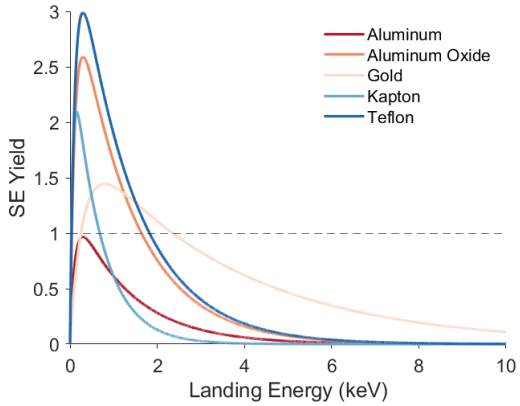

Figure 2.10: Secondary electron yields for common spacecraft surface materials.

is detected. This is surprising because higher energy beams are less deflected by the electric field about the charged spacecraft and would be expected to more reliably impact the source region. However, SE emissions favor low energy impacting electrons, with the energy at which the maximum yield occurs E_{max} typically around a few hundred electron volts. Figure 2.10 shows the Sanders and Inouye SE yield model as a function of landing energy for materials commonly used on spacecraft [110, 165]. As shown, once the landing energy exceeds E_{max} the yield decreases, and at approximately 5 keV the yield is minimal for most of the example materials. Raising the beam energy ≈5 keV does not significantly change the trajectory in the electric field of these high potential spacecraft, so the beam energy cannot be raised to decrease deflection within the energy range that significant SEs are emitted. Therefore, the focus should be to minimize the beam energy to increase SE yield. This could be achieved by first using x-ray emissions to obtain a rough estimate of the target's surface potential then determining an appropriate beam energy for SE emission. Otherwise, the beam energies must be swept through until sufficient SEs are emitted. Because the VUV laser is not deflected by the ambient electric field, changing the flux or photon energy does not change where the VUV laser impacts, and these parameters are analogous to the electron beam current.

2.4.2.2 Variable Positions

The beam and VUV laser are maintained at a constant half angle of 2° and deflected until at least 10 nA of current is detected or all deflection angles are tested at each servicer and target location. The electron beam maintains an energy of 10 keV, and current of 1 μA. There are 25 possible deflection angles tested at 703 servicer positions, for another 17,575 SIMION simulations for both the electron beam and VUV laser.

When using the electron beam, sufficient current is detected at 128 positions when the beam is not deflected and 242 positions when the beam is deflected. When using the VUV laser, sufficient current is detected at 133 positions without deflection and 241 positions with deflection. This represents a 90% and 81% increase in observability with the electron beam and VUV laser, respectively. In other words, the number of positions the servicer can determine the target's potential nearly *doubles* when the emission equipment is deflected.

The observability about the uniformly charged target is nearly the same with both the electron gun and VUV laser, regardless of the deflection of the equipment. Therefore, both options are viable for detecting the potential of a uniformly charged target.

2.4.3 Differential Target Potentials

Now, the electron beam and VUV laser maintain a half angle of 2°, the deflection angle is varied, and energy of the electron beam is swept through while the servicer and target remain at 0° azimuth and elevation and the target's is prescribed the same differential potentials set in Section 2.3.3. As a reminder, emissions can be detected for nine of the twenty-five differential potential combinations at this location. SE emissions are detected for four of the possible nine surface potential combinations, regardless of beam energy, again indicating that increasing the beam energy does not increase the observability of electron emissions about a target. The four surface potential combinations that allow electron emission detection only include a solar panel or boom that are equipotential or 10 kV more positive than the main body. Outside of this range, the

electron beam is deflected such that it does not impact the source region. Conversely, PE emissions are detected for all nine of the possible potential combinations, meaning full observability has been achieved. Because the VUV laser is not deflected by the ambient electric field, if there is a source region, the laser is capable of hitting it. The VUV laser is therefore more reliable than the electron beam when detecting the potential of a differentially charged target.

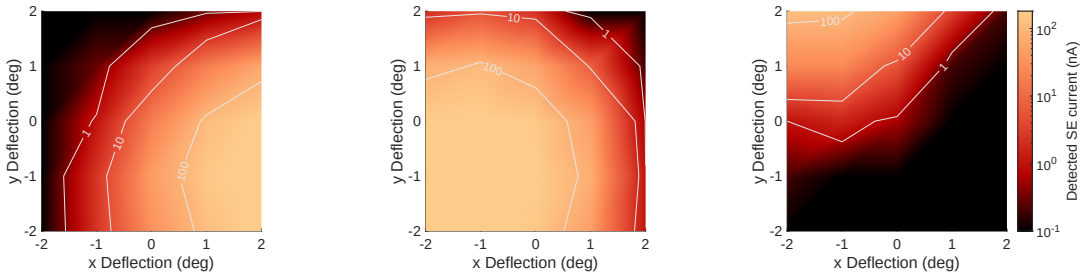

(a) -13 kV boom, -3 kV SP (b) -3 kV boom, -3 kV SP (c) -3 kV boom, -13 kV SP

Figure 2.11: Detected secondary electron current in nA for differential spacecraft potentials.

The detected currents from a differentially charged target for a 10 keV beam and the VUV laser are shown in Fig. 2.11 and 2.12, respectively. When the components are biased positively with respect to the main body, the source regions moves *away* from the components to counteract the attractive force. Conversely, if the component is equal to or more negative than the main body, the source region moves *towards* it to it to counteract the repulsive force. This means that the electron beam and VUV laser cannot be repeatedly directed towards the same position on the target to emit detectable electrons if differential potentials occur. Conversely, if the source region is different than expected, it can be concluded that a nearby component is biased more positive if the source region moves farther from it or more negative if the source regions moves closer to it. This simplifies detection of differentially charged components, as the electron gun and VUV laser can be deflected to search for the component based on the change in source region. In addition, insight into the potential magnitude of a nearby component can be achieved without directly detecting it. Since a VUV laser is not deflected by the ambient electric field and may create a spotlight on the target, it is likely simpler to determine what component is differentially charged using the VUV laser.

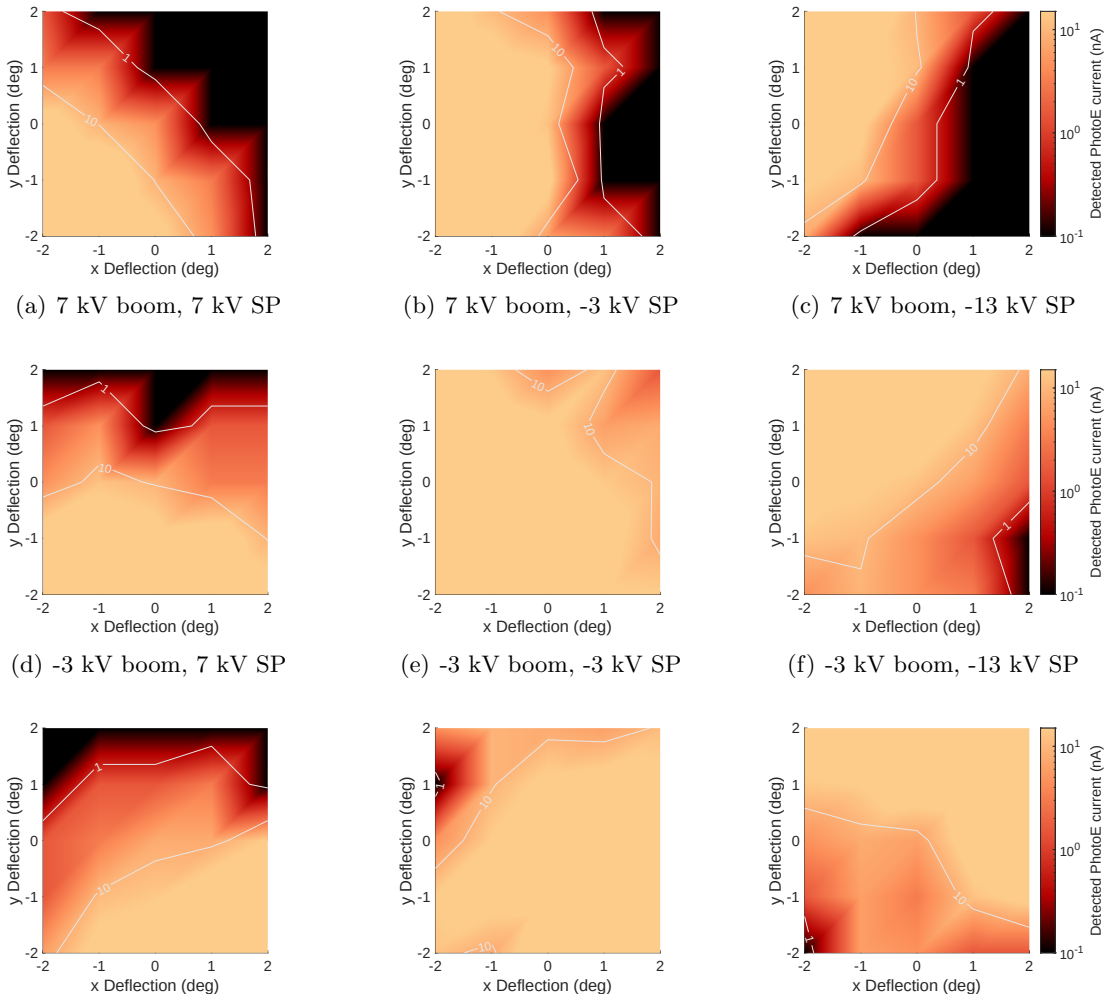

(a) 7 kV boom, 7 kV SP (b) 7 kV boom, -3 kV SP (c) 7 kV boom, -13 kV SP

(d) -3 kV boom, 7 kV SP (e) -3 kV boom, -3 kV SP (f) -3 kV boom, -13 kV SP

(g) -13 kV boom, 7 kV SP (h) -13 kV boom, -3 kV SP (i) -13 kV boom, -13 kV SP

Figure 2.12: Detected photoelectron current in nA for differential spacecraft potentials.

2.5 Conclusion

Novel strategies to increase the observability of electron emissions for touchless spacecraft potential sensing, particularly in the presence of differential charging, are investigated. It is found that biasing the servicer more positive increases the strength of the signal, but not necessarily the observability. About a uniform target, the electron emission trajectories are consistent in the presence of changing servicer and target potentials, allowing the regions in which emissions are detectable to be predetermined and integrated into spacecraft guidance controls, such as those

developed in [203]. If differential potentials develop on a target, the electron emission trajectories are no longer consistent. In this case, if there is prior knowledge about which component may be electrically disconnected and charged differently than the rest of the spacecraft, the servicer can increase the distance between the component and itself. The x-ray method can also be used to determine the target's potential with a lower resolution until electron emissions are detected.

Through extensive particle tracing simulations in SIMION, it is shown that observability can be nearly doubled by widening the electron beam or VUV laser and varying their deflection angle. In addition, the energy of the electron beam should be minimized to maximize the SE yield. Notably, the electron beam and VUV laser achieve comparable improvements in observability about a uniformly charged target, despite their different physical characteristics. Around a differentially charged target, the electron beam cannot reliably be utilized to detect the target's potential due to beam deflection while the VUV laser continues to reliably impact source regions. Furthermore, differentially charged components change the source region in predictable ways, allowing for the relative potential of a nearby component to be determined without direct detection.

Chapter 3

Electrostatic Potential Shielding During Touchless Potential Sensing

3.1 Motivation

Following the investigation of touchless potential sensing of complex shapes and differential surface charging, cislunar spacecraft-plasma interactions are considered. In this chapter, Debye shielding of the spacecraft potential is examined. As mentioned in the previous chapter, the Debye length is a measure of the distance over which a charge particle's electrostatic effect reaches in a plasma, and touchless potential sensing and electrostatic actuation operations are proposed for a separation distance of 10 to 30 meters [91, 168]. Thus, a Debye length of less than approximately 30 meters is considered short. For touchless potential sensing applications, a short Debye length limits the sphere of influence of a positive servicer, which limits the spacecraft's ability to pull in electron emissions from a target. This can decrease the separation distances possible for touchless potential sensing. For electrostatic tractor operations, a short Debye length significantly reduces the Coulomb force between two charged spacecraft, reducing the effectiveness of touchless re-orbiting or servicing processes for spacecraft at the same potentials and separation distance. A lower electron temperature and higher electron density can lead to a "short" Debye length, which is expected in the solar wind and magnetosheath regions based on Table 1.1.

Fortunately, it has been shown previously that an *effective* Debye length several times larger than the natural Debye length can better represent the sphere of influence of a charged particle. Effective Debye lengths have been investigated around asteroids in interplanetary space, quiet GEO, and LEO environments but have not been investigated in cislunar space [143, 175]. Therefore, the

effective Debye length is investigated for representative, dense cislunar plasma. An overview of the effective Debye length theory is first presented, followed by the solution methods used to determine the increase in the Debye length and the results in dayside solar wind plasma. Last, servicer and target interactions are investigated to provide a first look into charging and touchless potential sensing behavior at varying separation distances.

3.2 Cislunar Plasma Environment

As mentioned in Section 1.2.1, the Moon orbits through several plasma environments, and the mean plasma parameters in some of these environments are shown in Table 1.1. As indicated, the Debye length is larger than the proposed separation distances in the plasma sheet, magnetotail lobes, and the lower altitude lunar wake environments. In the solar wind, magnetosheath, and higher altitude lunar wake environments the Debye length is 10-20 m, which is on the lower end of separation distances proposed. It is in these regions that the investigation in this chapter is relevant.

The Debye length in the last column of Table 1.1 is computed from the relevant parameters assuming a Maxwellian plasma as

$$\lambda_D = \sqrt{\frac{\epsilon_0 T_e}{n_e q_e}}, \tag{3.1}$$

where ϵ_0 is the permittivity of free space, T_e is the undisturbed electron temperature in eV, q_e is the elementary charge in Coulombs, and n_e is the undisturbed electron density. A Maxwellian distribution typically assumes the plasma is collisional and in thermal equilibrium, but the cislunar plasma environment is non-collisional. Despite this, a Maxwellian distribution can be implemented as an approximated of the majority of a non-collision plasma distribution and is commonly used to represent cislunar plasma [32, 84, 87, 118]. Recent work has also indicated that a Kappa distribution, which has a higher energy tail than the Maxwellian distribution, is appropriate to approximate cislunar plasma distributions [75, 94, 197]. The inclusion of a Kappa distribution is not considered in this work and is recommended for future studies. The environments are assumed to have an

ion population of 100% protons (H^+). The solar wind is approximately 95% protons, 4% alpha particles (He^{++}) and 1% other ions [97, 147], so simulating the ion population using protons is an appropriate assumption.

In some of the environments shown in Table 1.1, the number of electrons n_e does not equal the number of ions n_i. Plasma is defined as quasi-neutral ($n_e \approx n_i$) on a macroscopic scale, so the data seemingly invalidates that assumption. In this case, the macroscopic scale can be defined by the Debye length shown in the last column in Table 1.1. Within a Debye length a charged particle is expected to alter the plasma conditions and quasi-neutrality may not be achieved. Electrostatic analyzer (ESA) instruments house on the main body of the ARTEMIS spacecraft were used to measure the electron and ion properties that are presented, and the main body of the spacecraft is 0.8x0.8x1 m [85], smaller than the Debye length. Therefore, the plasma density measurements are representative of those on a scale smaller than the Debye length presented in the last column, resulting in unequal electron and ion densities.

3.3 Effective Debye Length

3.3.1 Potential Approximation

Several analytic approximations of potential and electric fields in plasma exist. The appropriate representation depend on several variables, including the plasma properties, surface potential, and geometry. Two approximations are presented in this research: vacuum (Laplace) and Debye-Hückel. Both assume a spherical spacecraft, and their differing approximations provide a range of potential and electric fields that may be present around a charged sphere in plasma.

The vacuum approximation does not account for space charge shielding that occurs in a plasma. In a vacuum, the electric potential at a distance from the center of a sphere is

$$\phi(r) = \frac{V_{SC} R_{SC}}{r}, \tag{3.2}$$

where V_{SC} is the surface potential, R_{SC} is the radius of the sphere, and r is the distance from the sphere's center. This equation is only valid for $r > R_{SC}$. The electric field strength is the negative

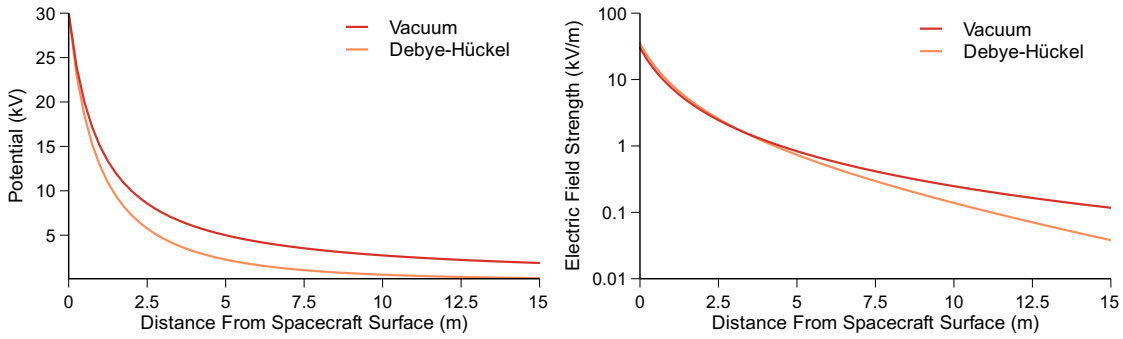

(a) Potential (b) Electric field strength

Figure 3.1: Potential and electric field strength estimated using the Debye-Hückel and vacuum approximation about a 30 kV, 1 m radius sphere (λ_D=10.1 m).

gradient of the potential

$$E(r) = -\nabla_r \phi(r) = \frac{V_{\mathrm{SC}} R_{\mathrm{SC}}}{r^2}. \tag{3.3}$$

In a plasma, the spacecraft potential is shielded, or approaches zero, closer to the spacecraft surface than in a vacuum. If the plasma is assumed to be Maxwellian and the charged body is assumed to be a sphere with a low surface potential compared to the plasma thermal energy ($q_e V_{\mathrm{SC}} \ll T_e$) the Debye-Hückel approximation of the electric potential can be employed [48]

$$\phi(r) = \frac{V_{\mathrm{SC}} R_{\mathrm{SC}}}{r} \mathrm{e}^{\frac{-(r-R_{\mathrm{SC}})}{\lambda_D}}. \tag{3.4}$$

The electric field strength is again the negative gradient of the potential

$$E(r) = -\nabla_r \phi(r) = \frac{V_{\mathrm{SC}} R_{\mathrm{SC}}}{r^2} e^{\frac{-(r-R_{\mathrm{SC}})}{\lambda_D}} \left(1 + \frac{r}{\lambda_D}\right). \tag{3.5}$$

The potential and electric field strength around a 30 kV, 1 m radius spacecraft in a plasma with an electron energy of 11 eV a Debye length of 10.1 m is shown in Fig. 3.1. Note that the electric field strength is plotted on a log scale for easier comparison. The Debye-Hückel values represent the minimum estimate of the fields because it assumes the charge is negligible compared to the plasma energy. The vacuum approximation then represents the maximum estimate of the field because no shielding is considered. It can be seen in Eqn. (3.4) that as the Debye length increases the exponential term trends towards 1, causing the potential to converge to the vacuum

Table 3.1: Mesh Independence Analysis

Parameter	**Final size Nascap-2k**	**Comparison size Nascap-2k**	**Percent difference**	**Final size SPIS**	**Comparison size SPIS**	**Percent difference**
Boundary distance	112 m	224 m	3.24	110 m	130 m	6.04
Boundary resolution	N/A	N/A	N/A	20 m	10 m	4.28
Near-spacecraft resolution	0.5 m	0.25 m	0.04	N/A	N/A	N/A

solution in Eqn. (3.2). As the Debye length increases, the shielding due to the plasma becomes less significant and the potential extends farther from the spacecraft. Therefore, as the Debye length approaches infinity the shielding due to the plasma becomes negligible and the potential resembles the vacuum approximation.

If the spacecraft potential is large compared to the ambient plasma, the potential is expected to be somewhere in between the Debye-Hückel and vacuum solution. In Fig. 3.1(a), from ≈5 m to 15 m from the spacecraft surface there is a difference of ≈3 kV in the potential. This represents significant uncertainty, and a more accurate approximation of the fields should be implemented for robust touchless potential sensing and electrostatic actuation investigations.

To approximate the potential about a highly charged spacecraft, the Debye length is simply multiplied by a scalar α in the Debye-Hückel approximation for the potential

$$\phi(r) = \frac{V_{\mathrm{SC}} R_{\mathrm{SC}}}{r} e^{\frac{-(r-R_{\mathrm{SC}})}{\alpha\lambda_D}}, \tag{3.6}$$

and electric field strength

$$E(r) = \frac{V_{\mathrm{SC}} R_{\mathrm{SC}}}{r^2} e^{\frac{-(r-R_{\mathrm{SC}})}{\alpha\lambda_D}} \left(1 + \frac{r}{\alpha\lambda_D}\right). \tag{3.7}$$

The *effective* Debye length is then $\alpha\lambda_D$. To determine the scaling parameters α, the potential about a spacecraft is determined using numerical or computational solvers. Once the potential is found in the programs, Eqn. (3.6) is fit to the solution using nonlinear least squares (NLS).

3.3.2 Solution Methods

The turning point method [152] and Poisson-Vlasov solvers [143, 175] have previously been implemented to determine the effective Debye length. The turning point method is most accurate

when the spacecraft radius is larger than the Debye length, limiting the spacecraft radii to larger than 10.1 m based on the smallest Debye length in Table 1.1. To investigate smaller spacecraft radii, Nascap-2k (version 4.4) and SPIS (version 6.1) are used to calculate the potentials in space. SPIS is a spacecraft plasma interaction software created by the Spacecraft Plasma Interactions Network in Europe (SPINE) [166], and Nascap-2k is a spacecraft charging and plasma interactions code developed as a collaboration between NASA and the Air Force Research Lab [128]. Nascap-2k is available to US citizens, and SPIS is open source. While both programs aim to solve similar problems, their underlying processes and assumptions vary.

Both programs are controlled through a user interface. First, the geometry of the spacecraft, surface materials, and size and resolution of the computational space is defined. SPIS implements a tetrahedral mesh generated and resolved in Gmsh to define the computational space, while Nascap-2k implements a user-defined Cartesian mesh. The ambient plasma can be defined with a Maxwellian or kappa distribution in both programs, with the energy, density, and other relevant parameters inputted. The programs offer a variety of solution methods for the currents on the spacecraft potential. SPIS is primarily a particle-in-cell (PIC) solver, which means that macro-particles are used to represent the electrons and ions throughout the space. It is also possible to define one or more of the particle species using the analytic Maxwell-Boltzmann approximation. Nascap-2k focuses more heavily on analytic or hybrid (analytic with some particle tracking) solutions. It is generally not possible to say which solution method is "correct", so the inclusion of both can be helpful for understanding the range of possible results.

To calculate the potentials in Nascap-2k, the analytic `non-linear` model in the "Space Potentials" tab is selected because it is applicable to high and low potentials in a dense plasma and is appropriate when the spacecraft velocity and the ambient magnetic field has minimal effect on the charge density within the sheath. The spacecraft velocity with respect to the plasma is set to zero in this chapter and will be investigated in the following chapter. While the plasma densities in cislunar space are low compared to LEO plasma, strict limits are not placed on the density for the non-linear model and high density plasma is interpreted to apply to environments in which the

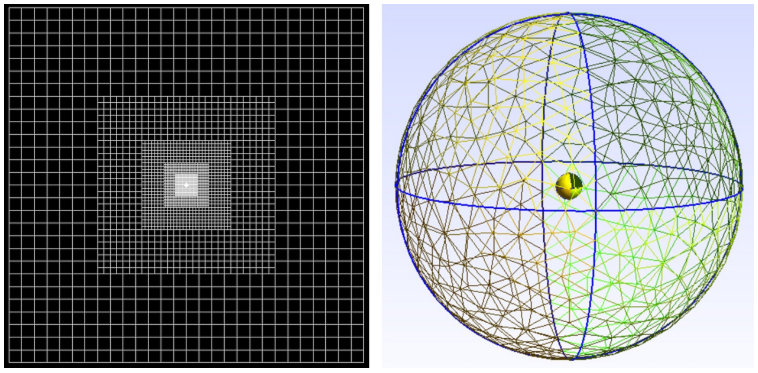

Figure 3.2: Nascap-2k cutview of grid (left) and SPIS 2D mesh (right) around a single spherical spacecraft.

vacuum approximation is not applicable. The electrical boundary condition is set to `DEBYE`, which estimates the potential on the boundary using the Debye-Hückel approximation. In theory, this should allow a smaller computational volume to be utilized compared to one in which the potential is zero on the boundaries.

In SPIS, the ions and electrons are modeled as PIC. Open boundaries are defined for the particles, which means particles can be injected and lost through the boundary surface. A Dirichlet electric boundary condition is selected, and the potential on the boundary is determined using the Debye-Hückel approximation to match Nascap-2k's boundary conditions.

The computational space is defined in Nascap-2k with cartesian elements, while SPIS utilizes a tetrahedal mesh. In both cases, the elements must be sized such that they are small enough to accurately determine the potential without using unnecessary computational power. The boundary must also be far enough away to minimize interference with the potential. To determine the appropriate mesh resolution and size, the mesh is refined about a 30 kV sphere until there is smaller than a 10% difference between the computed scaling parameters. A summary of the results is presented in Table 3.1, and a more detailed explanation of the analysis can be found in [35].

The boundary of the Nascap-2k simulation is defined 112 m from the spacecraft and the elements around the spacecraft are 0.5 m. The parent grids are defined with double the element size and the same number of elements as the smaller, child grid, making the resolution at the

boundary 8 m. The SPIS boundary is defined 110 m from the spacecraft with a surface resolution of 0.1 m and boundary resolution of 20 m. An intermediate mesh with an 8 m radius and 0.5 m elements is also defined to slow the size of the mesh expansion near the spacecraft. The final 2D-meshes are shown in Fig. 3.2.

When conducting PIC simulations, the time-steps must be small enough to ensure stability and smooth convergence, and the ions should not travel more than one mesh tetrahedral in each time-step [190]. In SPIS, a maximum timestep of 1E-6 s is implemented to satisfy this. In Nascap-2k, the maximum timesteps are set such that the solution smoothly converges. At this resolution and timestep, resolving the potential takes from 24 to 72 hours on a 16 GB RAM laptop, depending on the spacecraft size and surface potential.

3.3.3 Effective Debye Length Results

The effective Debye lengths in the dayside solar wind region are investigated because this region has the shortest electron Debye length in average conditions, and the Moon spends the majority of its orbit in the solar wind [145]. Regardless, the plasma parameters in the solar wind region will vary, and this region is considered a representative dense cislunar environment. From Table 1.1, the electron and ion density is 6E6 m^{-3}, ion temperature is 7 eV, and electron temperature is 11 eV. The bulk velocity of the plasma is not included in this chapter. Since the electron temperature is only 11 eV, if the spacecraft is charged more than a few volts, the Debye-Hückel assumption is no longer valid and an effective Debye length is likely a more accurate approximation.

To evaluate the effective Debye length scaling factor trends, computations are done for a spherical spacecraft with 0.25 m to 2 m radii and 1 kV to 30 kV potentials. Figure 3.3 shows the scaling parameters values and 1σ error bars associated with the NLS fit. The scaling parameter is consistently larger in Nascap-2k, so the potential may be narrowed down to somewhere in between the SPIS and Nascap-2k solutions. Both solution methods indicate that as the spacecraft become larger and the potential increases the scaling parameter increases with the largest effective Debye

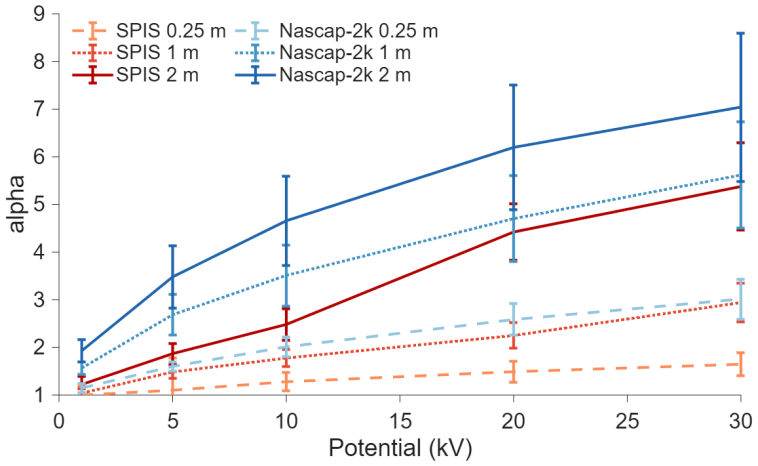

Figure 3.3: Scaling parameter solutions

length approximately seven times larger than the electron Debye length. This may increase the touchless potential sensing signal and electrostatic forces.

The error bars and difference between Nascap-2k and SPIS scaling parameters also increase as the scaling parameter increases. To explain this, the potential solutions, fits, and confidence bounds for a 30 kV, 1 m radius sphere are plotted over a gray-scale colormap of the potential computed for a range of scaling parameters in Fig 3.4. As alpha increases, the difference between potential values decreases, increasing the uncertainty in the fitted alpha value without actually increasing the uncertainty in the potential solution. This, in addition to differences in the software, explains why there is a difference in scaling parameter solutions, particularly for large spacecraft sizes and potentials.

3.4 Servicer-Target Interactions

3.4.1 Setup

Now that the appropriate approximation for the potential about a highly charged spacecraft has been determined, two aluminum, 1 m spherical spacecraft (a servicer and target) are modeled together in dayside solar wind plasma in Nascap-2k and SPIS. The servicer is held at 1 kV and 10 kV, the separation distance is varied, and the target is allowed to float. Potential control of one's

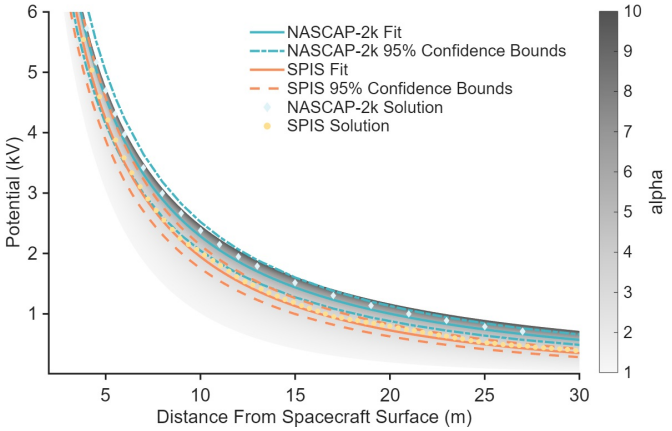

Figure 3.4: SPIS and Nascap-2k potential solutions, fits, and confidence bounds for a 30 kV, 1 m sphere. A background gray-scale colormap shows the potential calculated using Eqn. (3.6) for a range of α.

own spacecraft could be achieved through technologies such as biasing of electric field sensors [25], electron gun emissions [82, 90, 91], and ion emissions [157, 187–189]. The results provide insight into target's charging and electron emission behavior, and the detected current for touchless potential sensing.

The mesh definition is based on the findings from Section 3.3.2. The external boundary is defined at least 100 m from the edge of both spacecraft, Nascap-2k's grid elements are smaller than 0.5 m near the spacecraft surfaces, and SPIS's boundary resolution is smaller than 20 m. Figure 3.5 shows the meshes for a separation distance of 10 m.

In both tools, the target's surface potential is determined by solving the current balance equation

$$I_i(1+\delta_i) - I_e(1-(\eta+\delta)) + I_{ph} = 0, \tag{3.8}$$

where I_i and I_e are the incident ion and electron currents, respectively, and I_{ph} is the photoelectron current. The variables η, δ, and δ_i are the backscattered electrons, secondary electrons from electrons and secondary electrons from ions yields, respectively. The electron emission yields are defined the same in both tools, while the incident current computations differ.

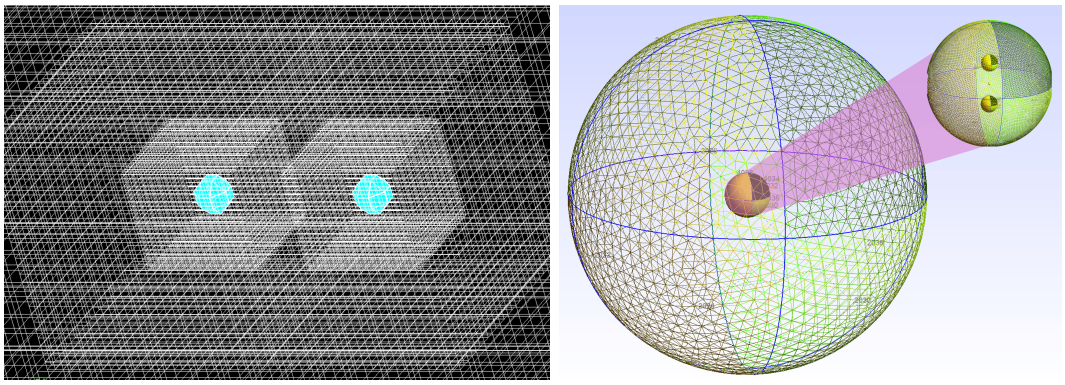

(a) Nascap-2k (b) SPIS

Figure 3.5: Nascap-2k and SPIS mesh for 10 m separation distance.

The secondary electron yield δ is defined based on a four parameter fit[47, 186]

$$R(E) = b_1 E^{e_1} + b_2 E^{e_2}, \tag{3.9}$$

where b_1 and b_2 are in Angstroms per eV and e_1 and e_2 are unitless inputs used when defining the material. The fitting parameters are 154, 220, 0.8, and 1.76 for b_1, b_2, e_1, and e_2, respectively, based on the values for aluminum in SPIS and Nascap-2k. The maximum yield $\delta_{\max}$ and electron energy at which the maximum yield occurs $E_{\max}$ is 0.97 and 300 eV, respectively.For more information on how the secondary electron yield is computed from the four parameter fit and maximum yield and energy at which the maximum yield occurs, see Section 6.2. The parameters presented here are the ones defined in the Nascap-2k and SPIS user interfaces to set the secondary electron yield. The photoelectron current density is defined as 4E-5A/m^2 in both programs.

The secondary electron from ions yield is

$$\delta_i(E) = \frac{\beta E^{1/2}}{1 + E/E_{\max,\mathrm{i}}} \tag{3.10}$$

where β is a scaling parameter and $E_{\max,\mathrm{i}}$ is the ion energy at which the maximum yield occurs. Values of 0.244 and 230 keV for β and $E_{\max,\mathrm{i}}$ based on the values for aluminum in Nascap-2k and SPIS.

SPIS is set up to compute the spacecraft charging and model the electron emissions in the same simulation by modeling all particles as PIC. The electron emissions are initialized with an

energy of 2 eV and a Maxwellian distribution. To avoid erroneously counting emissions from the servicer as emissions detected from the target, all electron emissions from the servicer are disabled.

Nascap-2k version 4.4 does not include the ability to model electron emissions as PIC. Thus, analysis requires two steps to investigate the servicer and target interactions: computation of target potential and simulation of emitted particle trajectories. For the first step, surface charging is computed using the "Tracked Ion & Analytic Electron Currents" option, which computes the electron surface currents using analytic formulas and the ion currents from tracked macro-particles. The potentials in space are once again found using the analytic non-linear option. Once the target potential and emitted currents are computed, the electron emission trajectories are modeled in a second simulation. To implement this, surfaces are assigned as "Emitters" in the **Object Toolkit**. The emitted current density, range of angles, and range of energies are specified, and the particles are generated from the surface. The range of both secondary electron and photoelectron emission angles is defined from 0 to π, the maximum range. Similar to the generation of secondary electron emissions in SIMION in Section 2.3.1, the secondaries are generated with an energy of 1.333 eV and the photoelectrons are generated from 1-3 eV. The secondaries are generated from all sides of the target, while the photoelectrons are generated from the sunlit half of the sphere.

3.4.2 Charging and Emissions

3.4.2.1 Potential Solution Comparison

Nascap-2k has the unique ability to determine the potential using the Debye-Hückel (Linear Debye Shielding) and vacuum (Laplace) approximations using the `Linear Debye Shielding` or `Laplace` options, respectively, available in the "Space Potentials" tab. Using these options, the electron emission trajectories in varying potentials can be compared to emphasize the importance of appropriately modeling the potential.

The photoelectron trajectories computed using the listed solution methods are shown in Fig. 3.6. The non-linear solution, equivalent to the Debye-Hückel assumption with an effective

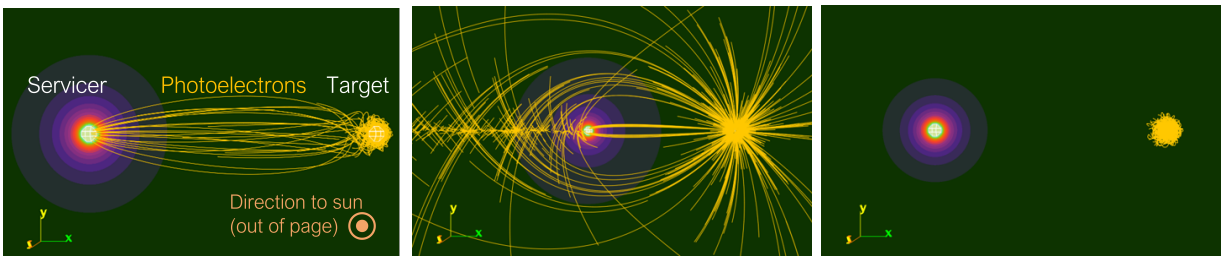

(a) Non-linear (b) Laplace (c) Debye-Hückel

Figure 3.6: Photoelectron trajectories from a 5 V, 1 m radius target (right) to a 1 kV, 1 m radius servicer (left) at 40 m separation using varying potential approximations.

Debye length, shows that the servicer's potential is just positive enough near the target to attract photoelectron emissions from the side of the target facing the servicer. The Laplace solution overestimates the servicer's sphere of influence, so photoelectrons are attracted to the servicer across the entire solution space. Utilizing this assumption would vastly overestimate the servicer's influence and detected emissions, leading to unrealistic expectations when detecting a target's potential in cislunar orbit. Conversely, the Debye-Hückel solution shows that all electron emissions are attracted back into the target's surface. This underestimates the servicer's influence, leading to overly conservative estimates of detected emissions. This could lead to decisions to not conduct touchless potential sensing operations in cislunar conditions when sensing is actually possible, missing out on the opportunity to gain insight into the target's potential for safety, science, or electrostatic actuation operations.

3.4.2.2 Sunlit Environment

The dayside solar wind environment is, as the name implies, a sunlit environment. Here, the photoelectron current is expected to dominate, so the spacecraft typically charges a few volts positive and photoelectron emissions are the main source of current for touchless potential sensing. In these simulations, the sun illuminates both the servicer and target, so photoelectrons are generated on the side of the target perpendicular to the servicer. The trends in this section can be compared to expected behavior during active potential sensing because a consistent current is

generated and sensed by the servicer. In this case, the initial photoelectron current is constant, while for active potential sensing the initial secondary electron current from an electron beam or photoelectron current from a VUV laser is relatively constant.

Figure 3.7(a) shows the surface potential solutions in Nascap-2k and SPIS and the potential calculated using Eqn. (3.6) using the SPIS scaling parameters found from Fig. 3.3. There are significant differences between the solutions in the two codes. Nascap-2k indicates that the target charges to ≈5 V in all simulations, while the target in SPIS charges highly positive near the servicer then settles to ≈8 V farther away. In SPIS, the emissions are modeled as PIC, and the highly positive servicer is capable of pulling emissions away from the target. In fact, it is seen that the surface potential of the target roughly follows the servicer's potential values, again indicating the importance of appropriately modeling the potential. Because the emissions are not modeled as PIC in Nascap-2k when determining the target's potential, the simulation does not take into account that the highly positive servicer is capable of drawing electron emissions away from a positive target, and once the target is a few volts positive it is assumed that the majority of the emissions are recollected. This indicates that SPIS may be a more appropriate tool for touchless potential sensing and charging simulations and the servicer drawing emissions away from a target should be taken into account when investigating charging behavior. Quantify the charging behavior is investigated more in depth in Chapter 6.

The target charges highly positive, so the difference in potential is *less* than the potential of the servicer. However, the minimum energy of electrons that may be detected is equal to the servicer's potential. This is often how the potential of a spacecraft is determined using an ESA instrument like an RPA [46, 58, 112]. In this case, the target's potential would be detected as zero in all cases, leading to hundreds of volts of error if taken at face value. Instead, if the servicer's potential is large, electron emissions are detected (indicating that the servicer is drawing emissions from the target), and the energy of the electrons is equivalent is equal to the servicer's potential, an appropriate assumption is to assume the target potential is approximately equal to the value of the potential generated by the servicer at that separation distance.

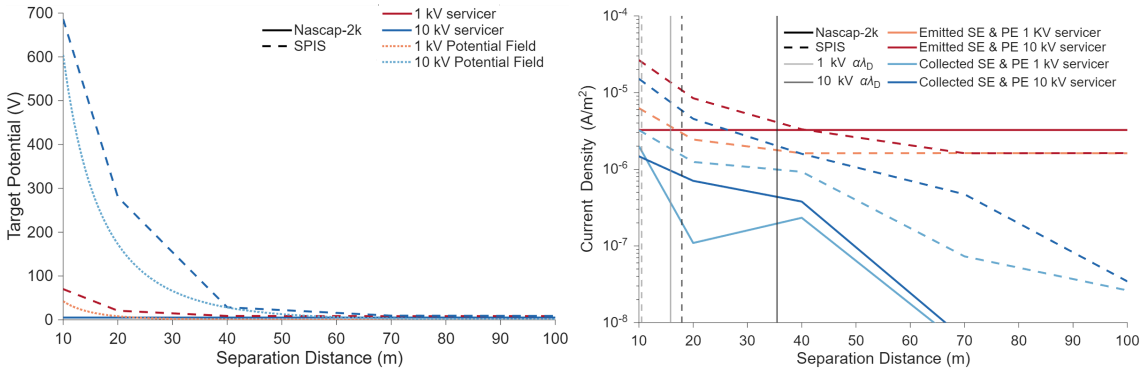

(a) Potentials (b) Currents

Figure 3.7: Target potentials (left) and emitted and collected currents (right) for varying separation distances from a constant potential servicer in a sunlit environment.

Figure 3.7(b) displays the emitted secondary (SE) and photoelectron (PE) current from the target and collected current by the servicer. The vertical lines again indicate the effective Debye lengths. It is important to note that the emitted current is the initially generated current minus the current recollected by the target, so this is only the current that leaves the target. Because Nascap-2k does not take into account the servicer drawing emissions away from the target, the emitted current is the same in all simulations. In SPIS, the emitted current is largest nearest to the servicer because the emissions are pulled from the target and towards the servicer. In addition, the emitted current density settles to ≈1.6E-6 A/m^2 in SPIS at approximately twice the separation distance about the 10 kV servicer than the 1 kV servicer. This again makes sense because the scaling parameter is ≈1.7 times larger for the 10 kV servicer. In both simulations, the collected current decreases as the separation distance increases, which follows expectations because the servicer has more influence on the initial electron emissions trajectories when it is closer to the target.

The 10 kV servicer collects from 1.3 to 6.5 times the current the 1 kV servicer collects. This corroborates the results in Fig. 2.3(b) from the previous chapter, where a 10 kV servicer collected up to double the current detected by a 1 kV servicer depending on the target's potential. However, a more positive servicer will also attract more ambient electrons. The electron emissions from the target must be distinguishable from the ambient electrons in order to determine the target's

potential. This is comparable to achieving a sufficient signal to noise ratio. So, if the increase in electron emission current is not larger than the increase in plasma electron current, the signal is actually worse. The electron current to a positively charged spherical spacecraft increases by a factor of $1 + V_{SC}/T_e$ [110], so the 10 kV servicer collected ≈9.9 times more electron current than the 1 kV servicer. Since the rise in electron current is larger than the rise in detected electron emissions, increasing the servicer's potential leads to a *worse* measurement. Thus, it is better to keep the servicer less positive for touchless potential sensing despite larger effective Debye lengths around a more positive servicer. A more in depth analysis of the feasibility of distinguishing the detected current from the environment is presented in the following chapter.

3.4.2.3 Eclipsed Environment

To gain insight into the behavior in an eclipsed environment, photoemissions are disabled and the simulations are repeated. This is possible in the dayside environment if the target is shadowed by the servicer or other object. Regardless, this environment serves as a representative cislunar environment and can be extended to indicate how the spacecraft may behave in an eclipsed cislunar region.

Figure 3.8 shows the target potentials and emitted and collected secondary electron currents as a function of separation distance. The vertical lines again indicate the effective Debye lengths. When the target is closest to the servicer, it charges most negative and has the lowest secondary electron emission. As the separation distance increases, the energy of the ambient electrons decreases and the secondary electron emission current increases. This is the consequence of several factors. One, ions are repelled and electrons are attracted by the highly positive servicer, leading to a more negative target. This negative target then repels electrons, leading to less electron impacts to generate secondaries. In addition, it is possible that the highly positive servicer is accelerating the ambient electrons which then impact the target at a higher energy and reduced secondary electron yield.[1] Again, methods to quantify this charging behavior near a highly positive servicer

[1] See Fig. 2.10 for examples of the secondary electron yield as a function of impact energy.

are investigated in Chapter 6.

The lower emission current when the target is near the servicer leads to a more complicated relationship between detected current and separation distance than seen in the previous section. The current collected by the servicer initially increases as the separation distance increases due to the increase in emitted current. Then, once the target reaches its peak emission current the collected secondaries decrease with further increasing separation. This peak occurs when the separation distance is approximately twice the effective Debye length ($2\alpha\lambda_D$). This places the target outside the sphere of influence, allowing it to charge more positively, be impacted by more lower energy electrons, and emit more secondaries while remaining close enough for the servicer to draw in electron emissions.

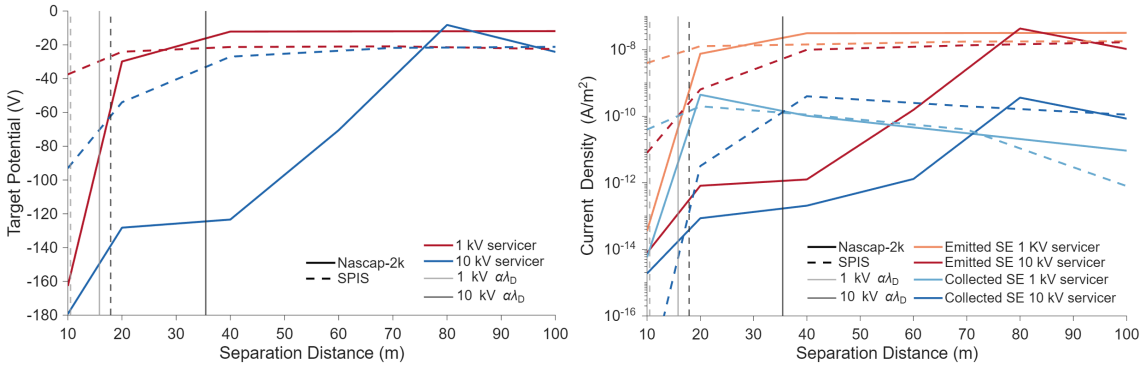

(a) Potentials (b) Emissions

Figure 3.8: Target potentials (left) and emitted and collected currents (right) for varying separation distances from a constant potential servicer in an eclipsed environment. Vertical lines indicate the effective Debye lengths.

At 100 m of separation the 10 kV servicer collected 9.2 times and 14 times more current than the 1 kV spacecraft in Nascap-2k and SPIS, respectively. This is near the increase in ambient electron current that results due to increasing the servicer's potential, indicating that at exceedingly large separation distances the servicer's potential can be increased to improve the detected electron emission to ambient electron ratio. Within a separation $2\alpha\lambda_D$, the 1 kV servicer detects more than the 10 kV servicer, and between $2\alpha\lambda_D$ and 100 m the 10 kV servicer detects less than 9 times the current of the 1 kV servicer. So, the lower potential servicer is again better for touchless potential

sensing within 100 m of separation.

The maximum current density detected is about 1E-10 A/m^2 for both spacecraft potentials, which is likely not large enough to determine the target's potential. This indicates that at large separation distances, sufficient current for passive potential sensing using secondary electron emissions may be difficult. In this case, active potential sensing is a more reliable option. A more in depth analysis of the conditions in which passive potential sensing can be conducted is presented in the next chapter.

3.5 Conclusions

The effective Debye length in a representative solar wind environment is determined using Nascap-2k and SPIS. It is found that the scaling parameter for the effective Debye length increases with increasing surface potential and radius. Nascap-2k generates larger effective Debye lengths with a maximum scaling parameter of ≈7.0 while SPIS indicates a maximum scaling parameter of ≈5.4. The significance of utilizing the appropriate potential approximation is emphasized in Nascap-2k simulations with varying potential approximations, where ignoring shielding led to a significant overestimation of the current to the servicer while utilizing the electron Debye length instead of the effective Debye length led to a significant underestimation of the servicer's influence.

In a sunlit environment, when a target approaches a highly charged servicer the photoelectron emissions are pulled away from the target and into the servicer, leading to an increase in detected current and target surface potential. In fact, the target's potential can be roughly approximated using the the servicer's potential magnitude at the location of the target. This again indicates the importance of appropriately estimating the potential with an effective Debye length. In an eclipsed environment, the target charges more negatively near the servicer and has a lower secondary electron current. Therefore, a separation distance of $2\alpha\lambda_D$ or low servicer potential is proposed to increase the detected current during passive potential sensing operations in eclipse. Furthermore, a lower servicer potential is found to generate a larger detected electron emission to ambient electron ratio, so a lower servicer potential is better suited for passive touchless potential sensing despite having

a lower effective Debye length. The results also provide a glimpse into the charging behavior of a spacecraft in the vicinity of another highly charged spacecraft, which will be further investigated in Chapter 6 and the importance of managing the servicer's potential for touchless potential sensing, which will be further investigated in the following Chapter 4.

Chapter 4

Sensing Through Barriers

4.1 Motivation

The potential shielding around a charged spacecraft investigated in the previous chapter is one of the spacecraft-plasma interactions that had previously not been explored in cislunar space. It was shown that electron emissions are able to reach a servicer over separation distances larger than a Debye length, but not all cislunar interactions were considered. In addition to short Debye lengths, spacecraft wakes and nonmonotonic sheaths can form. These formations can generate barriers that block electron emissions, limiting the signal for touchless potential sensing.

This work aims to determine the conditions in which spacecraft wakes and nonmonotonic sheaths form around Moon-orbiting spacecraft and their impact on electron emissions used for passive potential sensing. As explained in Section 1.2.1, the magnetotail lobes and plasma sheet contain high-energy, low-density plasma, similar to the GEO environment, while the magnetosheath and solar wind consist of lower-energy, denser plasma. It is in these latter environments that spacecraft wakes and nonmonotonic sheaths are expected to form. The Moon spends most of its orbit in the solar wind environment, so plasma parameters representative of solar wind plasma are implemented in this study. The conclusions can be extended to other environments in which spacecraft wake and nonmonotonic sheath formations can be expected.

An overview of spacecraft wakes and nonmonotonic sheaths are first presented. Then, the spacecraft wake and nonmonotonic sheath formations are characterized for varying spacecraft sizes and surface potentials. The impact of these formations on passive potential sensing and the feasi-

bility of passive potential sensing is then investigated. Last, barrier formations and the feasibility of active potential sensing is presented.

4.2 Cislunar Interactions

4.2.1 Spacecraft Wakes

As a spacecraft moves through plasma, the ambient electrons and ions are absorbed or moved out of the way. In mesothermal environments the ion thermal velocity v_i is less than the velocity of the spacecraft with respect to the ambient plasma v_{sc} which is less than the electron thermal velocity v_e ($v_i < v_{sc} < v_e$). Under these conditions, electrons catch back up to the spacecraft and impact on all sides, while the ions may take several spacecraft lengths to return to their undisturbed conditions, creating a complex region devoid of ions referred to as the spacecraft wake. Spacecraft wakes are investigated numerically to understand wake formations about spacecraft with large potentials [93, 195, 196], their impact on surface charging [140, 198], and their effects on scientific instruments [24, 142, 178]. Spacecrafts wakes have also been generated in vacuum chamber experiments to determine their properties [88, 132, 150, 156, 182], characterize how wakes alter space plasma measurements [6, 56], and even investigate the effects of lunar wakes on regolith charging [211].

Around the Moon, spacecraft wakes are expected in the solar wind and magnetosheath regions [36]. On the dayside of the Moon, the wake formation remains relatively consistent for varying spacecraft altitudes. On the eclipse side, spacecraft wakes are smaller near the surface, but as the craft's altitude increases the wakes grow and eventually resemble the dayside wakes. In these regions, the solar wind is flowing from the Sun at velocities of several hundred kilometers per second, while the spacecraft orbits the Moon with velocities on the order of one kilometer per second. Therefore, the wake always forms on the eclipse side of the Moon, regardless of the direction of the spacecraft's velocity, as demonstrated in Fig. 4.1.

The shape and size of an ion wake depend upon several parameters, including the ion energy,

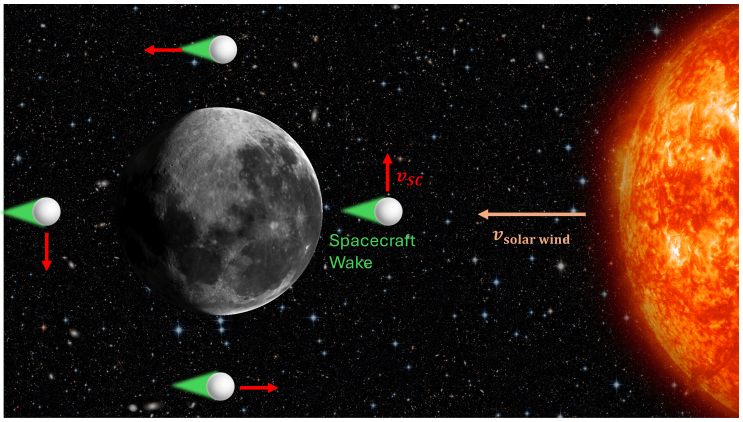

Figure 4.1: Cislunar spacecraft ion wake formations

bulk velocity, spacecraft size, spacecraft potential, and Debye length. A *narrow wake* forms with a width approximately equal to the spacecraft width W_{SC} when the ion bulk flow energy E_{bulk} is greater than the magnitude of the spacecraft potential $q_e\phi_{SC}$. The bulk flow energy in eV is

$$E_{\text{bulk}} = \frac{m_i v_{\text{bulk}}^2}{2q_e}, \tag{4.1}$$

where m_i is the ion mass and v_{bulk} is the bulk velocity is the plasma (also approximately equal to v_{sc} in cislunar plasma). If the spacecraft potential becomes more positive than the ion flow energy and the Debye length is larger than the spacecraft width ($\mathrm{m}_i\mathrm{v}_{\text{bulk}}^2/2 < q_e\phi_{SC}$, $\lambda_D > \mathrm{W}_{sc}$), an *enhanced wake* formation can occur. In this formation, the ions are deflected around the points where the potential $\phi(r)$ is equal to the ion flow velocity instead of the spacecraft body, and a significantly wider wake can form. Conversely, if the magnitude of a negative spacecraft's potential is larger than the ion flow velocity and the Debye length is comparatively large ($\mathrm{m}_i\mathrm{v}_{\text{bulk}}^2/2 < -q_e\phi_{SC}$, $\lambda_D > \mathrm{W}_{sc}$), a *focused wake* can form with a width much smaller than the spacecraft width [6, 54, 55, 59].

In wake formations in which the Debye length is much larger than the spacecraft, the changes in the potential are averaged out over the width of the wake. In other words, the wake size is increased or decreased when the spacecraft becomes more positively or negatively charged, but changes to the potential due to the absence of ions in the wake are averaged out and negligible. If the spacecraft width is larger than the Debye length, the wake can create negative potentials due to the absence of ions [72]. This negative potential can create a barrier that low energy electron

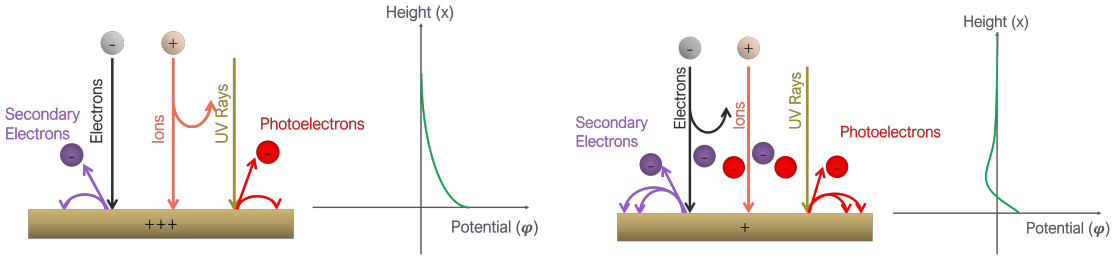

(a) Monotonic (b) Nonmonotonic

Figure 4.2: Schematic of monotonic and nonmonotonic sheath formation for a positively charged, sunlit spacecraft.

emissions cannot get through, but the magnitude of this barrier as a function of spacecraft size and potential has not been investigated.

4.2.2 Nonmonotonic Sheaths

In a typical spacecraft sheath, the potential decreases monotonically from the spacecraft surface value to zero. In this scenario, low-energy electron emissions, such as secondary electron and photoelectron emissions, can return to the surface if the spacecraft is positively charged, as shown in Fig. 4.2(a). Conversely, if the spacecraft is charged negatively, the electron emissions should be repelled from the spacecraft surface.

When electrons are emitted, their negative charge reduces the potential. Once the ratio of emitted electrons to incoming electrons Γ reaches some critical value Γ_c, the electrical field above the surface becomes zero and a space-charge-limited (SCL) sheath is formed. The electrons then are not accelerated away from the spacecraft surface and settle a short distance away, typically characterized by the photoelectron λ_{ph} or secondary electron λ_{SE} Debye length. This is the same concept that was analyzed in Section 2.2.4. Further electron emissions then cause the potential to dip below the spacecraft surface potential. Figure 4.2(b) shows an example of a nonmonotonic potential sheath above a positive spacecraft. This sheath formation can occur as a result of photoelectron and/or secondary electron emissions, and the critical ratio Γ_c can be approximated as [89]

$$\Gamma_c = 1 - 8.3\sqrt{\frac{m_e}{m_i}}, \tag{4.2}$$

where m_e is the mass of an electron and m_i is the ion mass. The nonmonotonic sheath is also a barrier that can prevent low-energy electron emissions from leaving the spacecraft surface, effectively reducing the emitted electron yield. If the ambient electron energy is greater than the electron emission energy, as would be expected in the cislunar solar wind, the reduction of electron emission current is greater than the reduction of incoming electron current and the spacecraft charges more negatively than expected.

In addition to having a large emitted to incoming electron ratio, the spacecraft size must be comparable to or larger than the photoelectron and electron Debye lengths for nonmonotonic sheaths to form. The photoelectron Debye length is typically much smaller than the electron Debye length and dominates near the spacecraft surface, while the electron Debye length dominates farther from the spacecraft. If the spacecraft is comparable in size to the electron Debye length and much larger than the photoelectron Debye length, the *thin sheath* approximation applies. In this regime, a nonmonotonic sheath creates a potential barrier close to the spacecraft surface. If the spacecraft is much smaller than the Debye length, the *thick sheath* approximation applies, and the barriers effectively disappear. In this regime, recollection of electron emissions is driven by positive surface potentials attracting emitted electrons instead of the nomonotonic sheath.

Nonmonotonic sheaths have been investigated both analytically and numerically to determine their impact on spacecraft charging [49, 57, 71], scientific measurements [199, 213], and lunar surface charging [32, 164, 214]. Experimental results have validated their formation [73, 200], and they have been observed above the dayside lunar surface [153] and about the HELIOS spacecraft [98]. However, a complete characterization of nonmonotonic sheath formation as a result of the spacecraft size to Debye length ratio and spacecraft surface potential has not been presented.

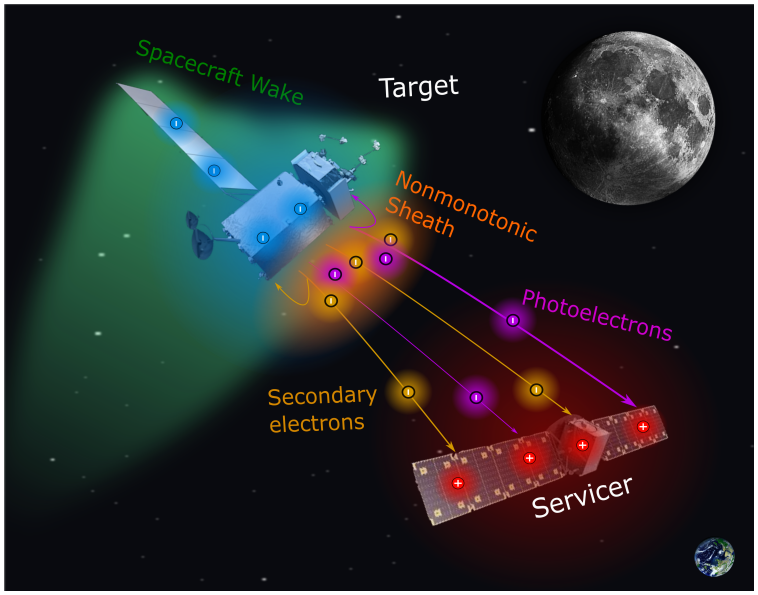

Figure 4.3: Passive touchless potential sensing in cislunar space concept.

4.3 Passive Potential Sensing

4.3.1 Simulation Setup

Simulations are conducted in SPIS in two environments: solar wind dayside and solar wind eclipse at an altitude greater than 12,000 km. The environment parameters are based on the mean environments given in the DSNE and presented in Table 1.1 [117]. In the solar wind eclipse environment, the ion density is not equal to the electron density. This creates a non-neutral plasma that is incompatible with the Dirichlet boundary condition, and there is currently no accepted solution to resolve this in spacecraft-plasma interaction codes with a defined computational boundary. It is possible to determine the charging behavior without a grid in Nascap-2k, and it is found that changing the ion density results in less than a 10% difference in the spacecraft potential, less than the change in potential that occurs if a different solution method is chosen for the same environment [39]. Therefore, the ion density is held equal to the electron density ($n_i = n_e$ =2.5E6 m^{-3}) in the solar wind wake environment and the solutions are considered representative.

The current balance equation is again given by Eqn. (3.8), and the SPIS simulation setup is

Table 4.1: Surface material parameters

Parameter	**Solar Wind Dayside**	**Solar Wind Eclipse >12,000 km**
Photoelectron Current Density (J_{ph})	4E-5 A/m^2	N/A
Max SE Yield ($\delta_{\max}$)	0.97	1.25
Energy at Max SE Yield ($E_{\max}$)	300 eV	135 eV

similar to that described in Section 3.4.1. The fitting parameters are again 154, 220, 0.8, and 1.76 for R_1, R_2, e_1, and e_2, respectively, based on the values for aluminum-2k in SPIS. The maximum yield $\delta_{\max}$ and electron energy at which the maximum yield occurs $E_{\max}$ for each environment are shown in Table 4.1. For all scenarios, the ions are assumed to be H^+ following the justification provided in Section 3.2, so the critical ratio at which a nonomonotonic sheath can form using Eqn. (4.2) is approximately 0.81. The $\delta_{\max}$ and $E_{\max}$ parameters are selected such that δ is less than Γ_c in the dayside plasma and greater than Γ_c in the eclipse plasma. This causes a nonmonotonic sheath due to secondary electrons to form in the eclipse environment and a nonmonotonic sheath due to photoelectrons to form in the dayside environment and allows the different types of sheath formations to be evaluated independently of each other. The main difference between the photoelectron and secondary electron sheaths is the density of the two emissions (photoelectron density is typically larger) and the regions around the spacecraft in which the sheaths form. Photoelectrons are only emitted on the sunlit side of the spacecraft, while secondaries may be emitted from all faces.

The photoelectron number density n_{ph} is

$$n_{ph} = \frac{2J_{ph}}{q_e v_{ph}}, \tag{4.3}$$

where J_{ph} is the photoelectron current density, $v_{ph} = \sqrt{2q_e T_{ph}/(\pi m_e)}$ is the photoelectron velocity, and T_{ph} is the photoelectron temperature. Both photoelectron and secondary electron emissions are assumed to have an energy of 2 eV and are given a Maxwellian distribution in SPIS. The photoelectron number density is then approximately 1054 cm^{-3}, and the photoelectron Debye length λ_{ph} using Eqn. (3.1) is 0.32 m.

A 0 V Dirichlet boundary condition is implemented, and the external boundary is set far

enough from the spacecraft to allow the potential to naturally reach zero before reaching the boundary (typically $\approx 6\lambda_D$). On the spacecraft surface, the resolution is 0.15 m, about half the photoelectron Debye length. A charging simulation with a 0.1 m mesh size on the spacecraft surface showed negligible difference in results while significantly increasing the computational time. The external boundary resolution is 5 m in the solar wind dayside and 10 m in the solar wind wake environment, about half the respective Debye lengths.

Open boundaries are defined for the particles, which means particles can be injected and lost through the surface. The ambient electrons and ions and electron emissions are modeled using the particle-in-cell (PIC) option. The maximum integration time for all particles is set to 1E-6 s, approximately the time it takes the ions to cross the smallest mesh tetrahedral. The total run time is at least 2E-4 seconds, the time it takes the ions to cross the entire computational space. If the simulation has not converged in this time, meaning the surface potentials and currents are still changing, the computational time is extended. The steady state is typically achieve between 3E-4 and 5E-3 seconds, and the run time is between 3 to 48 hours using a 32 GB RAM desktop depending on the scenario simulated.

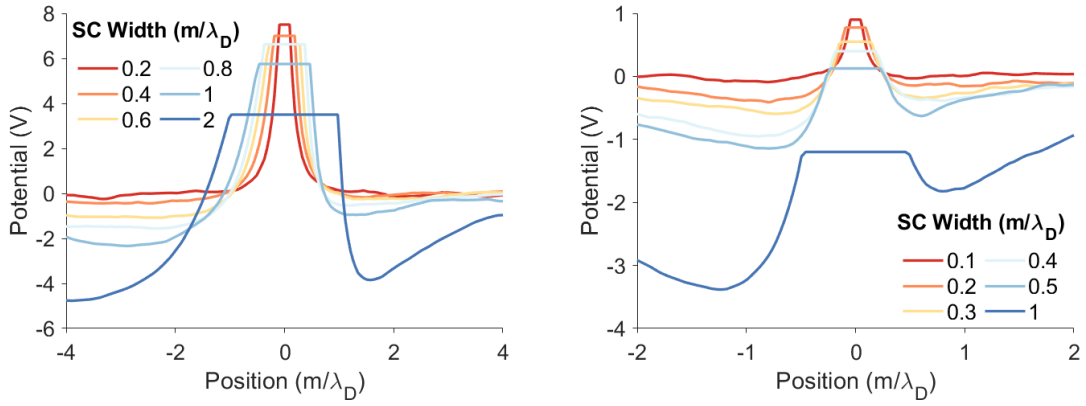

(a) Dayside

(b) Eclipse

Figure 4.4: Potentials about spacecraft of varying widths in the dayside and eclipse environment. Positive and negative x values indicate the ram and wake side of the spacecraft, respectively.

4.3.2 Single Spacecraft Characterization

4.3.2.1 Floating Spacecraft

The solar wind cislunar environment is unique because it is possible for smaller spacecraft to be in the thick sheath regime, while nearby larger spacecraft can be in the thin sheath regime. Therefore, it is necessary to determine the spacecraft width to Debye length ratio at which the regime transitions from thick to thin sheath and barriers due to spacecraft wakes and nonmonotonic sheaths may be expected to form. This is first done using floating cubic spacecraft of varying widths to provide insight into when the barriers form and how they impact the charging behavior of the spacecraft.

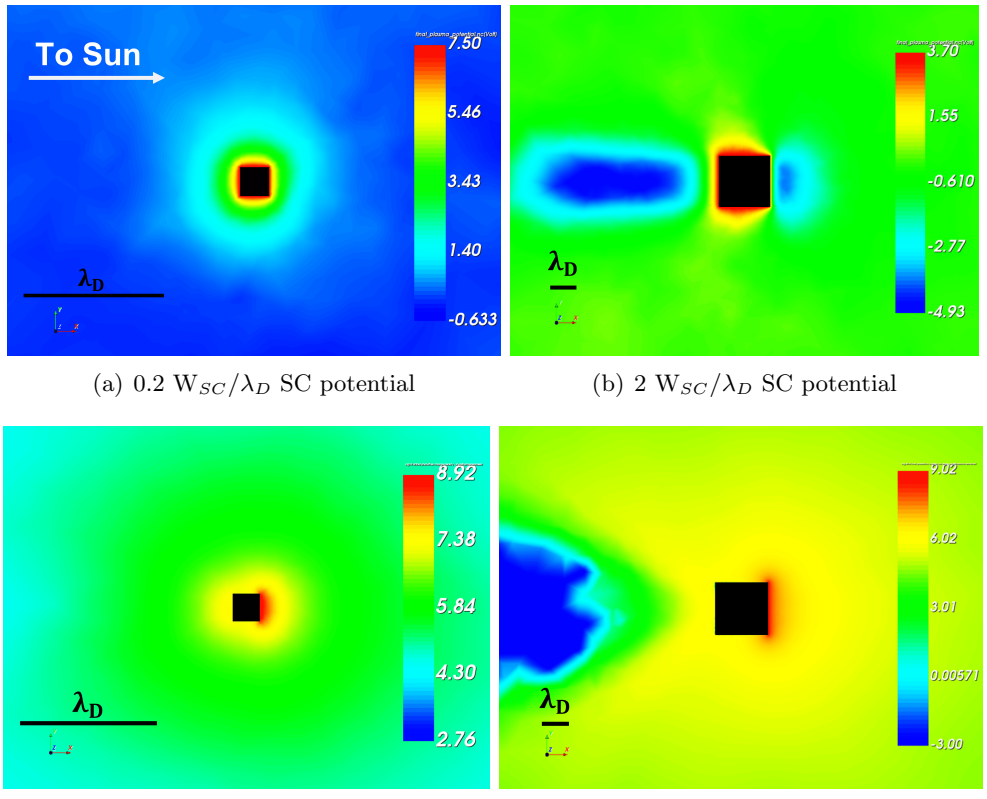

(a) 0.2 W_{SC}/λ_D SC potential

(b) 2 W_{SC}/λ_D SC potential

(c) 0.2 W_{SC}/λ_D SC $\log_{10}(n_{ph})$

(d) 2 W_{SC}/λ_D SC $\log_{10}(n_{ph})$

Figure 4.5: The potential (top) and $\log_{10}$ of the photoelectron density n_{ph} (bottom) around a 0.2 W_{SC}/λ_D (left) and 2 W_{SC}/λ_D (right) spacecraft in solar wind dayside plasma

Figure 4.4 shows the resulting potential about the floating spacecraft with varying width to

Debye length ratios ρ. As ρ increases, barriers due to the wakes and nonmonotonic sheaths begin to form. In the dayside environment, the nonmonotonic sheath begins to form due to photoelectron emissions on the ram side of the spacecraft (positive x-values in Fig. 4.4) when ρ is 0.8. On the wake side, the ion wake begins to influence the potential and create a barrier when ρ is 0.6. As ρ increases beyond these values, the size of the barrier increases, preventing more electron emissions from leaving the spacecraft surface and driving the spacecraft more negative. This trend is also seen for the spacecraft in the eclipse environment, but barriers begin to form on the ram and wake side of the spacecraft when ρ is 0.4 and 0.2, respectively. The secondary electron emissions on the wake side may increase the barrier size at lower ρ values. In addition, the spacecraft potential magnitudes are lower in this region, and the relationship between the spacecraft potential and barrier formation is explored in the next section.

The difference in potential and photoelectron trajectories for a spacecraft in a thick and thin sheath regime in the dayside environment is demonstrated in Fig. 4.5. When the spacecraft is much smaller than the Debye length (thick sheath), the potential decreases monotonically to zero as the distance from the spacecraft surface increase, and the photoelectrons create a **photoelectron sheath** around the body. When the spacecraft is larger barriers due to the spacecraft wake and photoelectron nonmonotonic sheath are observed. The minimum potential in the nonmonotonic sheath occurs approximately 5 meters from the spacecraft surface, about half a Debye length. This allows some photoelectrons to escape around the sides of this barrier; however, the wake prevents photoelectrons from entering the wake side of the spacecraft, creating an empty region in the photoelectron sheath.

4.3.2.2 Constant Potential

In the previous section, barriers formed for smaller ρ values in the eclipse environment than the dayside environment. However, the floating spacecraft potentials are smaller in eclipse, indicating that there is likely a relationship between the spacecraft potential and barrier size. There is precedence for this; Thiebault et al. [185] shows that if a spacecraft becomes more than a couple

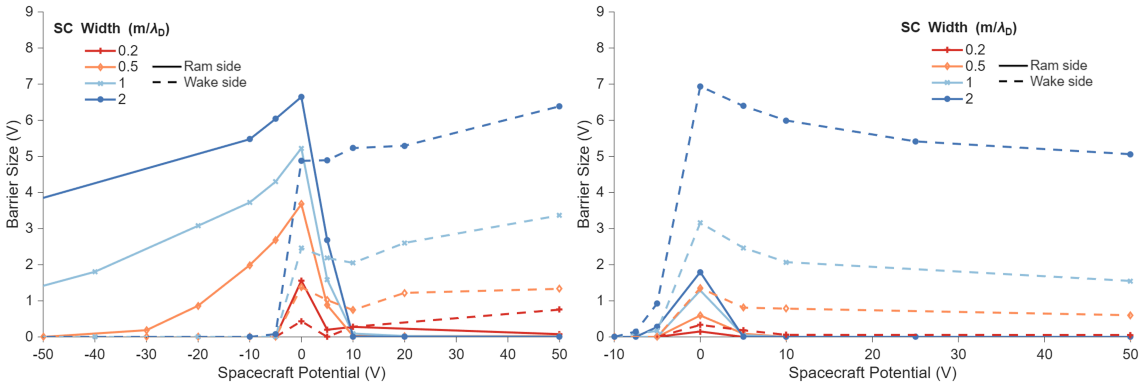

(a) Dayside (b) Eclipse

Figure 4.6: Barrier size on the wake and ram side of constant potential spacecraft on the dayside (left) and eclipse side (right) of the Moon.

volts positive, the electron emissions are attracted back into the surface and the barrier disappears. However, the relationship between negative spacecraft potentials and the barrier formation has not been established, and varying spacecraft size in the same environment has not been considered.

The size of the barrier ϕ_{barrier} for this evaluation is considered to be

$$\phi_{\text{barrier}} = \phi_{\text{min}} - V_{SC} \quad \text{for } V_{SC} < 0, \tag{4.4a}$$

$$\phi_{\text{barrier}} = -\phi_{\text{min}} \quad \text{for } Vi_{SC} > 0, \tag{4.4b}$$

where ϕ_{min} is the minimum potential and V_{SC} is the surface potential of the spacecraft. Typically, a positive spacecraft potential is considered as part of the barrier ($\phi_{\text{barrier}} = V_{SC} - \phi_{\text{min}}$ for $V_{SC} > 0$) because a positive spacecraft also draws electron emissions back into the spacecraft. For this study, barriers due to nonmonotonic sheaths and spacecraft wakes are isolated from the spacecraft potential.

Figure 4.6 shows the barrier sizes on the wake and ram side of spacecraft of varying widths and surface potentials on the dayside and eclipse side of the Moon. As observed with floating spacecraft, the larger the spacecraft become the larger the barriers become. For all spacecraft sizes, once a spacecraft becomes a couple volts positive, the electron emissions are attracted back into the spacecraft surface, and the nonmonotonic sheath and associated barriers disappear, matching the

results from [185]. It is possible that a small barrier exists within one mesh element in the simulation and not captured for more positive potentials than indicated. At this point, the size of the barrier is likely smaller than 2 eV, the mean energy of the electron emissions, and the recollection of electron emissions is driven by the positive spacecraft potential more than the barrier.

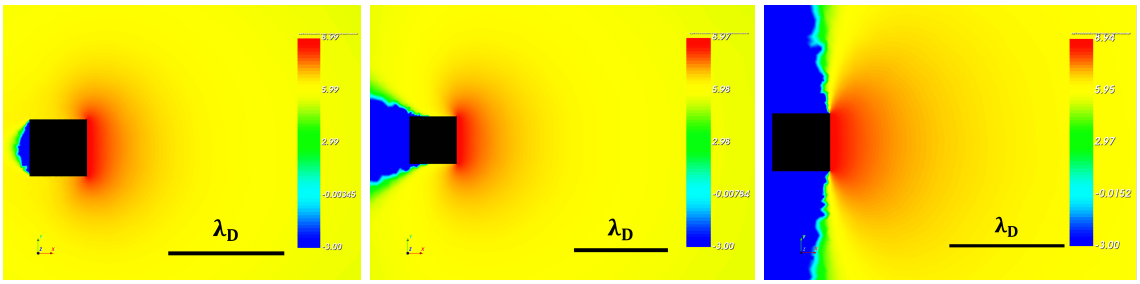

(a) 0 V (b) -5 V (c) -20 V

Figure 4.7: $\log_{10}$ of the photoelectron density about a 0.5 W_{SC}/λ_D width spacecraft in the solar wind dayside region at various surface potentials.

The nonmonotonic barriers on the ram side persist for larger negative spacecraft potentials. The reason for this is two-fold. When the spacecraft becomes more negative, the electron emissions are more effectively repelled, decreasing Γ near the surface of the craft. In addition, the electron emissions are accelerated, increasing the T_e value for the photoelectron or secondary electron Debye length from Eq.(3.1). This causes the emissions to spread out and settle farther from the spacecraft, decreasing the barrier size. Figure 4.7 demonstrates this, as the red region of dense photoelectrons spreads farther from the spacecraft as the surface potential gets more negative. In addition, the dark blue region indicating an absence of photoelectrons becomes larger as the spacecraft gets more negative. At smaller potential magnitudes, the photoelectron emissions can nearly surround the spacecraft and generate the photoelectron sheath (see Fig. 4.5(c)). As the spacecraft becomes more negative, it increasingly repels and accelerates the photoelectrons away from the surface (towards the right in Fig. 4.7), decreasing the photoelectron emissions' ability to surround the spacecraft. This further indicates that the electron emissions are more efficiently repelled as the spacecraft becomes more negative. This process is not as efficient as recollecting the emissions with

a positively charged spacecraft, so the barriers persist for more negative potentials. Larger barriers around bigger spacecraft also require more negative potentials to dispel the electron emissions. This causes the larger barriers from photoelectrons to persist for larger negative potentials than the smaller barriers from secondary electrons. It is again possible that a barrier smaller than one mesh element persists for more negative potentials than indicated, but the barrier size is most likely smaller than the energy of the emitted electrons.

The barriers on the wake side of the spacecraft disappear for small negative potentials and persist for larger positive potentials. This follows the trend for spacecraft wake formations, as large negative spacecraft potentials create a focused wake while large positive potentials create an enhanced wake. However, it is surprising that the barrier due to the wake disappears for negative spacecraft potentials of less than ten volts because the ion flow energy is 919.1 eV and 833.6 eV in the dayside and eclipse environment, respectively. This may be contributed to the process in which the wake creates a barrier in contrast with the nonmonotonic sheath. The barrier size of the wake when the spacecraft is uncharged is less than ten volts for the spacecraft sizes simulated, and it is likely that the barrier size in the wake remains constant. Then, once the spacecraft is more negative than the barrier there is no longer a noticeable dip in the potential. This also explains the trend for the wake side barrier about positive spacecraft, as the barrier remains close to its initial value as the spacecraft charge more positive. As a reminder, at highly positive potentials the spacecraft's surface potential attracts the majority of secondary electron and photoelectron emissions back into its surface. So in this region, the electron emissions are already expected to the repressed, but the wake may further prevent electrons from entering the wake-side region about the craft, as demonstrated in Fig. 4.5.

To review, as the spacecraft become larger the barrier size due to the spacecraft wake and nonmonotonic sheath increases, reducing the floating spacecraft potential. When holding the spacecraft at a constant potential, the barriers are largest when the spacecraft potential is smaller and width is larger, persist in the wake for more positive potential, and persist in the nomonotonic sheath for more negative potentials. In general, the barrier only exceeds 2 eV (the electron emis-

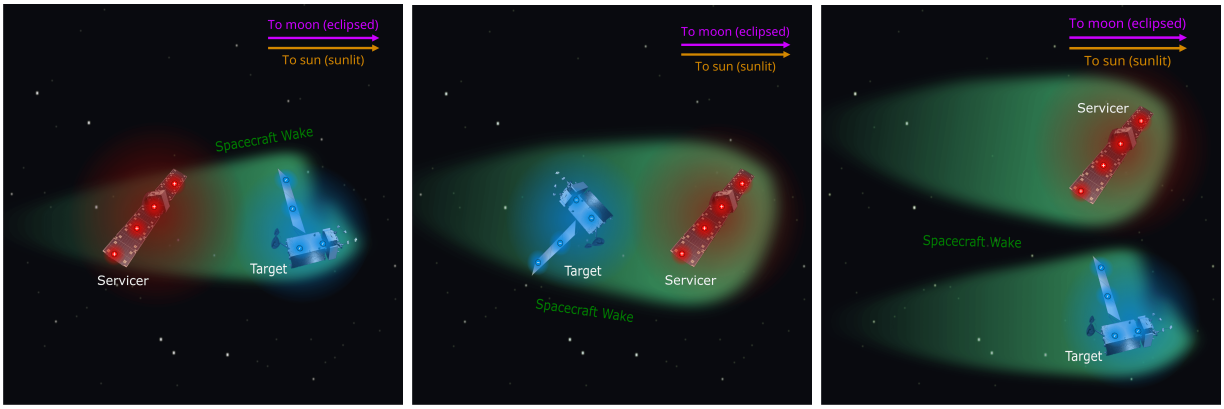

(a) Servicer in wake (b) Target in wake (c) Parallel wakes

Figure 4.8: Spacecraft positions for touchless potential sensing simulations

sion temperature) when the spacecraft width to Debye length is at least 0.5. Therefore, when the spacecraft width is smaller than this, barrier formations can largely be ignored, and barriers become more consequential as the spacecraft width gets larger.

4.3.3 Passive Potential Sensing Simulations

Passive potential sensing simulations are conducted to determine how barriers impact sensing and the conditions in which the servicer detects more emissions from the target. Based on the previous section, there are four sensing environments defined: (1) sunlit with a barrier ($W_{SC}=1\lambda_D$), (2) sunlit without a barrier ($W_{SC}=0.2\lambda_D$), (3) eclipse with a barrier ($W_{SC}=1\lambda_D$), and (4) eclipse without a barrier ($W_{SC}=0.2\lambda_D$). The servicer and target are the same size in all simulations and have a separation distance of one spacecraft width.

4.3.3.1 Characterization Results

In each environment, three relative spacecraft positions are simulated: servicer in target's wake, target in servicer's wake, and parallel wakes, as shown in Fig. 4.8. A constant potential servicer and floating potential target are modeled to determine how the servicer's potential changes the target's potential, emitted current, and detected current. In all environments and relative

Table 4.2: Passive Sensing Results

Servicer potential (V)	**SC width (m/λ_D)**	**Position**	**Target potential (V) (Sun / Eclipse)**	**Frac. of emissions recollected (Sun / Eclipse)**	**Detected emissions (A/m^2) (Sun / Eclipse)**
300	0.2	Servicer in wake	90 / 6.5	0.6 / 0.082	1.9E-6 / 2.2E-6
300	1	Servicer in wake	42.5 / 7	0.73 / 0.13	3.6E-7 / 2.1E-6
300	0.2	Parallel wakes	33.75 / 5.4	0.8 / 0.13	1.1E-6 / 2.3E-6
300	1	Parallel wakes	18 / 5.0	0.85 / 0.12	3.6E-7 / 1.4E-6
300	0.2	Target in wake	-70 / -25	0 / 0	0 / 7.5E-8
300	1	Target in wake	-100 / -32.5	0 / 0	0 / 6E-8
50	0.2	Servicer in wake	32.5 / 3.0	0.81 / 0.16	5.0E-6 / 9.4E-7
50	1	Servicer in wake	13 / 1.3	0.87 / 0.18	2.1E-6 / 8.3E-7
50	0.2	Parallel wakes	31.5 / 3.0	0.86 / 0.1	2.4E-6 / 6.3E-7
50	1	Parallel wakes	9.5 / 1.8	0.89 / 0.1	6.1E-7 / 4.0E-7
50	0.2	Target in wake	-32.5 / 3.3	0 / 0.14	5E-9 / 9.4E-7
50	1	Target in wake	-32.5 / -2.3	0 / 0.017	1E-8 / 6.5E-7
0	0.2	Target in wake	-23 / 1	0 / 0.1	1.25E-8 / 1.5E-7
0	1	Target in wake	-14.25 / -2.75	0 / 0.036	3E-8 / 1.75E-7

positions, the servicer is held at 50 V and 300 V. A 50 V servicer is highly likely to be more positive than the target, allowing it to attract emitted electrons. A 300 V servicer will attract and accelerate the ambient electrons, which may then impact the target with energy closer to E_{max} and increase the secondary electron yield. E_{max} is between commonly 280-800 eV for spacecraft surface materials, so a servicer potential of several hundred Volts could increase the yield from a variety of targets [121, 149]. A more positive servicer is not used because increasing the ambient electron energy significantly past E_{max} results in less detected current and a worse detected electron emission to ambient electron ratio, as shown in Chapter 3. As a worst-case scenario, a 0 V servicer is also modeled with the target in the servicer's wake, as this is the only orientation where it is likely that the target is charged negatively. The target's electron emissions that impact the side of the servicer facing the target are considered detected for touchless potential sensing, and emissions from the servicer are set to zero to ensure that servicer's own emissions are not falsely recorded as current for touchless potential sensing.

Table 4.2 and supporting Fig. 4.9 shows the relevant passive potential sensing results. When the target is not in the servicer's wake, it charges more positively than the individual spacecrafts charged in Section 4.3.2.1 because the servicer is drawing electron emissions away from the target,

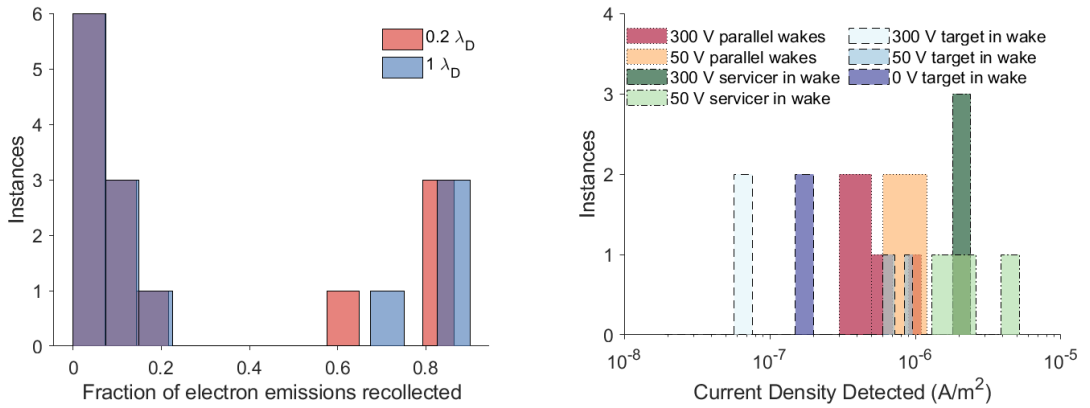

(a) Emission recollection vs size

(b) Detected current density vs servicer position and potential

Figure 4.9: Passive potential sensing results breakdown

effectively increasing its emissions current. In addition, when the target is larger it is seen that generally its potential is more negative, more current is recollected, and less current density is detected by the servicer. This follows expectations, as larger spacecraft are expected to have larger barriers. However, several of the target potentials are greater than ten volts positive, so nonmonotonic sheaths would not be expected to form. The difference in behavior can be explained by the size of the spacecraft relative to the photoelectron, secondary electron, and electron Debye lengths. For the larger spacecraft, the electron emissions settle closer to the target surface and the positive servicer's potential does not reach as far around the target. Both of these make it more difficult for the servicer to pull electron emissions away from the target for sensing. Figure 4.10 demonstrates this, as a higher density of photoelectrons travel farther from the smaller target's surface.

Regardless of size, when the servicer is more positive and the target is not in the servicer's wake, the target charges more positively and less emissions are recollected. This occurs because the more positive servicer may draw more electron emissions away from the target, which is further investigated in Chapter 6. For the eclipsed spacecraft, this correspond to a higher detected secondary electron current density. For the sunlit spacecraft, the higher potential servicer detects **less**

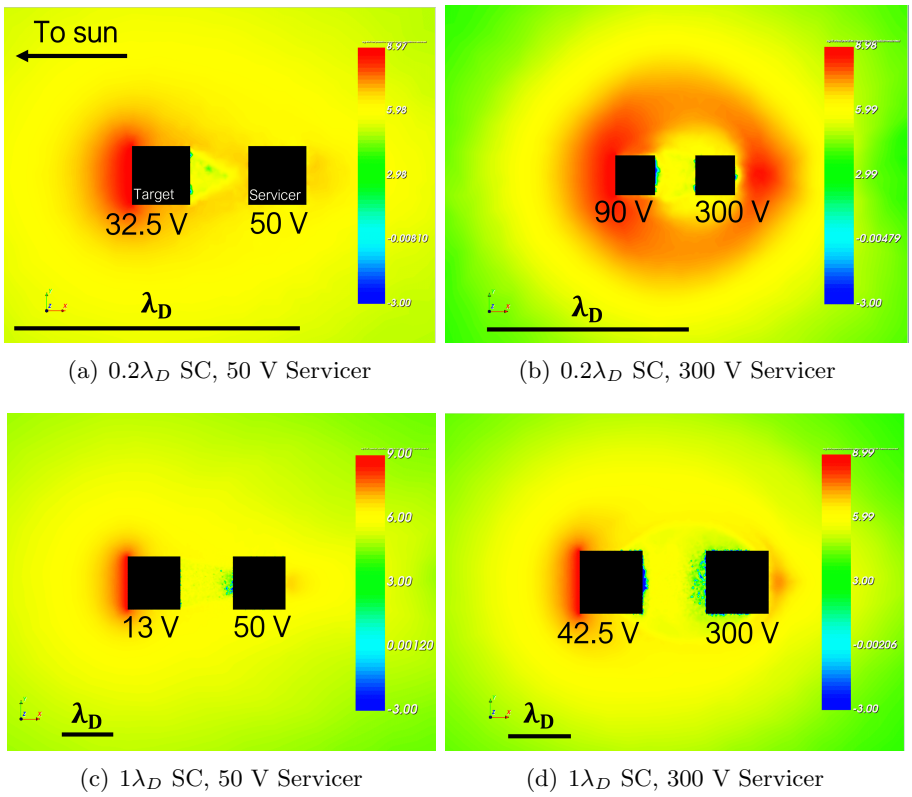

(a) $0.2\lambda_D$ SC, 50 V Servicer

(b) $0.2\lambda_D$ SC, 300 V Servicer

(c) $1\lambda_D$ SC, 50 V Servicer

(d) $1\lambda_D$ SC, 300 V Servicer

Figure 4.10: $\log_{10}$ of the photoelectron density about a target (left) and servicer (right) for the servicer in the target's wake.

current density. In this case, the photoelectron emissions is significantly larger than the secondary electron emission and the initially generated photoelectron current density does not vary with the target's potential. So, the photoelectron trajectories due to the spacecraft potentials is the main factor in the amount of detected current, not the secondary electron yield. Bengtson et al. [17] previously showed that a lower magnitude target potential is better for touchless potential sensing. When a more positive servicer generates a more positive target, the electron emissions are more influenced by the electric field about the target than the attractive force exerted by the servicer. This is demonstrated in the top two images of Fig. 4.10, where the photoelectron emissions are drawn nearly directly into the surface of the 50 servicer facing the target, while the emissions seem to orbit the 300 V servicer. Therefore, when the target is not in the servicer's wake a 50 V servicer is better when detecting photoelectron emissions, and a 300 V servicer is better when detecting

secondary electron emissions.

For both spacecraft sizes and in both the sunlit and eclipse environment, the servicer detects the most current when it is in the wake of the target. This is interesting because the wake is expected to serve as a barrier around a positively charged, larger target. Instead, the positive servicer is able to "punch through" barriers around the target and draw electron emissions in. This can be seen in Fig. 4.10, as the photoelectron emissions are drawn away from the target in all scenarios shown. Furthermore, the photoelectrons are present even in the regions to the right of the spacecraft where the wake barrier is expected, contrary to what is seen in Fig. 4.5(d) where the photoelectrons are repelled by the negative potential in the wake. Furthermore, the photoelectrons are present even in the regions to the right of the spacecraft where the wake barrier is expected, contrary to what is seen in Fig. 4.5(d) where the photoelectrons are repelled by the negative potential in the wake.

The discussion so far has only addressed results when the target is not in the servicer's wake. When the target is in the servicer's wake, the target generally charges negative, little to no electron emissions are recollected, and the detected current is lower than the other two orientations. Notably, no electron emission is detected when the servicer is 300 V positive. This occurs because the electron flux to the target exceeds the ion flux in the wake and charges the target negatively. At the floating potential, the negatively charged target repels the ambient electrons, as shown Fig. 4.11. It should be noted that an intermediate 20x20x20 m meshing grid with a resolution of 0.5 m is utilized to increase the resolution of the image. No changes are observed in the results when the intermediate meshing grid is implemented. Because the electrons are repelled from the target, they cannot create secondary electron emissions, so there is nothing to sense. While the wakes are classified as *narrow wakes* for all tested servicer potentials, the 50 V and 0 V servicer have slightly smaller wakes than the 300 V servicer, increasing the target's ion current and final potential. Electrons can then reach the more positive target and generate secondary electrons, albeit at a lower magnitude than in the other tested positions. Therefore, it is best to avoid putting the target in the wake, both for sensing and charging purposes, but if this configuration is unavoidable, a lower potential servicer is best when the target is in the servicer's wake. A conservative conclusion when no current is detected in

this configuration may be that the target has charged highly negative in the wake of the servicer.

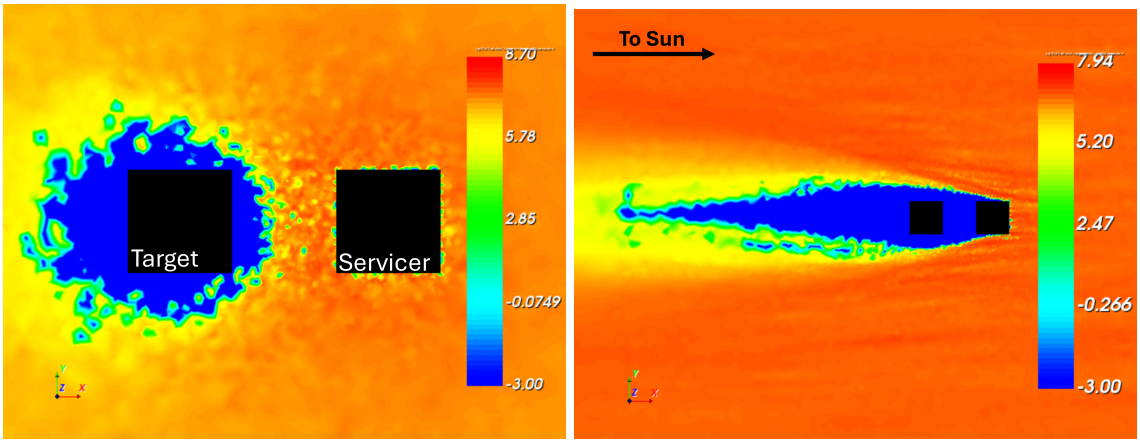

(a) Electron density (b) Ion density

Figure 4.11: $\log_{10}$ of the electron and ion densities about a $0.2\lambda_D$, 300 V servicer (right) and -70 V target (left) in the solar wind sunlit region.

4.3.3.2 Sensing Feasibility

Based on the previous section, the best case scenario for sensing is a $0.2\lambda_D$ length 50 V servicer in the target's wake when in a sunlit environment and a $0.2\lambda_D$ length 300 V servicer in the target's wake in an eclipse environment. In both environments, the worst case scenario is a target in the wake of a 300 V servicer. In any scenario, the detected electron emission current must be large enough to differentiate from the current due to the ambient electrons. An electrostatic analyzer (ESA), such as a Retarding Potential Analyzer (RPA), is proposed to measure the energy and flux of the electron emissions and ambient environment. The resulting measurements can be modeled as discrete energy bins with a width equal to the error in measurements. This is typically denoted as $\Delta E/E$ for electrostatic analyzer type instruments, and the energy resolution $\Delta E/E$ is assumed to be 4%, comparable to the resolution found by Bengtson et al. [19] ($\Delta E/E$ of 2.1% to 18%). The height of the bins is equal to the total detected current of electrons with energies between the min and max values of the energy bin.

The total measured ambient electron current $I_{\text{e,tot}}$ can be taken from SPIS and multiplied

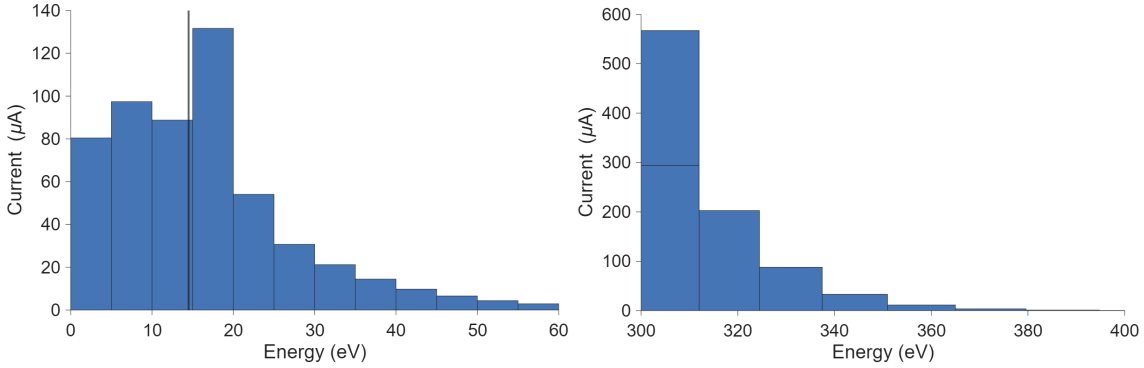

(a) 0 V Servicer, -14.5 V target, $1\lambda_D$ SC width, target in wake

(b) 300 V servicer, 6.5 V target, $0.2\lambda_D$ SC width, servicer in wake

Figure 4.12: Simulated ESA measurements for various sensing scenarios. The vertical line indicates the expected arrival energy of electron emissions from the target.

by the Maxwellian energy distribution function $f_E(E)$ to model the measured electron distribution ($I_e(E) = I_{\text{e,tot}} f_e(E)$). The Maxwellian energy distribution function is [110]

$$f_e(E) = \frac{2}{\sqrt{\pi} T_e^{3/2}} \sqrt{E} \exp\left(\frac{-E}{T_e}\right), \tag{4.5}$$

where E is the energy in eV. The detected electrons are accelerated by the potential of a positively charged servicer, so the spectrum is shifted such that the minimum detected energy is equal to the servicer's surface potential.

Various models exist for the energy distribution of electron emissions $f_{se/ph}(E)$, including the Chung-Everhart model [41] (which is referenced in Chapter 2), a Gaussian fit with a logarithmic argument [174], and a Maxwellian distribution. As mentioned in Section 4.3.1, SPIS models the electron emissions as a Maxwellian distribution with a temperature of 2 eV. To keep the feasibility analysis consistent with the characterization results in SPIS, a Maxwellian distribution is used to model both photoelectron and secondary electron emissions. As mentioned in Section 1.2.3, the electron emissions are accelerated away from a negative target and towards a negative servicer such that the energy of the secondary and photoelectron emissions $E_{SE/Ph}$ at detection is

$$E_{SE/Ph} = T_{se,ph} f_{se/ph}(E) + V_{\text{ser}} - V_{\text{tar}}, \tag{4.6}$$

where V_{ser} and V_{tar} are the servicer and target's potential, respectively. If the target is charged

positively, it is assumed that the electron emissions leave the target with negligible initial energy, or $V_{\text{tar}} \approx 0$ V. The detected ambient electron and electron emission currents are then superimposed to model the complete detected spectrum.

Figure 4.12(a) is an example of measurements in a scenario where the target is in the wake of a 0 V servicer in the dayside environment. A shown, the bin with the secondary electron emissions is over 200 μA larger than the next tallest bin, indicating that the electron emissions can be distinguished from the ambient environment. Figure 4.12(b) is an example of a setup where a 300 V servicer is in the wake of the target in the eclipse environment. The target is charged positively, so the electron emissions are captured in the first energy bin, which is over twice as large as the next bin. In addition, the horizontal line in the first bin indicates an initial measurement of the environment without secondary electron emissions, which is approximately half the size of the bin when the electron emissions are detected. Therefore, the electron emissions can be differentiated from the environment in both tested cases, so long as the energy resolution of the detection instrument is sufficient (not significantly larger than 4%).

4.4 Active Potential Sensing

In a similar manner in which secondary and photoelectron emissions generate nonmonotonic sheaths, it is possible that electron emissions from an electron beam can generate a potential barrier. If the electron beam current is large enough, the concentration of electrons can generate a barrier that prevent further electrons from passing through. This concept was introduced in Section 2.2.4 during the computation of the SCL current. Therefore, the electron beam behavior when emitted from an isolated spacecraft is tested to first investigate the barrier formations. Then, active touchless potential sensing scenarios are simulated to determine if barriers can form and the feasibility of detecting actively emitted secondary electrons.

The simulation setup is similar to that described in Section 4.3.1. Now, a 2 cm wide square plane is defined in the center of the servicer face that is directed towards the target. This flat plane is define as a *source* in SPIS such that electrons with a specified current density, initial half

angle of spread, and energy are emitted. The current density is defined in the "Group Parameters" tab, and the energy and half angle are defined using the `AxisymTabulatedVelocitySurfDistrib` option in the "Global Parameters" tab[1] . The half angle is set to 2° for all simulations, and the energy is held at 1 keV to excite secondary electron emissions, based on the results from Chapter 2. Secondary electrons due to the electron beam along with those emitted by the environment are enabled in the "Global Parameters" tab by setting `electronSecondaryEmission` to 195.

4.4.1 Electron Beam Barriers

4.4.1.1 Single Spacecraft

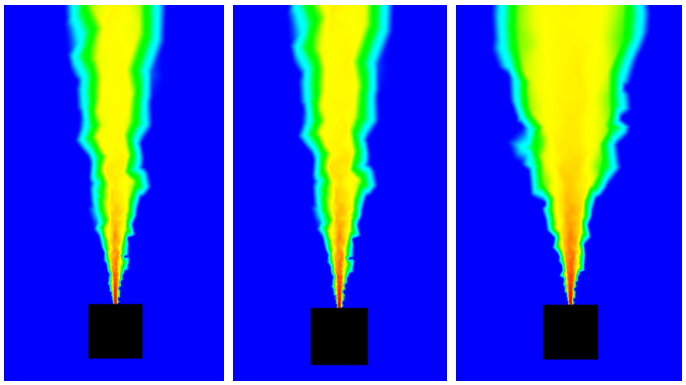

(a) 0.1 mA (b) 1 mA (c) 10 mA

Figure 4.13: $\log_{10}$ of the electron beam density from a 0 V spacecraft.

The spacecraft potential is first held at 0 V and the beam current is varied to investigate the worst-case barrier formation, as it was shown in Section 4.3.2.2 that the largest barriers form when the spacecraft is uncharged. The electron beam charge density from a 0 V, 1 λ_D width spacecraft for varying beam currents is shown in Fig. 4.13. The beam has an initial divergence, so the radius of the beam becomes wider as the distance from the spacecraft increases. This may also be exacerbated by the mesh size increasing as the resolution becomes more coarse between the spacecraft surface and computational boundary. In Fig. 4.13(c), the 10 mA beam becomes wider

[1] For more information on formatting the `AxisymTabulatedVelocitySurfDistrib` input file in SPIS, see the discussion in the SPIS forum at SPIS Forum Post.

closer to the spacecraft than the lower current beams. At this current, the density of the electrons is large enough that space charge is no longer negligible and the electrons are repelling each other. Fortunately, the SCL current has not been exceeded and the beam crosses the entire computational space. The space charge repulsion can be positive for touchless potential sensing because a wider beam is shown to increase the observability of a charged target in Chapter 2. Conversely, this could decrease the fraction of the electron beam that impacts a target during electrostatic tractor operations, decreasing the electron beam current to the target and the magnitude of the resulting target potential.

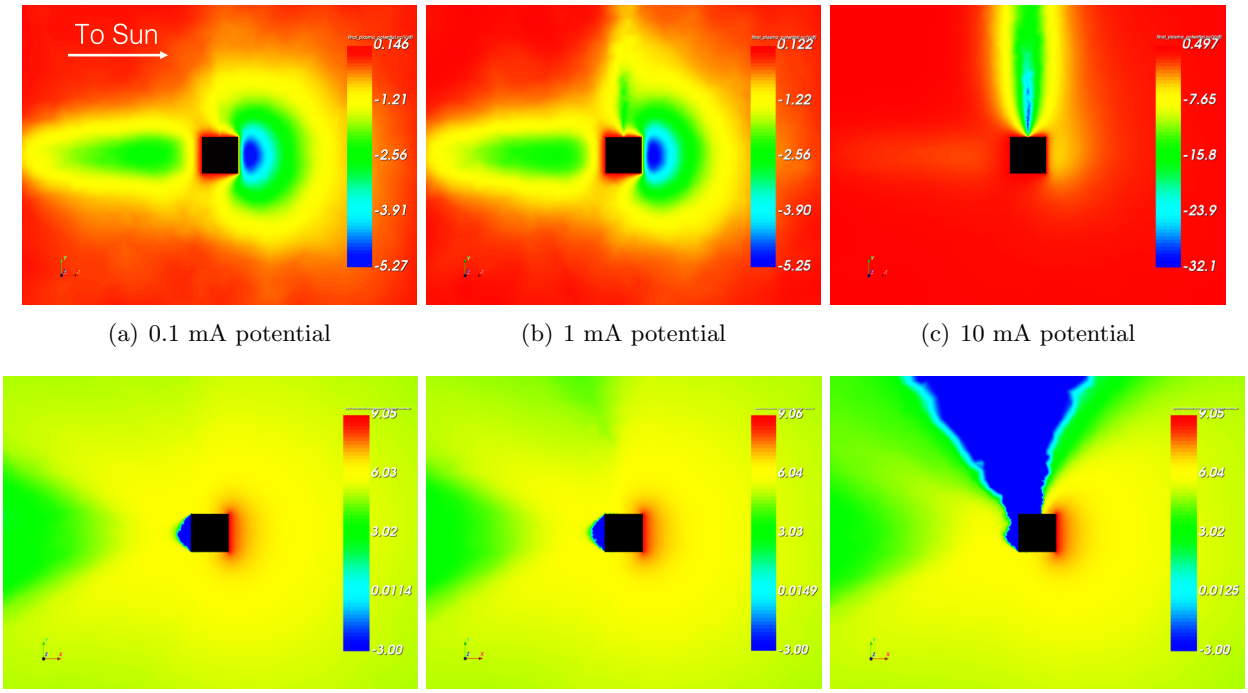

(a) 0.1 mA potential (b) 1 mA potential (c) 10 mA potential

(d) 0.1 mA photoelectron density (e) 1 mA photoelectron density (f) 10 mA photoelectron density

Figure 4.14: The potential (top) and $\log_{10}$ of the photoelectron density (bottom) around a 0 V spacecraft with varying beam currents.

The potential and photoelectron density around an uncharged spacecraft with varying beam current is shown in Fig. 4.14. In these images, the beam is emitted perpendicular to the flow of the ions. It can be seen that the barrier formations become larger as the beam current increases, following the trends seen for increased secondary electron and photoelectron emissions. In fact,

when the beam current is 10 mA, the negative potential barrier due to the beam is ≈32.1 V, larger than any of the barriers presented in Fig. 4.6. This then creates a large region that the photoelectrons cannot penetrate near the beam. Thus, it is possible for a high current beam to repel electrons when the spacecraft potential is low.

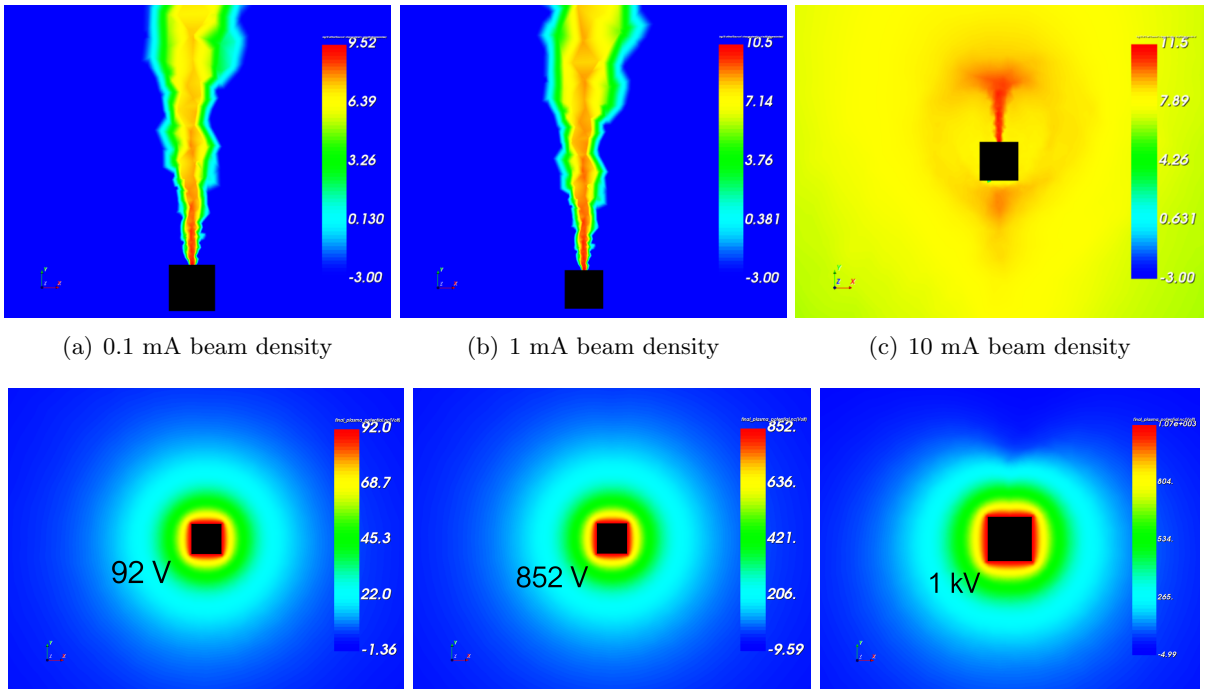

(a) 0.1 mA beam density (b) 1 mA beam density (c) 10 mA beam density

(d) 0.1 mA potential (e) 1 mA potential (f) 10 mA potential

Figure 4.15: The $\log_{10}$ of the electron beam density (top) and potential (bottom) about a floating spacecraft with varying beam currents.

Figure 4.15 shows that once the servicer is allowed to charge due the to electron emissions, the barriers disappear. The most notable behavior occurs at the largest beam current. The spacecraft charges to the same energy as the beam and begins to recollect the emitted electrons. The electron beam surrounds the positive spacecraft and creates an electron sheath, similar to the concept of a photoelectron sheath.

Overall, if a servicing spacecraft has a low surface potential and high beam current, it is possible for barriers to form. Typically, a high beam current causes large surface potentials, which then results in a negligible barrier. Technology such as pulsing can enable the use of higher currents

while minimizing the change in surface potential [83]. In this case, the electron gun current should be restricted to avoid barrier formations. This work only models a continuous beam in SPIS, and implementing pulsing into SPIS simulations is recommended for future work.

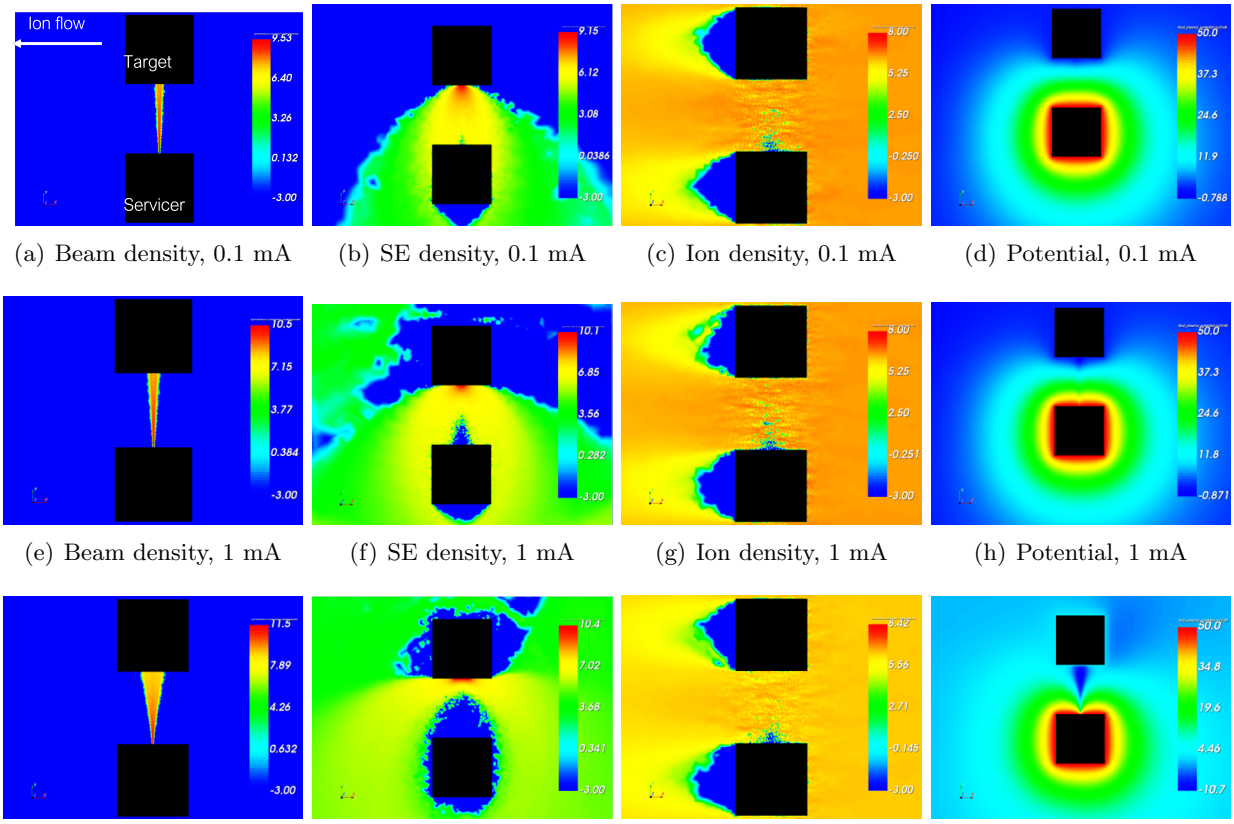

(a) Beam density, 0.1 mA (b) SE density, 0.1 mA (c) Ion density, 0.1 mA (d) Potential, 0.1 mA

(e) Beam density, 1 mA (f) SE density, 1 mA (g) Ion density, 1 mA (h) Potential, 1 mA

(i) Beam density, 10 mA (j) SE density, 10 mA (k) Ion density, 10 mA (l) Potential, 10 mA

Figure 4.16: $\log_{10}$ of particle densities and potential results for a 50 V servicer impacting a 1.8 V target with a 1 keV, electron beam with various currents.

4.4.1.2 Sensing Simulations

A target spacecraft is now included in the simulations such that it is impacted by the servicing spacecraft's electron beam. First, a simulation is conducted while the spacecraft are held at a constant potential to investigated a case in which high beam current, low potential spacecraft occur and barriers may form. Then, the spacecraft are allowed to float to simulate the full interactions expected when the servicer directs an electron beam at a target.

A 1 λ_D width servicer and target are held at 50 V and 1.8 V in the solar wind eclipse environment with parallel wakes based on the passive sensing results from Table 4.2, and the electron beam current is varied. Figure 4.16 shows the particle densities and potential results for a 1 keV beam with various currents. Once again, as the beam current increases the width of the beam increases due to space charge repulsion. The higher current electron beams also create a distinct barrier seen in the secondary electron density and potential results. In fact, when the beam has a current of 10 mA, a 10.7 V barrier is generated and no emitted secondaries from the target impact the servicer. Therefore, if high beam current and low spacecraft potentials occur, it is possible for barriers for form that prevent the servicer from collecting electron emission current for touchless potential sensing.

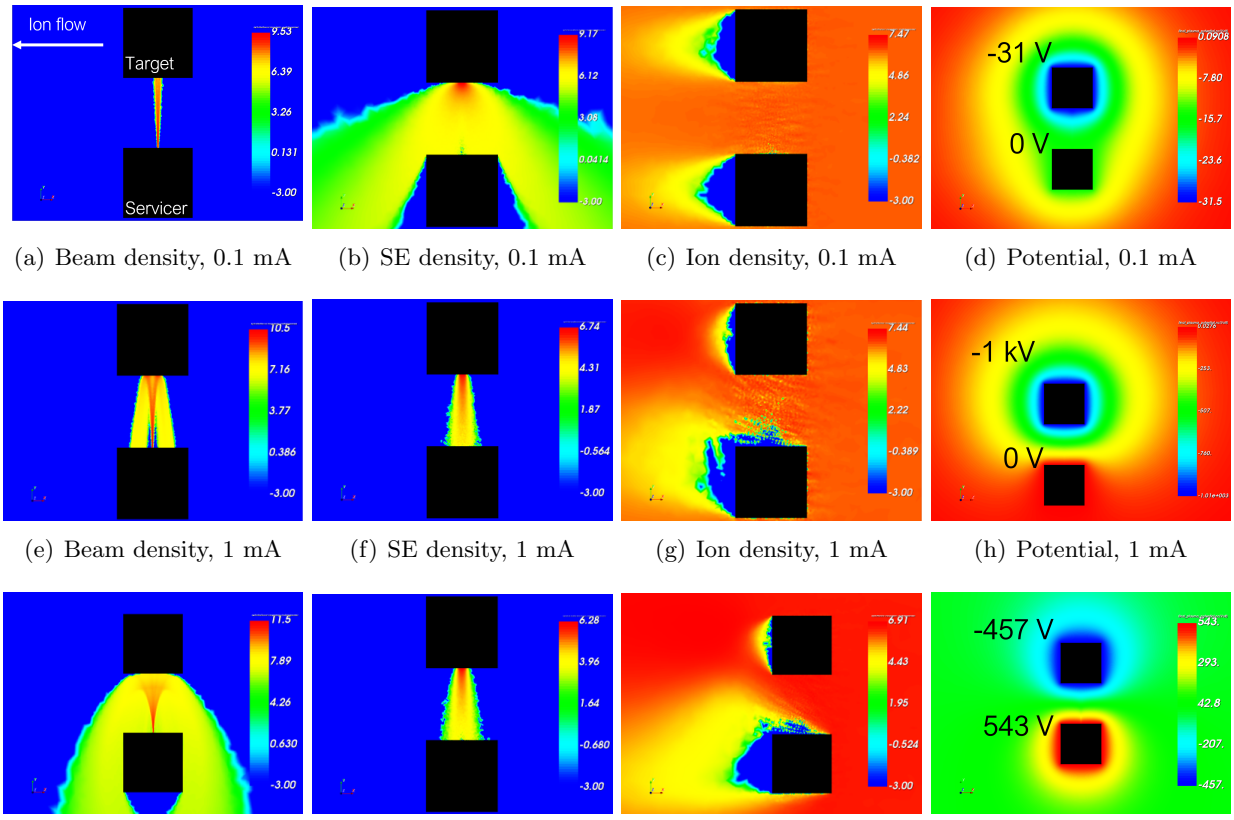

(a) Beam density, 0.1 mA (b) SE density, 0.1 mA (c) Ion density, 0.1 mA (d) Potential, 0.1 mA

(e) Beam density, 1 mA (f) SE density, 1 mA (g) Ion density, 1 mA (h) Potential, 1 mA

(i) Beam density, 10 mA (j) SE density, 10 mA (k) Ion density, 10 mA (l) Potential, 10 mA

Figure 4.17: $\log_{10}$ of particle densities and potential results for a servicer impacting a target with a 1 keV, electron beam with various currents.

Now, the spacecraft are allowed to float and the simulations are repeated. As seen from the results in Fig. 4.17, barrier formations are not observed when the spacecraft are allowed to charge. At 0.1 mA, the target only charges to -31 V, but the beam current is not large enough to generate a barrier. At the larger beam currents, the difference in potential between the servicer and target is equal to the beam energy and no barriers are detected within this higher surface potential system. Therefore, in electrostatic tractor operations where a beam is utilized to create large potentials on the servicer and target, it is unlikely for a barrier to form even with a high current electron beam.

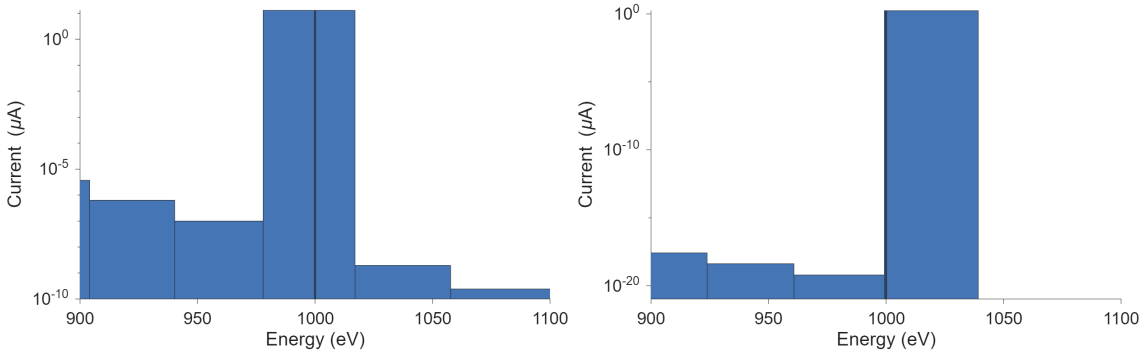

(a) 10 mA beam, 543 V servicer, -457 V target (b) 0.1 mA beam, 0 V servicer, 1 kV target

Figure 4.18: Simulated ESA measurements for various active potential sensing scenarios. The vertical line indicates the expected arrival energy of electron emissions from the target.

4.4.2 Sensing Feasibility

The analysis conducted in Section 4.3.3.2 is repeated for active potential sensing. Figure 4.18(a) shows the results for a servicer with a 10 mA electron beam in solar wind eclipse and parallel wakes. The difference in potential is 1 kV, as indicated by the vertical line. The current in the bin containing the emissions from the target is orders of magnitude larger than the surrounding bins, so this measurement is easily distinguishable from the ambient electron flux. Figure 4.18(b) shows the measurement to a servicer with a 0.1 mA beam directed at a target in the servicer's wake in the solar wind dayside environment. In this scenario, the target charges to the beam energy and the servicer remains uncharged, so the difference in potential is again 1 kV.

The bin with the target's emissions is again orders of magnitude larger than the surrounding ones. Thus, active potential sensing of charged spacecraft in dense cislunar plasma is feasible.

4.5 Conclusions

Barriers due to spacecraft wakes and nonmonotonic sheaths can prevent electron emissions used for touchless potential sensing from being detected. The barriers are characterized about spacecraft of varying widths and potentials in solar wind dayside and eclipse plasma. It is found that barriers can form when the spacecraft width is at least half the Debye length and are largest when the spacecraft is uncharged. Barriers due to nonmonotonic sheaths persist as the spacecraft charges more negative, while barriers due to the spacecraft wake persist as the spacecraft charges more positive.

Simulations of passive potential sensing when barriers are expected ($W_{SC} = 1\lambda_D$) and not expected ($W_{SC} = 0.2\lambda_D$) reveal that fewer electron emissions leave a target and the detected current density is lower when barriers are expected. However, sensing is not fully prevented because a positively charged servicer is able to draw electron emissions through anticipated barrier formations, such as the target's wake. When the target is not in the servicer's wake, a 50 V servicer is best for detecting photoelectrons, and a 300 V servicer is best for detecting secondary electrons. When the target is in the servicer's wake, a highly positive servicer can begin to enhance the wake formation, leading to less ion current to the target and a highly negative surface potential. This then prevents ambient electrons from impacting the target and generating electron emissions. Therefore, placing the target in the servicer's wake should be avoided for both charging and sensing purposes, and the servicer's potential should be minimized if this configuration is necessary. It is likely that other constraints are present during proximity operations that can prevent the servicer from positioning itself to detect the target's potential. Regardless, these results can be utilized to position the servicer to detect the target's potential prior to docking, or to the inform operators why electron emission measurements from the target may not be detected during proximity operations.

When an electron beam is utilized to generate emissions for touchless potential sensing, it is

possible for the beam to create barriers if the beam current is large ($\geq$1 mA) and the spacecraft potential is low. Fortunately, setting a large beam current generally results in a large spacecraft potential, allowing barriers from the beam to be avoided for most scenarios.

In realistic environmental conditions, the electron emissions passively and actively generated from a target can be differentiated from the environment, showing that touchless potential potential sensing through barriers in cislunar space can be conducted to achieve both scientific and safety goals.

Chapter 5

Vacuum Chamber Wake Development

5.1 Motivation

Numerical programs, such as Nascap-2k and SPIS, are excellent resources to provide insight into spacecraft-plasma interactions; however, complex particle-in-cell simulations can also take hours to days to converge for a single configuration, requiring significant computational power and time to obtain results. Furthermore, these programs include assumptions about the space environment and interactions that may decrease the accuracy of the results. Therefore, it is desirable to complement numerical simulations with experimental results to validate that the modeled behavior acceptably represents realistic scenarios. As shown in Chapter 4 and will be shown in Chapter 6, spacecraft wakes can significantly alter the charging and sensing behavior, and the potential of the spacecraft influences the size of the wake. Therefore, it is of particular interest to investigate cislunar wake formation using both numerical and experimental techniques. This chapter focuses on enabling spacecraft wake generation in the Electrostatic Charging Laboratory for Interactions between Plasma and Spacecraft (ECLIPS) vacuum chamber located at the Autonomous Vehicles Systems (AVS) Laboratory at the University of Colorado Boulder. Enabling wake experiments in the ECLIPS chamber, as opposed to traveling to other facilities, increases experimental efficiency by eliminating the need to travel and coordinate with external laboratories.

Ion wake experiments typically involve an ion or plasma source, an object to obstruct the flow of plasma, and sensors such as Langmuir probes (LPs) and Faraday cups to determine the properties of the plasma. It would be straightforward to implement a similar setup in the ECLIPS

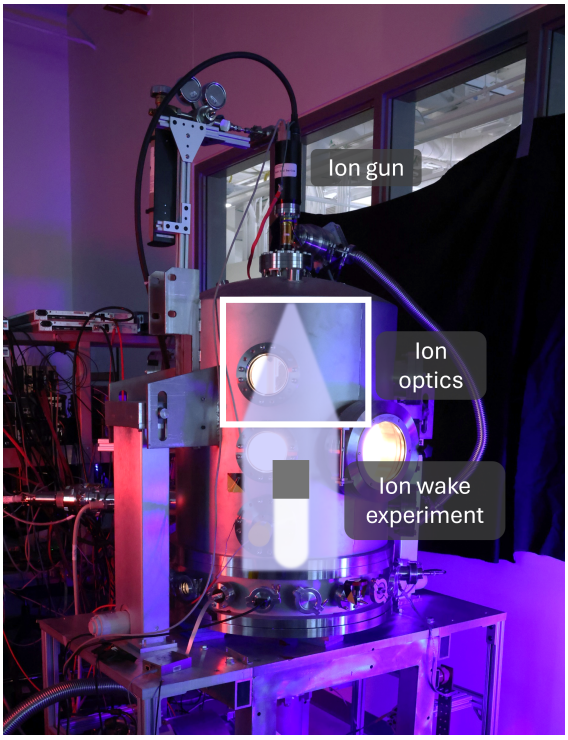

Figure 5.1: Proposed ion wake experimental implementation in the ECLIPS vacuum chamber

vacuum chamber; however, the 1402 Ion Gun from Non Sequitur Technologies installed in the ECLIPS chamber emits a narrow ion beam that significantly limits the object size that can be used to generate a wake and makes obtaining measurements of the wake difficult. For example, a cube with a minimal width of 5 cm is required for touchless potential sensing experiments based on previous experiments. This allows the entire electron gun to impact the face of the cube. Furthermore, there should be at least 1 cm of ions surrounding the cube to ensure measurements can be made of the fast-flowing ions and wake formation. Half of the diagonal of a 5 cm cube is approximately 3.55 cm, so the beam should have a radius of at least 4.55 cm. In addition, the beam expands radially outwards throughout the length of the chamber, which likely does not represent the flow expected in cislunar plasma. Spacecraft wake experiments have been conducted utilizing an expanding plasma source, so limiting the expansion of the ion flow is ideal but not a strict requirement. To ameliorate this limitation, charged particle optics are utilized to expand and refocus the beam such that the beam is large enough to fully envelop an object and flow parallel

to the chamber walls. This is referred to as telescoping the beam, as shown in Fig. 5.1.

Charged particle optics involves manipulating the trajectory of charged particles by altering the ambient electric or magnetic field and has been a topic of study since the early 20th century, with several publications outlining the general concepts [45, 52, 122, 183]. Altering charged particle trajectories has been used to focus ion beams for mass spectrometry [31, 209], radiotherapy for cancer patients [12], sample etching and preparation [114, 167], investigating irradiation effects on materials [184, 212], and more.

Electrostatic, magnetic, or a combination of the two types of lenses can be used to manipulate the ion beam as desired. Low energy ion (5 eV to 50 keV) trajectories are generally altered more by varying electrostatic fields versus magnetic fields [52]. Furthermore, implementing simple electrostatic lenses allows for for easy adaptability and implementation in other vacuum systems, where the results could also be extended to any experiment in which it is beneficial to expand the installed ion gun's capability to manipulate the ion beam. Accordingly, electrostatic lenses held at constant potentials are designed and utilized to manipulate the ion beam, and the resulting lens configuration and characterization is the primary contribution to the current state of ion wake experiments.

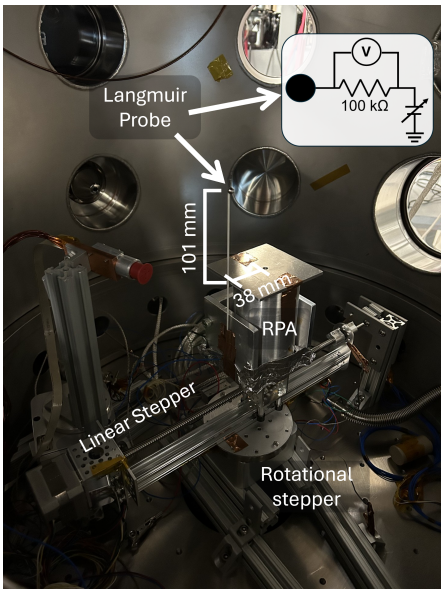

Figure 5.2: Sensor package and Langmuir probe circuit

The materials and methods used to characterize the ion beam and the state of the unaltered beam is first presented. Next, the electrostatic lens configuration results calculated in SIMION results are discussed. Last, installation and experimental characterization of the lenses is presented.

5.2 Experimental Setup

5.2.1 Cislunar Plasma Experimental Representation

The wake experiment is limited by the experimental volume available in the ECLIPS chamber, which has a height of ≈86 cm and a diameter of ≈60 cm. The ion lenses are restricted to the top 50 cm of the chamber to leave sufficient room for experiments. Despite the size of the ECLIPS chamber, large scale phenomena can still be represented. A scaling law can be applied to relate the spacecraft's experimental radius R_0 to the radius in the environment of interest R_{sim} [33]

$$R_{\text{sim}} = \sqrt{\frac{n_i}{n_{\text{sim}}}} R_0, \tag{5.1}$$

where n_i is the experiment ion density and n_{sim} is the environment ion density. In other words, if the density of the experimental ion beam is larger than the environmental plasma density, the experimental object represents a larger spacecraft. This relationship was derived for LEO plasma-body interactions, but it applies to processes governed by the Vlasov-Maxwell equations [33]. Thus, this may be applied to cislunar plasma environments where spacecraft wakes form. The density of the ions in the ECLIPS chamber is

$$n_i = \frac{I_{\text{beam}}}{q_e A v} = \frac{I_{\text{beam}}}{q_e \pi r^2} \sqrt{\frac{m_i}{2E}}, \tag{5.2}$$

where I_{beam} is ion gun current, q_e is the elementary charge in Coulombs, A is the final area of the beam, or πr^2, v is the velocity of the ions, m_i is the mass of the ions, and E is the energy of the ions, found as $E = 1/2 m_i v^2$ assuming non-relativistic ions.

The argon ions (Ar^+) generated in the ECLIPS chamber are not representative of cislunar plasma environments, which are comprised mostly of Hydrogen ions (H^+). Fortunately, there is

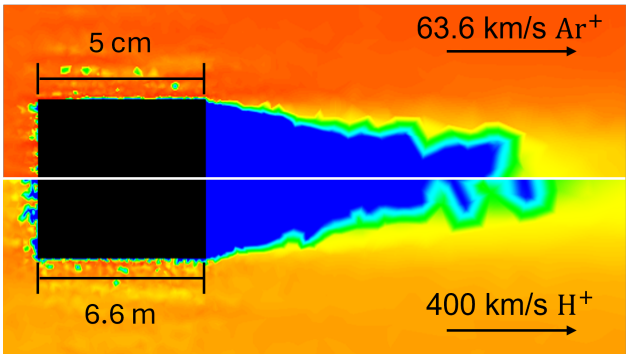

Figure 5.3: Ion wake formation ($\log_{10}$ of the ion density) about scaled spacecraft.

another scaling law from Ref. [33] that can be used to relate the velocity of two different ion species

$$v_{\text{sim}} = \sqrt{\frac{m_i}{m_{\text{sim}}}} v, \tag{5.3}$$

where v_{sim} is the velocity of the environment being simulated and m_{sim} is the mass of the ions in the simulated environment. Spacecraft wakes form in the cislunar magnetosheath and solar wind regions, which have H^+ bulk velocities from 350 to 930 km/s [117]. Hydrogen ions with a bulk velocity of 400 km/s reasonably represents solar wind or magnetosheath conditions, which corresponds to Ar^+ ions with a velocity of 63.6 km/s, or a beam energy E_B of approximately 835 eV. The beam is held at this energy in all simulations and experiments.

Figure 5.3 shows the ion wake formation around a 5 cm wide cube in 63.6 km/s, 1.04E11 m^{-3} Ar^+ ions and a 6.6 m cube in 400 km/s, 6E6 m^{-3} H^+ ions with a thermal ion temperature of 7 eV in both plasmas. The wake formations approximately match in both scenarios, validating that the scaling laws are appropriate to correlate the experimental results to cislunar mesothermal plasma.

5.2.2 Ion Beam Characterization

A spherical Langmuir probe and Retarding Potential Analyzer (RPA) are used to take measurements of the ion beam at different positions, shown in Fig. 5.2. The LP is constructed from a 2.5 mm radius aluminum sphere spot welded to nickel wire. The wire is electrically isolated and held in place with a ceramic tube. Before each experiment, the LP is bombarded with 3 keV ions,

the highest energy possible with the ion gun, and held at -1 kV to remove surface contamination. A sweep outside the ion gun is then conducted to obtain measurements of the expected noise level, or the load line. The load line is subtracted from the final measurements during analysis [120]. This noise is generally two orders of magnitude smaller than the measurements obtained in the ion gun. The Langmuir probe is swept from 0 to -100 V in 10 V steps using a Matsusada AU-IR30 High Voltage Power Supply (HVPS), and the voltage change across a 100 kΩ resistor is measured using a Keithley DMM6500 multimeter. The voltage change is then converted into collected current using Ohm's Law ($V = IR$). It should be noted that the multimeter has an internal resistance of 20 MΩ, which is added to the circuit resistance when converting the measured change in potential to collected current. These measurements generate a current versus potential (I-V) curve in the ion saturation region [40]. The Langmuir probe theory presented in [125] is implemented in MATLAB and utilized to obtain the ion current density results presented. The RPA was previously constructed from a Faraday cup with a front grounding grid followed by a biasing grid [204]. An aluminum sheet is placed in front of the RPA's entrance to decrease the entrance aperture to a circle with a radius of 2.4 mm. This makes the RPA entrance comparable to the size of the LP and allows for measurements to be taken in 5 mm steps. The RPA is located approximately 460 mm from the ion gun exit, and the LP is positioned approximately 101 mm higher than the RPA, or 359 mm from the ion gun. Both instruments are placed on a linear stepper motor capable of moving the sensors ±10 cm from the center of the chamber and a rotational stepper capable of rotating 360°. This allows the entire space to be characterized with a resolution of 5 mm.

To determine if the ion beam is symmetrical and characterize the initial spread of the beam, a current density map of the ion beam is obtained, shown in Fig. 5.4. The beam is not perfectly symmetric, but edge points can be used to determine an average beam radius. The average beam radius is 3.84 cm as measured by the RPA and 3.15 cm as measured by the LP. Based on this, and assuming an initial radius of 1 mm at the ion gun exit, the half angle of the beam is estimated to be ≈4.9°.

It is surprising that the current density measured by the LP is smaller than that measured

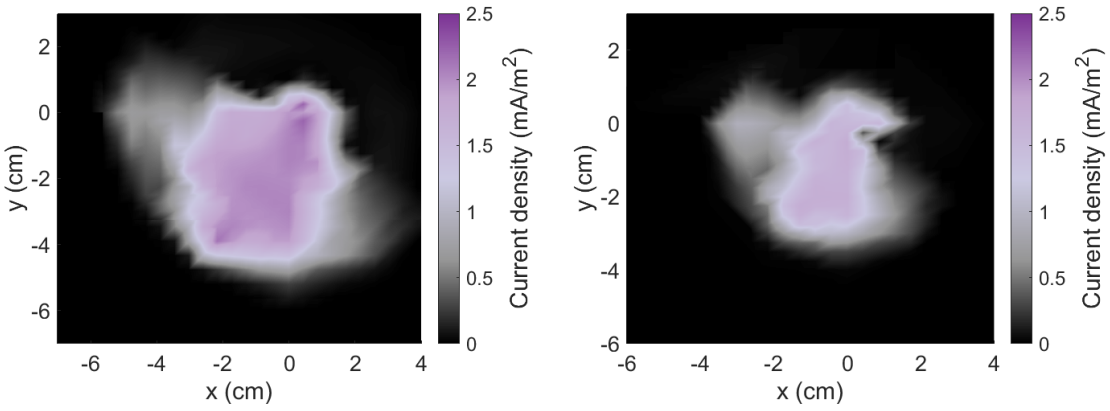

(a) RPA measurements (b) LP measurements

Figure 5.4: Current density map of the unaltered ion gun emissions measured by the Retarding Potential Analyzer and Langmuir Probe

by the RPA because the LP is located in a region of the beam with a smaller radius and higher current density. However, Langmuir probes are often stated to have accuracy of 20 to 50% of real values [40, 125], and contamination and secondary electrons emitted from the chamber and RPA can alter the current magnitude. Regardless, the magnitude of the current density measured by the LP does not change the results of this project because the edge points of the current measurements are used to determine the size of the beam. This process is further described in Section 5.4.1.

5.3 Particle Tracing and Optimization Approach

Three lens configurations are considered for installation in the ECLIPS vacuum chamber: two thin lenses, three thin lenses, and three thick lenses, as shown in Fig. 5.5. The thin lenses are flat, thin plates with openings of radius R_{lens} to allow the beam to pass through. The thick lenses are thin cylindrical shells that again allow the ion beam to pass through the center. Each thin lens has three parameters: location x_{lens}, electric potential V_{lens}, and inner radius R_{lens}. Each thick lens has a variable thickness L_{lens} and potential. The thick lenses all have the same radius, and the top of the first lens is in line with the ion gun opening. The final lens configuration can then have anywhere from six to nine variables.

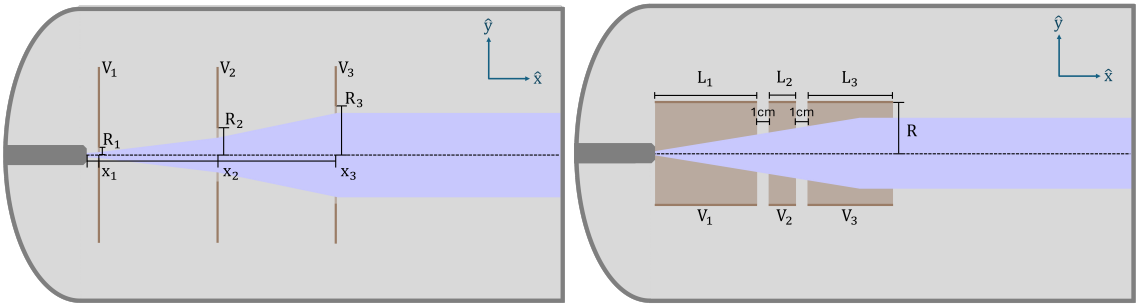

(a) Thin lens (b) Thick lens

Figure 5.5: Thin and thick lens schematics.

SIMION is used to design and investigate the electrostatic lenses. To efficiently optimize the design of the lenses, a windows batch file is written to enable MATLAB to alter the lens parameters and run a SIMION simulation. Then, a genetic algorithm and fminsearch in MATLAB are used to minimize an associated cost function. A genetic algorithm is a method for solving constrained or unconstrained optimization problems based on a natural selection process that mimics biological evolution. The algorithm is proficient at finding the approximate absolute minimum for the entire problem space, but the solution is not as accurate as MATLAB's fminsearch. MATLAB's fminsearch is a nonlinear programming solver that finds the minimum of a specified function and is proficient at determining local minimum near a defined starting point. Therefore, a genetic algorithm is first implemented, and then the results are used as the initial guess for fminsearch, taking advantage of the capabilities of both functions.

The goal of this study is to maximize the final radius of the beam and minimize the spread of the beam in the direction parallel with the ground of the chamber, which is defined as the y-direction. In addition, the lenses may accelerate the ions, so the difference between the final velocity and 63.6 km/s should be minimized. The cost function is then

$$\text{Cost} = w_y \frac{n}{y_{\max}^2} + w_{v_y} \text{sum}(v_y^2) + w_{v_x} \text{sum}((v_x - 63.6)^2), \tag{5.4}$$

where $y_{\max}$ is the maximum radius achieved by an ion particle, n is the number of particles flown, w_y is the weight applied the final radius, v_y is the final velocity of each particle in the y-direction, w_{v_y}

Table 5.1: Lens design constraints

Parameter	**Constraints**
E_B	825 eV $\leq E_B \leq$ 845 eV
V_{lens}	-30E3 V $\leq V_{lens} \leq$ 30E3 V
R_{lens}	$5 \leq R_{lens} \leq 250$ mm
x_{lens}	$x_3 \geq x_2$+100 mm $\geq x_1$+100 mm; $x_1 \geq 101$ mm; $x_2 \leq 500$ mm (2 thin lenses); $x_3 \leq 500$ mm (3 thin lenses)
L_{lens}	$L_1 + L_2 + L_3 \leq 380$ mm

is the weight applied to minimizing the spread of the particles in the y-direction, v_x is the velocity of each particle in the x-direction, and w_{v_x} is the weight applied to minimizing the variance of the final velocity from the defined optimal velocity, 63.6 km/s. Only the maximum value of the radius component is used $y_{\max}$ because particles that impact near the center of the chamber have a minuscule final position in the y-direction, resulting in an uncharacteristically high cost function. The velocity components of the cost function sum the final velocity of all the particles, which creates higher values compared to the final position of a singular particle. So, the radius component is multiplied by the number of particles to make the values of each component of the cost function comparable. In addition, if the potential of the lens is too high, the particles will be attracted back towards the lenses and impact them. To avoid this solution, the cost function is automatically given a value of 1E10 if the final position of the particles are not at the floor of the chamber.

The constraints must be selected such that the final lens design fits inside the available experimental area and is within the bounds of the technology available in the ECLIPS chamber. The beam energy E_B is allowed to vary ±10 eV from the optimal energy in order to account for change in velocity due to the lenses, and the possible potential of the lenses V_{lens} is constrained by the capabilities of the Matsusada AU-30R1 HVPS, ±30 kV. The ion gun exit has a radius of 4 mm, so radius of the space in the center of the lenses R_{lens} is set to a minimum of 5 mm to ensure

the lens don't block the opening. The maximum radius is 250 mm to allow space for stands to be installed on the outside of the lenses. The ion gun is 100 mm long, and the lenses must be placed in the top 500 mm of the chamber to leave space for wake experiments to be conducted. For the thin lenses, this means the lens locations x_{lens} must be greater than 100 mm and less than 500 mm. The thick lenses have set separation distances of 100 mm, so the combined length of the lenses L_{lens} must be less than 380 mm. These constraints are shown in Table 5.1.

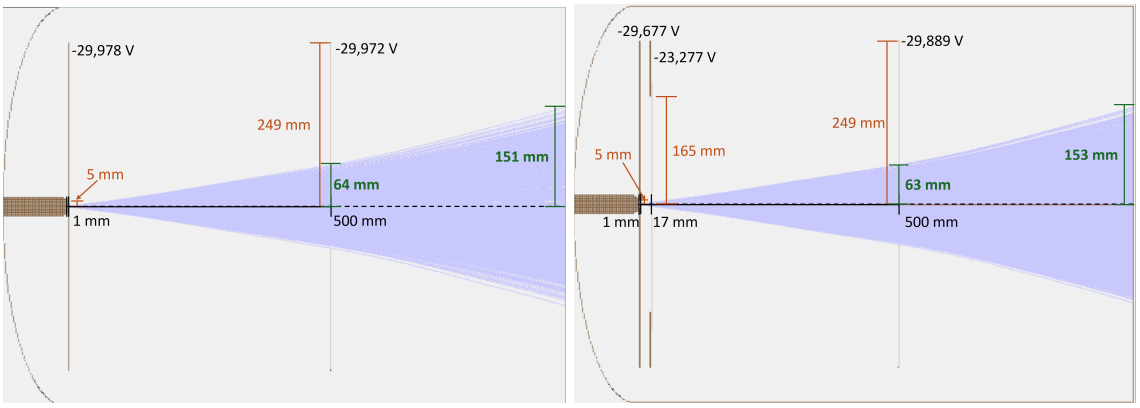

(a) Two thin lenses (b) Three thin lenses

Figure 5.6: Optimization results for two and three thin lenses. Lens radii values are shown in orange, lens potential and placement values in black, and beam radii values in green.

Following the evaluation done in Section 5.2.2, the half angle is set to 4.9°. In the process of performing the lens design optimization and modifying the weights of each component of the cost function, it is found that the lenses negligibly change the energy of the ion beam. Therefore, w_{v_x} is set to zero, as this component does not impact the results. Furthermore, determining the proper w_y and w_{v_y} weights to telescope the beam such that each component is evenly prioritized is found to be non-intuitive, and it is inefficient to readjust the weights because each optimization process takes approximately 16 hours. Instead, the cost function is set to solely maximize the final radius of the beam (w_y=1 and w_{v_y}=0), and adjustments are made post-optimization to minimize the final particle velocities in the y-direction.

5.3.1 Optimization Results

5.3.1.1 Thin Lens Results

The optimization results for two and three thin lenses are shown in Fig. 5.6. Interestingly, there is negligible difference between using two or three thin lenses. Both designs create a beam radius of 153 to 154 mm at the bottom of the chamber and a beam radius of 63 mm at 500 mm, the maximum lens x-value. In fact, the result for three thin lenses places the middle lens 1.6 cm from the first lens at a similar potential, and it is found that removing this lens does not change the beam properties. Therefore, both solutions functionally use two thin lenses to expand the beam. In both designs, the first lens is as close to the ion gun as possible with the smallest radius possible and is held at nearly the maximum potential. The second lens is then placed at the maximum distance from the ion gun, the lens radius is as large as possible, and the potential is again nearly the maximum possible value. This process appears to provide an initial increase in beam radius as the ions are exiting the ion gun and a final boost to the radius as far as possible from the beam's point of origin.

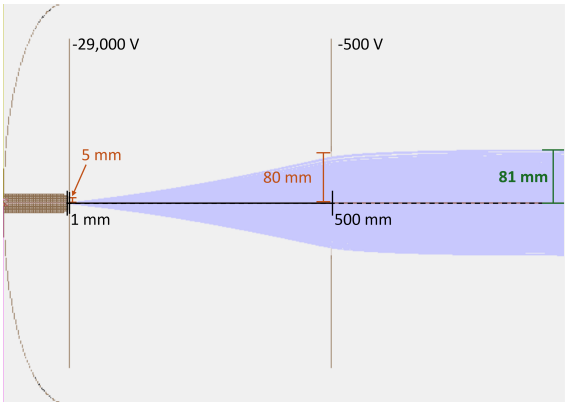

Figure 5.7: Telescoped beam with thin lenses. Lens radii values are shown in orange, lens potential and placement values in black, and beam radii values in green.

Because the cost function is designed to simply maximize the beam radius, the resulting beam is not telescoped. Therefore, the second lens is modified to telescope the beam. It is found that with an initial lens at -29,000 V, a second lens at 500 mm at -500 V with an 8 cm radius

telescopes the beam, as shown in Fig. 5.7. The final beam radius is then 81 mm, over twice as large as the unaltered beam radius found in Section 5.2.2. For this lens design, the lens closest to the ion gun expands the beam and is referred to as the *expanding lens*. The lens farthest from the ion gun refocuses the beam and is referred to as the *focusing lens*.

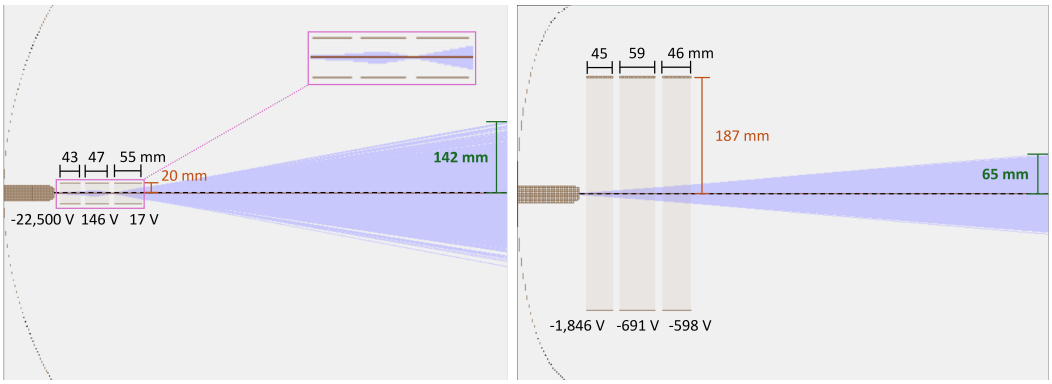

(a) Initial result (b) Restricted result

Figure 5.8: Optimization results for thick lens design. Initial results (top) utilize constraints shown in Table 5.1 and restricted (bottom) has the additional constraints $V_1 \leq 0$, $V_2 \leq 0.1V_1$, and $V_3 \leq 0.1V_1$.

5.3.1.2 Thick Lenses Results

The optimization results for the thick lens design is shown in Fig. 5.8. Initially, the thick lenses widen the beam by expanding it with a negative lens. Then, two positive lenses repel the beam to such an extent that the ions cross through a point and the polarity of the velocity in the y-direction v_y is flipped. This generates a beam with a final radius of 142 mm, approximately a centimeter smaller than the radius achieved by the thin lenses. The process of widening the beam is more complex than previously found, which may create issues when characterizing spacecraft wake formations. Therefore, the lens potentials are restricted such that the beam is widened without the ion paths crossing each other. To do so, the first lens must be negative ($V_1 \leq 0$), and the last two lenses are also negative with potential magnitudes greater than one-tenth the magnitude of the first lens potential ($V_2 \leq 0.1V_1$ and $V_3 \leq 0.1V_1$). The resulting lens design negligibly changes

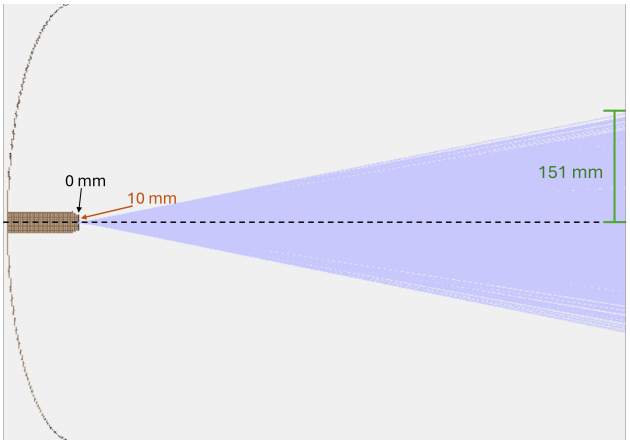

Figure 5.9: Ion beam expanded with magnetic field generated by a coil of wires. Coil radii is shown in orange, distance from ion gun exit in black and final beam radius in green.

the radius of the beam, indicating that the thick lens design is not viable for increasing the radius of the beam without the ion trajectories crossing. Because the thick lens design is not as effective at increasing the beam radius as the thin lens design, the thin lens design with an expanding and focusing lens is selected to alter the ion beam.

5.3.1.3 Magnetic Lens Comparison

It is mentioned in the introduction that the magnetic field can also be manipulated to expand and focus the ion beam, so the current required to generate a similar beam expansion to that shown in Section 5.3.1.1 is determined. For this project, a thick coil with current running through can be used to generate a magnetic field and expand the beam. SIMION is capable of modeling this configuration,[1] with the coil position, radius, wire thickness, current, and number of turns specified. Helmholtz coils have previously been implemented in the ECLIPS chamber with 0.75 mm radius wires, a maximum current of 5 A, 40 turns, and 298 mm radius [204]. To theoretically modify this configuration to expand the beam, a single coil could be taken, placed directly below the ion gun exit (similar to the expanding lens), and tightened such that the radius is 10 mm. If the number of turns is held at 40 mm, a current of 8,000 A is required to expand the beam to a radius of

[1] See SIMON `thick_coil` example available with the software.

≈150 mm at the base of the chamber, as shown in Fig. 5.9. This far exceeds the capabilities of current sources available in the AVS or similar laboratories and validates that electrostatic lenses are a more viable option for expanding the beam for ion wake experiments.

5.3.2 Arcing Analysis

A thin expanding lens placed as close as possible to the ion gun is optimal for increasing the radius of the beam. However, the high voltage lens may arc with the nearby, grounded ion gun. If arcing occurs, the HVPS will shut off and the ion gun may be damaged. To prevent this, the maximum voltage that can be achieved before arcing is characterized at several separation distances. This is accomplished using two conductive sheets of aluminum that are held at the desired separation distance. One sheet is grounded, and the voltage on the second sheet is increased until arcing occurs. The arcing potential is then recorded, the separation distance is increased, and the experiment is repeated. The wake experiment is conducted in vacuum, but the arcing voltage versus separation distance is recorded in atmosphere, which is approximately 630 Torr at room temperature in Boulder, Colorado. This is done because the objects may arc through the flowing argon, resulting in lower possible potentials at a set separation distance than expected in vacuum. The arcing voltage versus separation distance is plotted as a white line over the expected final beam radius versus lens distance from the ion gun and lens potential in Fig. 5.10. This line indicates where the lens may be expected to arc with the ion gun, and safe lens voltage and distance combinations are located below the white line. Fortunately, it is found that the beam radius plateaus after a certain lens potential, which means lower expanding lens potentials than found in Section 5.3.1.1 can be used to achieve the maximum beam radius. It is evident from the figure that the largest beam radius at the RPA is limited to 60 to 70 mm for a lens located 3 to 5 mm from the ion gun. Once the lens is placed 6 mm or more from the ion gun exit, the radius of the beam is negligibly increased.

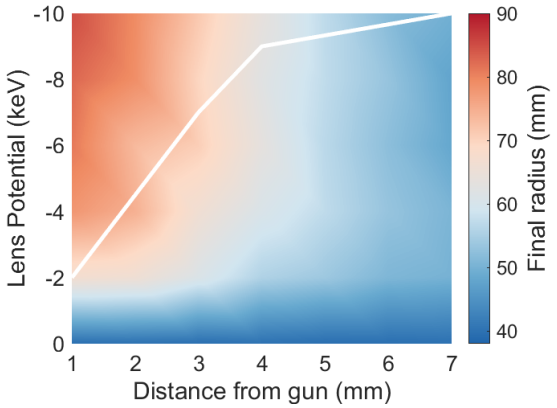

Figure 5.10: Expected beam radius at the RPA position (46 cm from ion gun exit) versus expanding lens potential and distance from ion gun. The white line indicates the voltage and distance combination at which arcing may occur.

5.4 Lens Characterization

The lenses are constructed from 6 mm thick sheets of aluminum and held at the desired potentials using Matsusada AU-30R1 HVPS. PEEK rods are used to electrically isolate the lenses from the chamber walls and hold them in place, as shown in Fig. 5.11. The lenses are sanded to avoid any irregularities on the surface or edges, and a level is used to ensure they are as flat as possible upon installation. As described in Section 5.3.1, the optimal lens design uses an expanding lens near the ion gun exit and a focusing lens farther away to telescope the beam. Before combining the entire setup, the expanding and focusing lenses are installed one at a time and measured to test their individual effects.

5.4.1 Expanding Lens

The expanding lens is positioned 5 mm from the ion gun exit with an inner radius of 5 mm. Creating a detailed map of the lens, as done in Section 5.2.2, takes approximately four hours. It is desirable to test the entire range of lens potentials in the same sitting, as this minimizes changes to the setup or ion beam properties. Therefore, a faster method of estimating the size of the beam must be determined. The general shape of the beam is assumed to be approximately circular.

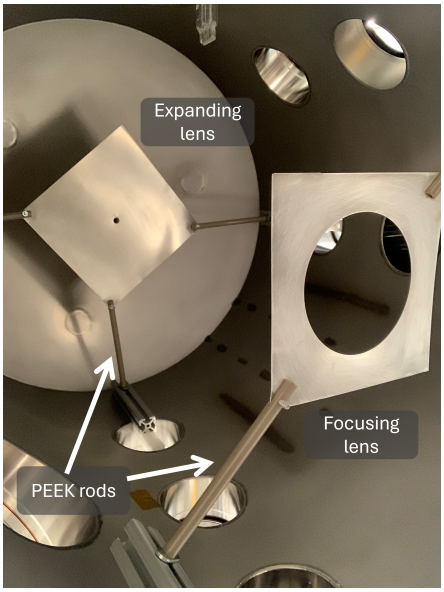

Figure 5.11: Lens setup in the ECLIPS vacuum chamber

Then, at least three edge points of the beam are found and the positions are recorded as Cartesian coordinates (x,y). These points are then used to find the center point of the beam (x_c,y_c) and radius r by performing a linear least squares (LLS) fitting to the equation of a circle

$$r^2 = (x - x_c)^2 + (y - y_c)^2. \tag{5.5}$$

To find these edge points, the sensors measure a straight line along the entire length of the stepper motor, then the rotational stepper motor is rotated 90°, and the process is repeated. This results in three to four edge points being recorded and utilized to determine the position and size of the circular projection of the beam. Examples of these circular projections of the beam are shown in Fig. 5.12. Based on the RPA measurements, it is also found that the final ion energy remains at approximately 835 eV. This validates the SIMION results, which indicated that the lenses are not expected to significantly change the ion energy.

As shown in these projections, the beam is expanded and **translated** as the potential is varied. This indicates that the lens is misaligned, meaning it is not perfectly flat or centered with respect to the ion gun. Misalignment is expected within the system, particularly because this lens design is intended to be installed by hand and adaptable to different vacuum chamber systems.

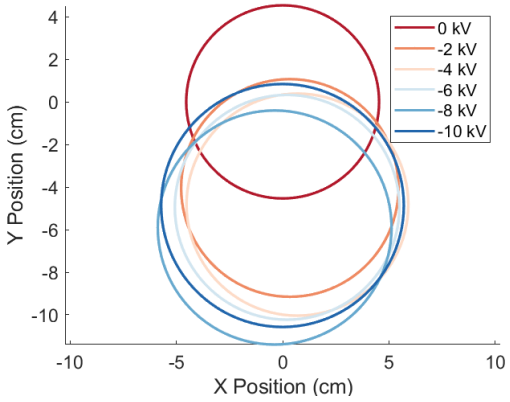

Figure 5.12: Projections of the ion beam made from RPA measurements for varying expanding lens potentials.

Therefore, the beam translations are characterized for various misalignment.

The expanding lens is modeled in SIMION at a distance of 5 mm from the ion gun to match the experimental setup. The simulated lens is then shifted from the center of the simulation and tilted to characterize how the misalignment may impact the ion beam radii and offset. The translation, or offset, of the beam and final radius values for various lens misalignments is shown in Fig. 5.13. The dashed lines display results for a perfectly centered, but tilted beam and the solid lines represent an off-center but perfectly level lens. Tilting the lens has a significantly smaller effect than shifting the lens with respect to the ion gun. Thus, any ion beam translations are contributed to an off-center lens.

The expanding lens was set up and characterized in two separate trials. The translation of the lenses is unknown, so the recorded results are compared to SIMION results to estimate how much the lenses might have been offset. The experimental and corresponding SIMION results for the two trials are shown in Fig. 5.14. The error bars indicate the 1σ value from the LLS fitting and an assumed measurement error of ± 2.5 mm. The beam translation is only shown at the RPA position because the translation between the RPA and LP positions changes by millimeters. Therefore, the SIMION results have significant overlap, and showing both results is redundant. The LP was improperly connected to the multi-meter during trial 1, so there are no LP results for that test.

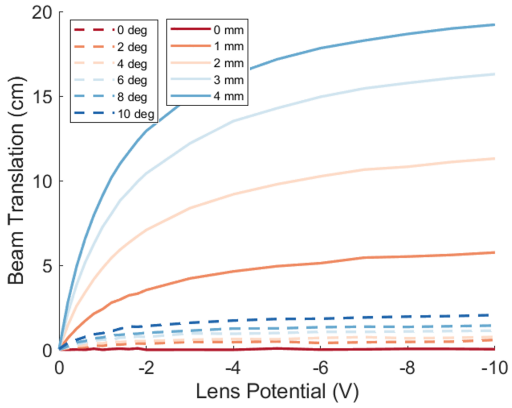

Figure 5.13: SIMION simulations of ion beam translation at the RPA position versus expanding lens potential for varying misalignments. Solid lines indicate an off-center lens and dashed indicate a tilted lens.

It is estimated that trial 1 was offset approximately 0.9 mm and trial 2 was offset 0.5 mm. The experimental and SIMION beam translation correspond well with each other. This validates that the translation of the beam can be contributed to the lens being off-center with respect to the ion gun by sub-millimeter magnitudes.

SIMION shows a quick jump in radius before a plateau, while the experimental results indicate a more gradual increase in radius and then plateau. This may be due to inaccuracies in the chamber model in SIMION, as some unmodeled components such as the chamber windows or wires may slightly alter the potentials. However, it is shown that the radius of the beam is increasing with lens potential, the majority of the SIMION results are within the error bounds of the experimental results, and the maximum radius for both appears to be approximately the same. Thus, the expanding lens is performing as designed and generating a wider beam as predicted.

5.4.2 Focusing Lens

In order for the focusing lens to "compress" the ions into a smaller radius beam, the lens must be more positive than the preceding lens or ion source [122]. In initial experiments using the focusing lens, the lens is placed 36 cm down from the ion gun exit and has an opening of 50 mm. The LP is then located 1.6 cm from the lens, and the RPA entrance is 11.6 cm from the lens.

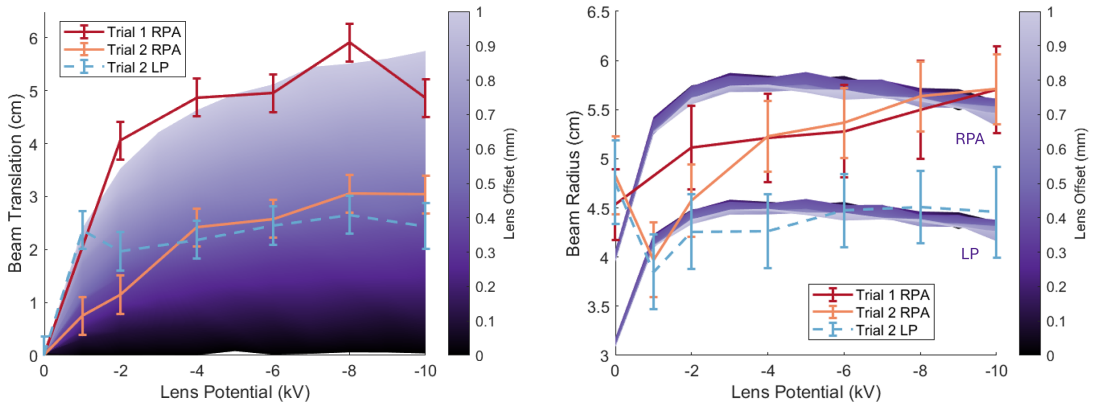

(a) Translation (b) Radius

Figure 5.14: Ion beam translation (top) and radius (bottom) versus expanding lens potential. SIMION results are shown in a purple gradient. Trial 1 is estimated to be shifted 0.9 mm and Trial 2 is estimated to be shifted 0.5 mm.

Experiments revealed that the proximity of the Langmuir Probe to the focusing lens significantly alters the electric field and resulting measurements. This phenomenon was recreated in SIMION, and comparisons between current density measurements modeled in SIMION and measured in experiments show good agreement. This is described in further detail in Reference [38]. However, phenomena such as beam deflection may be missed if the current density is solely used to evaluate the beam behavior. Therefore, the experiments are modified and repeated. The Langmuir probe is shifted down so it is only 58 mm above the RPA entrance compared to 101 mm. The focusing lens is widened to a 70 mm radius and moved to 31 cm below the ion gun exit. This creates a separation distance of 10.5 cm between the lens and Langmuir probe.

The beam translation is characterized for this lens configuration, as shown in Fig. 5.15. Once again, an off-center lens translates the beam more than a tilted lens. Since the lens is farther from the ion source, lens translations on the order of centimeters are required to generate beam translations comparable to those seen in Section 5.4.1. This is useful because the focusing lens is farther from the ion gun, and the vacuum chamber walls prevent the focusing lens and ion gun from being seen at the same time. As a result, the focusing lens is aligned to the bottom of the vacuum chamber using a vertical laser level. The floor of the vacuum chamber is not connected to the top

of the vacuum chamber, and shifts in the vacuum chamber floor cause additional misalignment between the ion gun and focusing lens.

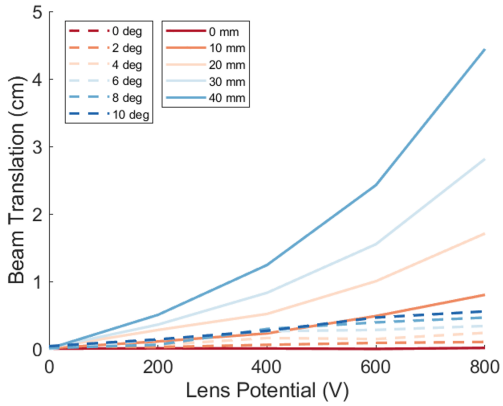

Figure 5.15: SIMION simulations of ion beam translation at the RPA position versus lens potential for varying focusing lens misalignments. Solid lines indicate an off-center lens and dashed indicate a tilted lens.

The beam radius and offset versus lens potential is shown in Fig. 5.16, and the SIMION results are shown in the background as a purple gradient. As with the expanding lens, the error bars indicate the σ value from the LLS fitting and an assumed measurement error of ± 2.5 mm. The ion energy is also again measured at approximately 835 eV by the RPA. The SIMION results are shown at the RPA location. The beam radius decreases as the lens potential increases, as expected, and the beam is translated 4.25 cm for an 800 V lens. Based on this, it is estimated that the beam is off-center by approximately 3.4 cm. SIMION simulations indicate that if the beam is more off-center than this, at approximately 800 V the lens significantly repels the nearby beam and begins to expand the beam radius. The experimental results indicate the beam is translated approximately 1 cm more than indicated by the SIMION simulations for a lens offset of 3.4 cm. However, the beam radius decreases as expected, so it is unlikely the lens is more off-center. It is possible that the wires providing power to the focusing lens and stepper motors alter the electric field and generate more beam translation than predicted. The beam radius versus lens potential results show good agreement with the SIMION simulations, and the SIMION results are within the 1σ error bars of the experimental results. This, in addition to the focusing lens results presented

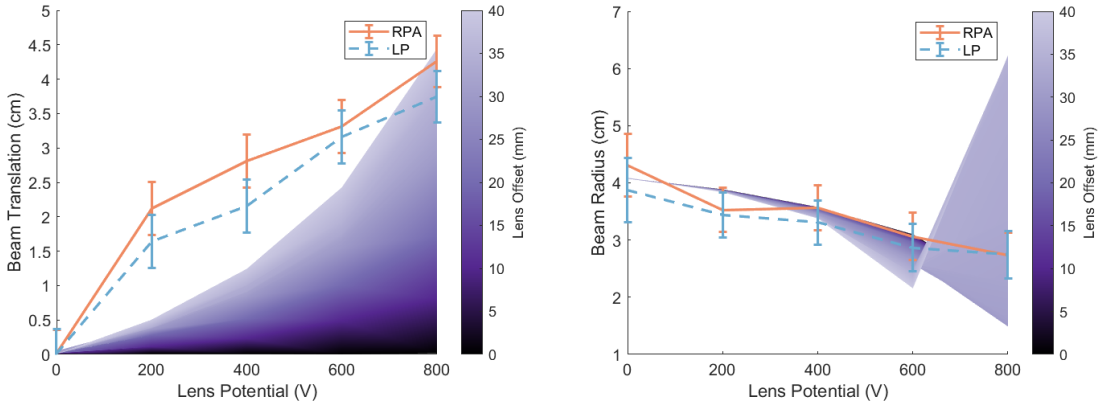

(a) Translation (b) Radius

Figure 5.16: Ion beam translation (top) and radius (bottom) versus focusing lens potential. SIMION simulation results are shown in a purple gradient, and it is estimated the lens is offset ≈34 mm.

in Reference [38] validate that the beam is focused as predicted.

5.4.3 Both Lenses

Finally, both lenses are installed. The expanding lens is kept 5 mm from the ion gun exit with a radius of 5 mm, and the focusing lens is kept 36 cm from the ion gun exit with a radius of 7 cm. This should leave 3 cm of space between the ion beam edge and focusing lens opening. The lens should be telescoped, similar to the beam shown in Fig. 5.7, with a final radius of 45 mm when the expanding lens is held at -8 kV and focusing lens is held at -500 V. The current density map measured by the Langmuir probe is shown in Fig. 5.17(b). Here, it appears the beam impacts the edge of the focusing lens, as shown by the curvature on the left side of the plot. It is difficult to determine if one or both lens misalignments causes this, but upon investigating with SIMION, it is found that in this configuration if the expanding lens is off-center by 1 mm, the beam will impact the focusing lens, as shown in Fig. 5.17(a). The focusing lens is also likely off-center, likely increasing the percentage of the ion beam that is impacting the lens.

A larger focusing lens could be utilized to avoid the beam impacting the lens. However, the lenses are not installed with sub-millimeter precision and misalignment will still be expected. A

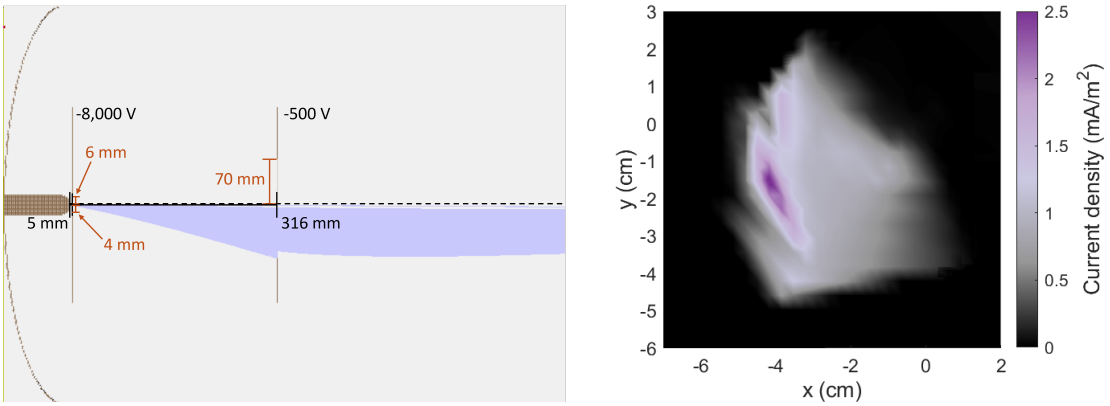

(a) SIMION (b) Experiment

Figure 5.17: Current density map measured by the Langmuir Probe with the expanding and focusing lens in place (bottom), and a SIMION simulation of a possible corresponding lens setup (top).

SIMION simulation with a larger focusing lens and realistic lens placements, or the expanding lens off-center by 0.5 mm and focusing lens off-center by 1 cm, is shown in Fig. 5.18. The larger focusing lens does allow the beam to pass through without impact. However, the combined misalignments of the lenses causes the beam to have a non-zero velocity parallel to the floor of the chamber. In other words, the focusing lens does not cause the ions to flow parallel to the chamber walls, which is the desired configuration for this test design. This could be useful if it is desirable to simulate a spacecraft with a velocity comparable to the plasma bulk velocity ($v_{sc} \approx v_{\text{bulk}}$) traveling in a direction that is not parallel to the bulk velocity, such as the conditions experienced by the Parker Solar Probe [57]. For this project, the aim is to represent solar wind flow around cislunar spacecraft, and the spacecraft velocity is not comparable to the bulk velocity, so ion flow should be symmetrical around the spacecraft to best represents the ion wake around a cislunar spacecraft.

5.4.4 Wake Generation

The goal of this project is to generate a wake that can be used in future experiments. To accomplish this, as previously mentioned, the beam must be large enough to fully envelop a representative spacecraft and be measured, and ideally the ions would flow parallel to the chamber walls.

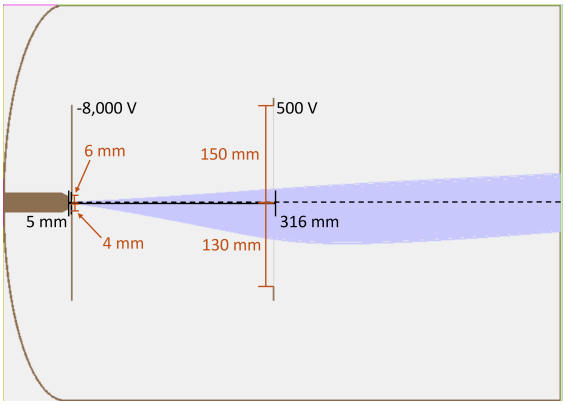

Figure 5.18: SIMION simulation of both lenses installed with expanding lens off-center by 1 mm and focusing lens off-center by 1 cm.

Since the focusing lens introduces additional deflections and does not generate ion velocities that represent cislunar plasma flow, only the expanding lens is used to generate representative spacecraft wakes. This also generates a larger beam around the representative spacecraft, making the wake formation simpler to characterize. The expanding lens is again held 5 mm from the ion gun exit, has an inner radius of 5 mm, and is held at a potential of -8 kV. Therefore, the beam radius at the representative spacecraft location should be approximately 5.5 cm, which is large enough to fully envelope a representative spacecraft. A cube with a width of 5 cm is used to represent a spacecraft. Assuming a beam current of 10μA, representative solar wind plasma density of 6E6 m^{-3}, and using Equations (5.1) and (5.2), the 5 cm cube represents a spacecraft with a width of 6.6 m.

As described in Section 5.4.1, if the expanding lens is off-center by sub-millimeter distances, the beam is deflected by several centimeters. Therefore, the expanding lens is first installed and the position of the beam is determined without the cube in place. Then, the vacuum chamber is opened, the cube is placed in the path of the beam, and the experiment is repeated with the cube in the beam path. The RPA cannot fit underneath the cube in the vacuum chamber, so only the Langmuir probe is used to determined the ion beam behavior. The expected ion beam behavior and experimental results are shown in Fig. 5.19. It is expected that a -110 V cube creates an expanding wake that is larger than the width of the cube. This is found experimentally, as the width of the beam is larger with the -110 V cube in place versus without. When the cube potential is increased

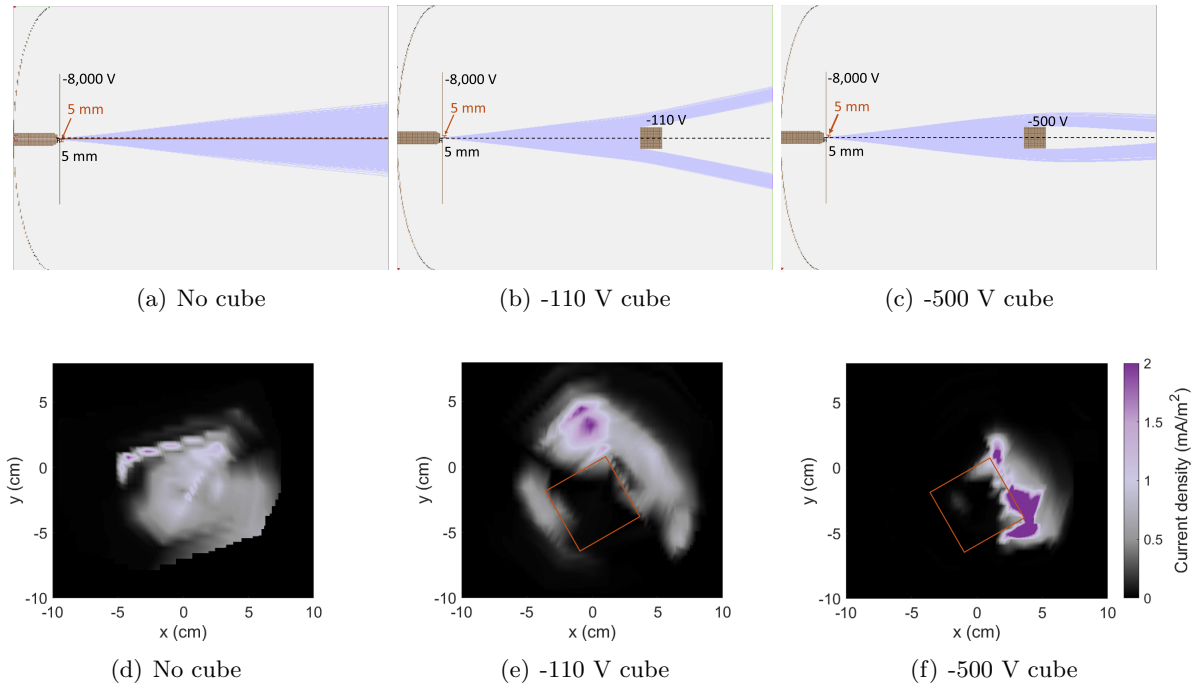

(a) No cube (b) -110 V cube (c) -500 V cube

(d) No cube (e) -110 V cube (f) -500 V cube

Figure 5.19: SIMION simulation of chamber wake generation (top) and current density maps of experimentally generated wakes (bottom). A projection of the cube is shown in orange.

to -500 V, the ions are attracted toward the cube, and a closing wake is generated. This is again found in experiments, as the width of the beam is smallest for this configuration. The ions seem to disappear on the left side of the cube when the voltage is decreased from -110 V to -500 V. This likely occurs because the ion beam is thinner on this side, and the ions are attracted into the side of the cube when the voltage magnitude is increased. Overall, it is shown that the expanding lens can be used to reliably expand and translate the beam, and the wake behavior matches in simulations and experiments.

5.5 Conclusions

Electrostatic lenses are investigated and tested in the ECLIPS vacuum chamber system to manipulate the ion beam behavior. It is shown that in an ideal system, two lenses are optimal for this system for increasing the radius of the beam and telescoping the beam. When telescoping the beam, the top lens is referred to as the expanding lens and the bottom is referred to as the focusing

lens. If the expanding lens is off-center by sub-millimeter distances, the ion beam is deflected several centimeters. For the focusing lens, offsets on the order of centimeters deflect the beam several centimeters. Regardless, individually, both the expanding lens and focusing lens alter the ion beam radius as expected, presenting a novel, adaptable method to manipulate a charged beam.

Spacecraft ion wakes are generated with only the expanding lens in place. It is shown that wake formations around a cube with varying potential can be generated and measured, and the measured results show good agreement with simulations. Thus, simple electrostatic lenses are successfully designed, tested, and used to generate spacecraft ion wakes. This lens configuration could be implemented in any scenario in which it is necessary to widen, focus, or translate a beam with charged particles beyond the capabilities of its pre-existing configuration.

Chapter 6

Proximity Charging Interactions

6.1 Motivation

As shown in Chapters 3 and 4, the presence of a charged servicer near a floating target can change the target's emissions and surface potential. Typically, electrostatic actuation or coulomb formation flying studies prescribe surface potentials or utilize charging equations to determine the potentials, which does not capture the phenomena seen in previous chapters. The changing target potentials and emissions were captured through simulations in Nascap-2k and SPIS, which are powerful but computational expensive tools that can take hours to days to run. Therefore, results from SPIS are utilized to generate analytic approximations of the interactions between spacecraft, increasing the efficiency and ease of future electrostatic actuation investigations.

The legacy charging equations are first presented, followed by the electrostatic force equation. Then, charging behaviors that occur when a highly charged object is nearby are investigated, including electron emissions being drawn away from a positively charged spacecraft, repulsion of like charges in a plasma, and acceleration of ambient particles. Next, the servicer recollecting electron emissions generated by electron beam impact on the target is characterized. The ion current to a target within the wake of a servicer is then characterized and analyzed with simple simulations and experiments. Finally, the resulting charges and forces in cislunar environments are presented with the inclusion of the newfound proximity charging approximations.

6.2 Charging and Forces Equations

In this study, all surface are assumed to be aluminum. The current charging equations implemented for electrostatic tractor investigations assume orbit motion limited (OML) currents, which are applicable when the Debye length is larger than the spacecraft. In this regime, the potential of a servicer equipped with an electron gun is first determined using the current balance equation

$$I_e(V_S)[1-\alpha(V_S)] - I_{ph}(V_S) - I_i(V_S)[1-\delta_i(V_S)] - I_B(V_S) = 0, \tag{6.1}$$

where I_e is the incident electron current, I_i is the incident ion current, α is the sum of the SE yield δ and backscattered electron yield η, and δ_i is the SE due to incident ions yield.

The incident electron current is [110]

$$I_e(V) = \frac{1}{4} q_e n_e v_e A \exp\left(\frac{q_e V}{k_B T_e}\right) \quad \text{for } V < 0, \tag{6.2a}$$

$$I_e(V) = \frac{1}{4} q_e n_e v_e A \left(1 + \frac{q_e V}{k_B T_e}\right) \quad \text{for } V > 0, \tag{6.2b}$$

where A is the total surface area of the spacecraft and v_e is the velocity of the electrons $\sqrt{2q_eT_e/m_e}$. The incident ion current in a non-mesothermal plasma is similarly

$$I_i(V) = \frac{1}{4} q_e n_i v_i A \left(1 - \frac{q_e V}{k_B T_i}\right) \quad \text{for } V < 0, \tag{6.3a}$$

$$I_i(V) = \frac{1}{4} q_e n_i v_i A \exp\left(\frac{-q_e V}{k_B T_i}\right) \quad \text{for } V > 0. \tag{6.3b}$$

When the plasma is mesothermal, the ion current is computed using the shifted orbit motion limited (SOML) equations

$$I_i(V) = q_e A_{\text{ram}} n_i v_{\text{bulk}} \left(1 - \frac{2q_e V}{m_i v_{\text{bulk}}^2}\right) \quad \text{for } V < 0, \tag{6.4a}$$

$$I_i(V) = q_e A_{\text{ram}} n_i v_{\text{bulk}} \exp\left(\frac{-2q_e V}{m_i v_{\text{bulk}}^2}\right) \quad \text{for } V > 0. \tag{6.4b}$$

Essentially, the energy of the bulk velocity of the plasma is used to scale the current instead of the thermal energy of the ions, and the ions are assumed to impact the projected area of the ram side

of the spacecraft. These equations are applicable because the potentially field is negligibly altered by the wake when the spacecraft is smaller than the Debye length, as shown in Chapter 4.

The photoelectron current I_{ph} is

$$I_{ph}(V) = J_{ph}A_{ph}\exp\left(\frac{-V}{k_B T_{ph}}\right) \quad \text{for V} > 0, \tag{6.5a}$$

$$I_{ph}(V) = J_{ph}A_{ph} \quad \text{for V} \leq 0, \tag{6.5b}$$

where J_{ph} is the photoelectron current density and A_{ph} is the sunlit area of the spacecraft. For a spherical spacecraft, the sunlit area is πR^2, where R is the spacecraft radius. The photoelectron current density is defined as 4E-5 A/m^2 in this work.

The SE yield δ depends on the incidence energy of the primary particle and angle of incidence. For this approximation, the incidence angle of the electrons is assumed to be zero, or perpendicular to the surface of the spacecraft. The yield is implemented based on the Nascap-2k definition [47]

$$\delta(E) = c_1 \int_0^R \left|\frac{\mathrm{d}E}{\mathrm{d}x}\right| \exp -c_2 x dx, \tag{6.6}$$

where

$$\frac{\mathrm{d}E}{\mathrm{d}x} = \left(\frac{\mathrm{d}R}{\mathrm{d}E_0}\right)^{-1} + \left(\frac{\mathrm{d}^2R}{\mathrm{d}E_0^2}\right)\left(\frac{\mathrm{d}R}{\mathrm{d}E_0}\right)^{-3} x, \tag{6.7}$$

and R is a bi-exponential range law with a four parameter fit

$$R = b_1 E_0^{e_1} + b_2 E_0^{e_2}. \tag{6.8}$$

For aluminum, the fitting parameters b_1, b_2, e_1, and e_2 are 154 Å/eV, 220 Å/eV, 0.8, and 1.76, respectively.

The backscattered electron yield η is again based on the Nascap-2k yield

$$\eta(E) = \left(\frac{H(1-E)H(E-0.05)\log(E/0.05)}{\log 20} + H(E-1)\right) \left(1 + \frac{\mathrm{e}^{-E/5}}{10} - \left(\frac{2}{\mathrm{e}}\right)^{0.037Z}\right), \tag{6.9}$$

where Z is the atomic number, E is the energy in keV, and $H(E)$ is the Heaviside step function. The atomic number of aluminum is 13 [121].

The SE yield due to incoming ions is based on the Nascap-2k implementation [47]

$$\delta_i(E) = \frac{\beta E^{1/2}}{1 + E/E_{\text{max,i}}} \quad \text{for } V < 0, \tag{6.10a}$$

$$\delta_i(E) = \frac{\beta(E) E^{1/2}}{1 + E/E_{\text{max,i}}} \exp\left(\frac{-V}{k_B T_{se}}\right) \quad \text{for } V > 0, \tag{6.10b}$$

where $E_{\text{max,i}}$ is the ion energy at which the maximum yield occurs and $\beta(E)$ is a scaling parameter

$$\beta(E) = \begin{cases} 0.25 \quad \text{for } E < 0.476 \text{ keV} \\ 2^{-1/E-0.1} \quad \text{for } 0.476 \text{ keV} < E \leq 10 \text{ keV} \\ 1 \quad \text{for } 10 \text{ keV} < E \end{cases} \tag{6.11}$$

$E_{\text{max,i}}$ is assumed to be 230 keV, based on the values for aluminum implemented in Nascap-2k. The yield models and material properties for aluminum are the same in Nascap-2k and SPIS.

SE emissions escape from the surface with energies on the order of a few volts, while backscattered electrons are emitted with their approximate impact energy. Therefore, if the spacecraft is more than a few volts positive, the SE emissions will be attracted back towards the servicer. In order to find α in a Maxwellian plasma, the yield is integrated over the distribution function of the ambient electrons

$$\alpha = \int_0^\infty [\eta(E) + \delta(E)] f_E(E) \mathrm{d}E \quad \text{for } V < 0, \tag{6.12a}$$

$$\alpha = \int_0^\infty \left[\eta(E) + \delta(E) \exp\left(\frac{-V}{k_B T_{se}}\right)\right] f_E(E) \mathrm{d}E \quad \text{for } V > 0, \tag{6.12b}$$

where T_{se} is the emission energy of SEs (assumed to be 2 eV), and $f_E(E)$ is the Maxwellian energy distribution function

$$f_E(E) = \frac{2E^{1/2}}{\pi^{1/2}(k_B T_e)^{3/2}} \exp\left(\frac{-E}{k_B T_e}\right). \tag{6.13}$$

Similarly, the secondary electron from ion yield is

$$\delta_i = \int_0^\infty \delta_i(E) f_E(E) \mathrm{d}E \quad \text{for } V < 0, \tag{6.14a}$$

$$\delta_i = \int_0^\infty \delta_i(E) \exp\left(\frac{-V}{k_B T_{se}}\right) f_E(E) \mathrm{d}E \quad \text{for } V > 0, \tag{6.14b}$$

where T_{se} is again assumed to be 2 eV.

The current balance equation of a target impacted by an electron beam, assuming the entirety of the beam impacts the target, is

$$I_e(V_T)[1-\alpha(V_T)] + I_{ph}(V_T) - I_i(V_T)[1-\delta_i(V_T)] + I_B(V_T,V_S)[1-\alpha_B(V_T,V_S)] = 0, \tag{6.15}$$

where α_B is the sum of the SE and backscattered electron emissions due to the beam. The landing energy of the electron beam is

$$E_{\text{land}} = E_B + q_e V_t - q_e V_s \quad \text{for } q_e V_s - q_e V_t < E_B, \tag{6.16a}$$

$$E_{\text{land}} = 0 \quad \text{for } q_e V_s - q_e V_t \geq E_B. \tag{6.16b}$$

If the difference in potentials between the servicer and the target is greater than the energy of the electron beam ($q_e V_s - q_e V_t \geq E_B$), the beam will be deflected by both objects and will not impact the target. The landing energy of the electron beam then serves as the impact energy when calculating α_B using Eqns. (6.2) and (6.2).

The electrostatic force between two charges in a vacuum is found with Coulomb's law

$$F_e = k_c \frac{q_1 q_2}{r^2}, \tag{6.17}$$

where k_c is Coulomb's constant (≈8.99E6 Nm^2/C^2), r is the center-to-center separation distance of the spheres, and $q_{1,2}$ are the charges. The charge of a single sphere is a function of the potential and capacitance C

$$q = CV. \tag{6.18}$$

When two charged spheres are in the vicinity of each other, mutual capacitance effects occur, which must be accounted for. The approximation for the charge on two spheres is

$$\begin{bmatrix} q_1 \\ q_2 \end{bmatrix} = \frac{r}{k_c(r^2 - R_1 R_2)} \begin{bmatrix} R_1 r & -R_1 R_2 \\ -R_1 R_2 & R_2 r \end{bmatrix} \begin{bmatrix} V_1 \\ V_2 \end{bmatrix}. \tag{6.19}$$

As was discussed in Chapter 3, Debye lengths shorter than the separation distance can exist in the solar wind and magnetosheath cislunar environments, but the effective Debye length can extend

the sphere's influence significantly farther than the separation distances proposed. Therefore, this approximation for the force is appropriate when there are large potentials on the spacecraft, as is expected during electrostatic tractor operations.

6.3 Sheath Overlap

6.3.1 Electron Emission Collection

When a highly positive spacecraft, such as one equipped with an electron gun, is located near another floating spacecraft, it is possible for the electron emissions from the floating spacecraft to be drawn away into the highly positive spacecraft. This phenomena, referred to as sheath engulfment, has been observed on the SCATHA satellite. SCATHA was equipped with an electron beam and had booms that were electrically isolated from the main body. As SCATHA rotated, oscillations in the main body potential were recorded that corresponded to the frequency of the rotations. Analysis indicated that as the main body charged highly positive due to electron beam emissions, photoelectrons were drawn away from the boom when they became sunlit and collected by the main body. This then decreased the main body's potential, leading to the observed surface potential oscillations [109–111].

A simple model was proposed to estimate the photoelectron current collected by the main body of the SCATHA satellite. In essence, the potential at a position on the boom is estimated, and the fraction of the emissions below the energy of the potential at that point are assumed to be collected by the main body instead of recollected by the boom. In this study, the charging of the body that electron emissions are pulled away from are also considered. Typically, once spacecraft charge to a few volts positive, the low energy secondary electron and photoelectron emissions are recollected, and the spacecraft potential ceases to charge more positive. If these emissions are drawn away, the spacecraft could continue to charge positively.

The fraction of emissions that are drawn away from the target $\rho[\phi(r)]$ are estimated using

[110]

$$\rho[\phi(r)] = \frac{\int_0^{\phi(r)-V} E\exp(-E/k_BT_{se/ph})\mathrm{d}E}{\int_0^{\infty} E\exp(-E/k_BT_{se/ph})\mathrm{d}E}. \tag{6.20}$$

The updated electron emissions yields from the target are then

$$\alpha = \int_0^{\infty} (\eta(E) + \delta(E)) f_E(E)\mathrm{d}E \quad \text{for } V < 0, \tag{6.21a}$$

$$\alpha = \int_0^{\infty} (\eta(E) + \delta(E)\rho[\phi(r)])\, f_E(E)\mathrm{d}E \quad \text{for } \phi(r) \geq V \geq 0, \tag{6.21b}$$

$$\alpha = \int_0^{\infty} \left[\eta(E) + \delta(E)\exp\left(\frac{-V}{k_BT_{se}}\right)\right] f_E(E)\mathrm{d}E \quad \text{for } V \geq \phi(r) \geq 0, \tag{6.21c}$$

and the photoelectron current is

$$I_{ph}(V) = J_{ph}A_{ph} \quad \text{for } V < 0, \tag{6.22a}$$

$$I_{ph}(V) = J_{ph}A_{ph}\rho[\phi(r)] \quad \text{for } \phi(\mathrm{r}) \geq \mathrm{V} \geq 0, \tag{6.22b}$$

$$I_{ph}(V) = J_{ph}A_{ph}\exp\left(\frac{-V}{k_BT_{ph}}\right) \quad \text{for V} \geq \phi(r) \geq 0. \tag{6.22c}$$

The potential is modeled using the Debye-Hückel approximation in Eqn. 3.4 with the scaling parameters found in SPIS. It is assumed that the secondary electron and photoelectron currents drawn away from the target are collected by the servicer, so the updated charging equations are

$$I_e(V_T)[1-\alpha(V_T,V_S)] - I_{ph}(V_T,V_S) - I_i(V_T)[1-\delta_i(V_T,V_S)] + I_B(V_T,V_S)[1-\alpha_B(V_T,V_S)] = 0, \tag{6.23}$$

for the target and

$$\begin{aligned} I_e(V_S)[1-\alpha(V_S)] - I_{ph}(V_S) - I_i(V_S)[1-\delta_i(V_S)] - I_B(V_S) + I_{ph,T}(V_S,V_T)... \\ +I_{e,T}(V_T)\delta_T(V_S,V_T) + I_{i,T}(V_T)\delta_{i,T}(V_T,V_S) = 0, \end{aligned} \tag{6.24}$$

for the servicer, where the subscript T represents the current from the target. Because the spacecraft potentials depend on each other, the solution must be iterated until both spacecraft potentials stabilize to some solution. In this study, the surface potential solution is iterated until the servicer and target potential each change by less than 1%.

To validate the electron emission collection approximation, the SPIS results from Section 3.4.2.2 are utilized. In these simulations, a floating target spacecraft is simulated at varying separation

distances from a 1 kV and 10 kV servicer. Both spacecraft are 1 m aluminum spheres, and the target has a 4E-5 A/m^2 photoelectron current density. The spacecraft wake formations are not included.

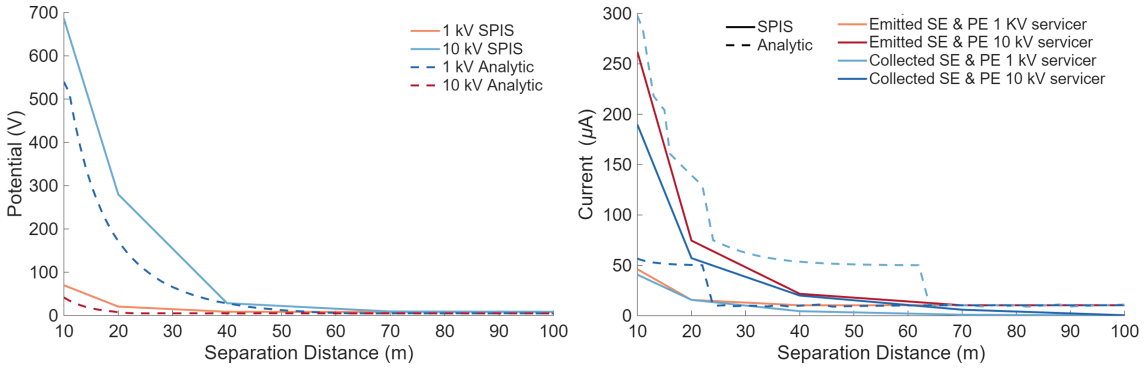

(a) Potentials (b) Currents

Figure 6.1: Floating spacecraft potentials (left) and emitted and collected currents (right) in a sunlit environment.

Figure 6.1 shows the floating spacecraft potentials and emitted and collected secondary electron and photoelectron current for varying separation distances. The emitted and collected current is slightly overestimated in the analytic solution, but in both solutions the fraction of current collected by the servicer is larger when the separation distance is smaller and drops once the target's potential exceeds the potential generated by the servicer ($\phi(r) < V_T$). All emitted current is assumed to be collected by the servicer when $\phi(r) > V_T$, so these lines overlap in Fig. 6.1(b). This assumption is validated in SPIS, as 80% to 95% of the electron emissions are recollected when the servicer is drawing emissions away from the target. The target's potential in SPIS is slightly higher than the calculated potential, which indicates that the potential about the servicer might be slightly underestimated in the analytic solution. Despite this, the floating potential solutions show good correlation, validating that the electron collection assumption is appropriate.

These results are only applied to positively charged targets. Bengtson et al. showed that once a target becomes a few kiloVolts negative, the electron emission current collected by the servicer remains below 10% regardless of servicer potential [17]. In addition, in Fig. 3.8(b) it is shown that

less than 10% of electron emissions from the negative target are collected by the servicer. Therefore, if the target is negatively charged it is assumed the the electron emission current collected by the servicer is negligible.

6.3.2 Repulsion of Charges

In addition to a positive servicer drawing electron emissions away from a floating target, a highly charged spacecraft can influence the ambient plasma population, changing the charging behavior of a nearby electrically disconnected object. This has been observed on the SPEAR-1 mission, where two 10 cm radius spheres were attached to a rocket body on the end of a 3 m boom. The spheres could be biased up to 46 kV, which incidentally caused highly negative potentials on the rocket body [102]. The sheath generated by the larger rocket body is theorized to partially or entirely engulf the small sheath generated by the positive sphere, reducing the electron current to the sphere despite its large positive potential. This concept can also be demonstrated in SPIS, as shown in Fig. 6.2, where a highly charged spacecraft repels like charges, reducing the relevant current to a nearby uncharged object.

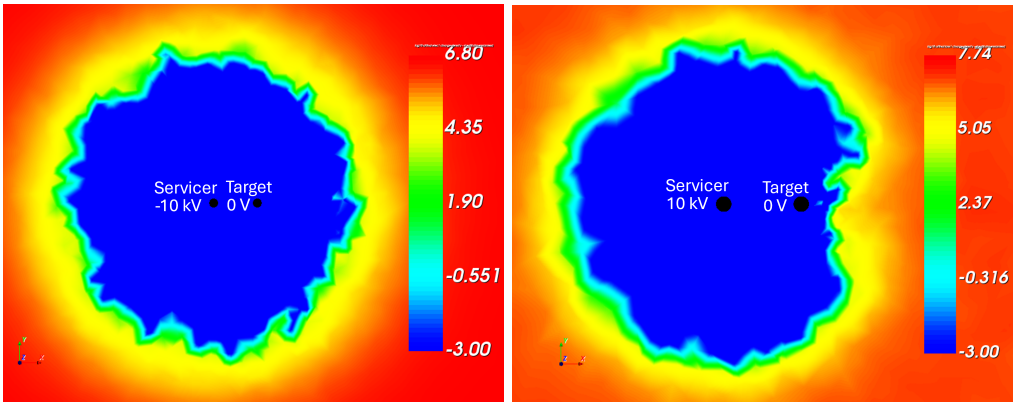

(a) $\log_{10}$ of electron density (b) $\log_{10}$ of ion density

Figure 6.2: Repulsion of electrons around a negative charged spacecraft (left) and ions around positively charged spacecraft (right).

If a nearby object is charged highly negative ($|q_e V| \gg T_e$), the electron current to the body

of interest is reduced and determined using

$$I_e(V,\phi(r)) = \frac{1}{4}q_e n_e v_e A \exp\left(\frac{q_e(V+\phi(r))}{k_B T_e}\right) \quad \text{for } V+\phi(r) < 0 \text{ and } \phi(r) < 0, \tag{6.25a}$$

$$I_e(V,\phi(r)) = \frac{1}{4}q_e n_e v_e A \left(1+\frac{q_e(V+\phi(r))}{k_B T_e}\right) \quad \text{for } V+\phi(r) > 0 \text{ and } \phi(r) < 0. \tag{6.25b}$$

where $\phi(r)$ is the potential generated by the positive spacecraft (Eq. (3.4)) at distance r. Similarly, if a nearby object is charged highly positive ($q_e V \gg T_i$), the ion density in the region may be depleted, and the ion current is determined as

$$I_i(V,\phi(r)) = \frac{1}{4}q_e n_i v_i A \left(1-\frac{q_e(V+\phi(r))}{k_B T_i}\right) \quad \text{for } V+\phi(r) < 0 \text{ and } \phi(r) > 0, \tag{6.26a}$$

$$I_i(V,\phi(r)) = \frac{1}{4}q_e n_i v_i A \exp\left(\frac{-q_e(V+\phi(r))}{k_B T_i}\right) \quad \text{for } V+\phi(r) > 0 \text{ and } \phi(r) > 0, \tag{6.26b}$$

These equations are only applied to ion currents in non-mesothermal plasma environments. If the conditions are not satisfied for these current equations to be implemented, the ion and electron currents are computed using Eqns. (6.2) and (6.2), respectively.

This assumption can be validated using the results presented in Section 3.4.2.3. In this investigation, a floating target is held at several distances from a 1 kV and 10 kV servicer in an eclipsed solar wind environment. As shown in Fig. 6.3, the analytic and SPIS solutions show good correlation. The analytic target potential is more negative than the SPIS potential at 10 m separation, which may be due to differences in the electron emission computations. In both solutions, the target's potential changes at a similar rate and settles to approximately -20 V once the target is outside the sphere of influence of the servicer. Therefore, the provided approximation for repulsion of like charges is appropriate.

6.3.3 Acceleration of Ambient Particles

It is theorized in Chapters 3 and 4 that a highly positive servicer may accelerate the ambient electrons, which may then impact the target at a higher energy and increase the secondary electron yield. To test this, a target is held at 0 V and the separation distance is varied near a 10 kV servicer. The target's electron emission current is then divided by the collected electron current found in SPIS

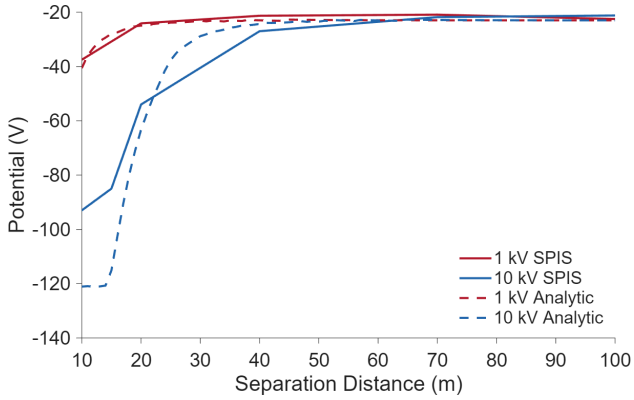

Figure 6.3: Floating spacecraft potentials for a spacecraft with varying separation distance from a 1 kV and 10 kV spacecraft.

to determine the yield. Figure 6.4 shows that the yield negligibly varies as the separation distance increases outside of noise. Therefore, it is unlikely that the highly positive servicer generates noticeable changes in the electron emission yield. Instead, the variation in emission currents seen in previous chapters is a result of the spacecraft surface potentials changing due to the repulsion of like charges. The different target potentials then repels or attracts electrons and changes their landing energy. Thus, only the energy of the one's own spacecraft need to be taken into account when determining the yield, and these equations remain unchanged from Section 6.2.

6.4 Beam Electron Emission Recollection

When the target is impacted by the electron beam, secondary and backscattered electrons are generated. This is accounted for when determining the target's potential using the α_B term. These emissions can be collected by the servicer, which is not included in the charging equations presented in Section 6.2. This may result in significantly more negative servicer potentials than expected, changing the efficiency of electrostatic actuation operations. Fortunately, the electron emissions from the target can be included in the servicer's current balance equation using pre-

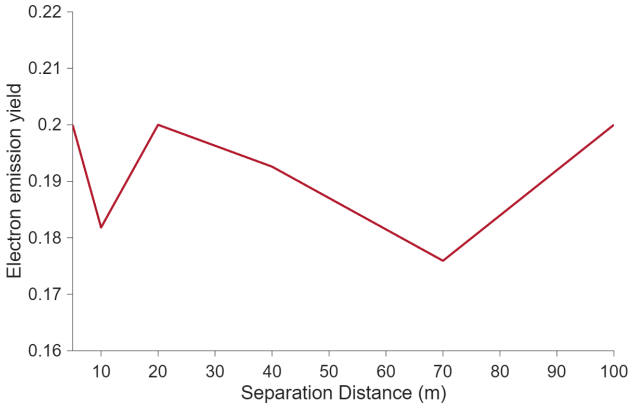

Figure 6.4: Yield from a 0 V spacecraft near a 10 kV spacecraft.

existing parameters δ_B and η_B

$$\begin{aligned} &I_e(V_S,V_T)[1-\alpha(V_S)] - I_{ph}(V_S) - I_i(V_S,V_T)[1-\delta_i(V_S)]... \\ &-I_B(V_S)(1-\kappa_{se}\delta_B(V_S,V_T) - \kappa_{be}\eta_B(V_S,V_T)) + I_{ph,T}(V_S,V_T)... \\ &+I_{e,T}(V_T,V_S)\delta_T(V_S,V_T) + I_{i,T}(V_T,V_S)\delta_{i,T}(V_T,V_S) = 0, \end{aligned} \tag{6.27}$$

where κ_{se} and κ_{se} are the fraction of emitted secondary and backscattered electrons that are recollected by the servicer. To implement this additional source of current, the solver must again be iterated as described in Section 6.3.1, but before this, the proper values for κ_{se} and κ_{be} must be investigated. Different spacecraft geometries will also change the amount of electron emission collected, as shown in Chapter 2, but this must be computed for the specific target geometry of interest. In this work, a general characterization using spherical spacecraft is completed.

SIMION is employed to characterize the fraction of emissions that are recollected. Because the spacecraft are held at 2 m radii, which is smaller than the Debye length, changes to the potential due to nonmonotonic sheaths and spacecraft wakes are not expected, and the beam current is assumed to be low enough to avoid generating barriers. Therefore, SIMION is assumed to appropriately model the recollection behavior. Spherical spacecraft are generated following the fine and coarse potential array (PA) generation described in Chapter 2. The spheres are generated with a resolution of 0.25 mm in the fine PA and 1 m in the coarse PA. When the fine PA elements are decreased to 0.125 mm, negligible change is recorded in the results and the computational time

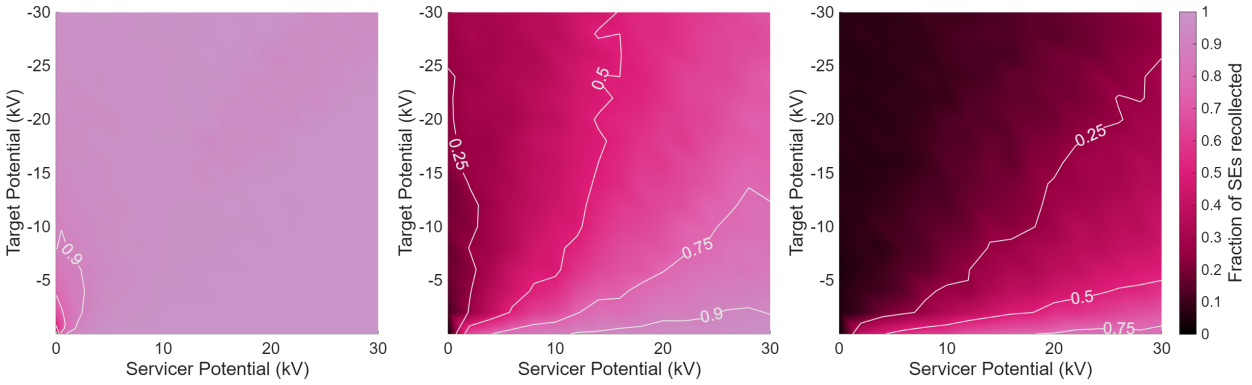

(a) 10 m (b) 20 m (c) 30 m

Figure 6.5: Fraction of secondaries generated by electron beam impact on the target collected by the servicer for varying center-to-center separation distances.

increases by ≈4 times.

6.4.1 Secondary Electrons

Previous work presents detailed descriptions of the emission process for secondary electrons in SIMION [160], which is implemented here. To generate secondary electron emissions, the electron beam energy is set to land on the target's surface with 10 keV of energy the ensure it impacts the center of the target, and one electron is generated for every impacting electron beam electron. This makes the results independent of yields. Figure 6.5 shows the fraction of emitted secondaries recollected for varying separation distances. When the spacecraft are 10 m apart, the servicer consistently collects all emitted secondaries. As the separation distance increases, the servicer collects less of the emissions. This effect is expected to be exacerbated if a short Debye length is present around the spacecraft, such as in low earth orbit or the solar wind when the spacecraft potentials are small.

Figure 6.6 shows that when the half angle of the electron beam is increased, the fraction of secondaries recollected decreases. In this case, more secondaries are generated on the edge of the target, which can then escape the servicer's sphere of influence. This also helps explain why few secondary electron emissions generated by ambient electrons are captured by the service because

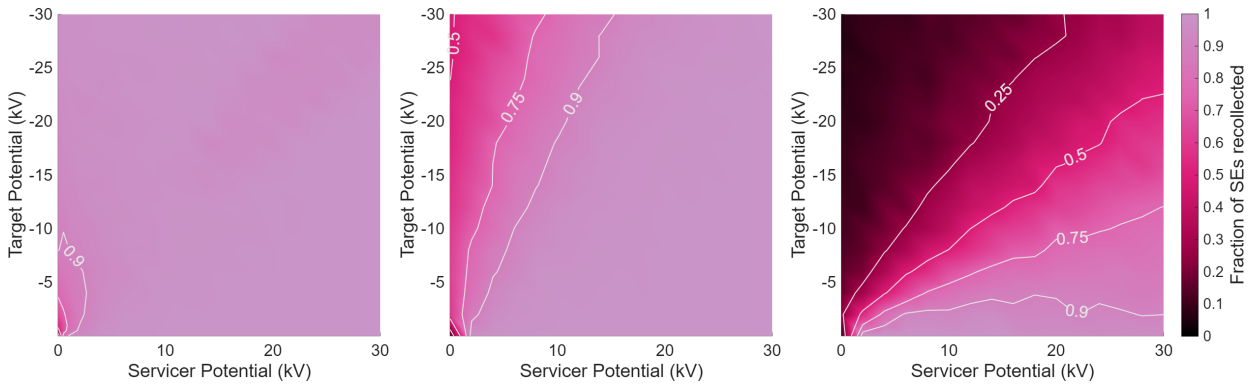

(a) 0° (b) 2° (c) 5°

Figure 6.6: Fraction of secondaries generated by electron beam impact on the target collected by the servicer for varying half angle.

natrually emitted secondaries are genreated from all sides of the target. As an exception, the servicer consistently recollects the majority of the electron emissions when the target potential is low and the servicer potential is large. It should be kept in mind that this is only applicable for spherical spacecraft. For a more complex geometry, a larger half angle can actually enable more efficient recollection of secondary electron emissions, as shown in Chapter 2.

6.4.2 Backscattered Electrons

Backscattered electrons may lose some energy as they traverse through the material, and their peak in energy is near the energy of the incident electron. The peak energy for backscattered electrons from aluminum is ≈2/3 the energy of the incident electrons [68], and legacy versions of SPIS have initialized backscattered electrons with 2/3 the energy of incident electrons.[1] Therefore, the backscattered electrons are initialized with 2/3 the energy of incident electrons. The electron beam is assumed to hit the target perpendicular to the surface, so the angular distribution is defined following a cosine law with respect to the surface normal vector [68]. The simulation is again initialized such that one backscattered electron is emitted for every incident electron, making these results independent of the yield.

[1] See presentation outlining SPIS software tool at SPIS presentation

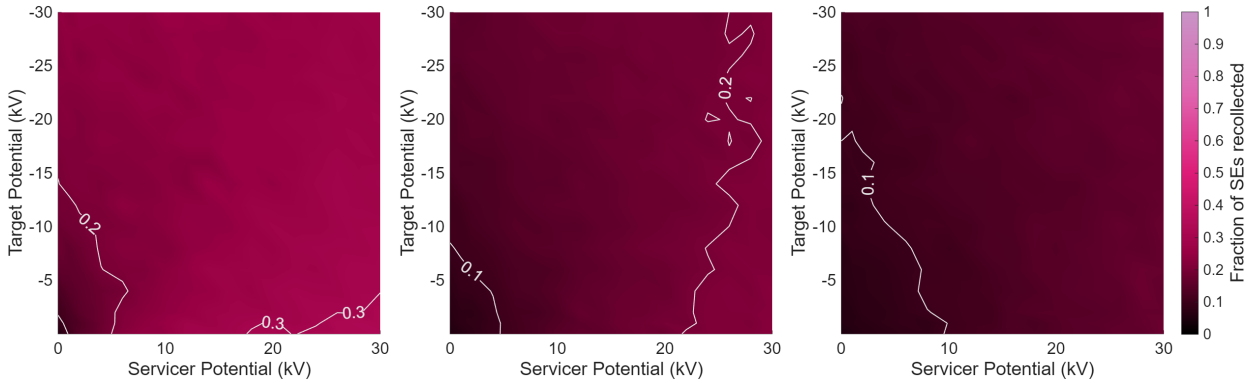

(a) 1 keV landing energy (b) 5 keV landing energy (c) 10 keV landing energy

Figure 6.7: Fraction of backscattered electrons recollected by the servicer for varying beam landing energies, 0° half angle, and 10 m separation distance.

Figure 6.7 shows the fraction of emitted backscattered electrons recollected by the servicer at a 10 m center-to-center separation distance and 0° half angle for varying landing energies. At a landing energy of 1 keV, the servicer recollected a maximum of 0.32 times the emitted backscattered electrons. When the landing energy increases, thereby increasing the emission energy, the number of backscattered electrons recollected decreases. This occurs because the more energetic backscattered emissions are able to escape the sphere of influence more efficiently than the lower energy secondary electron emissions.

6.4.3 Impact on Charging

The importance of electron emission recollection is investigated by determining the resulting potentials with and without recollection included in the computation. The repulsion of like charges is also included in the computations. The calculations are completed in the mean plasma sheet from Table 1.1 with electron and ion temperatures of 150 eV and 780 eV, respectively, and electron and ion densities of 2.2E5 m^{-3} and 2E5 m^{-3}, respectively. The spacecraft both have a 2 m radius and a center-to-center separation distance of 10 m.

Figure 6.8 shows that with no recollection, the servicer charges to approximately match the beam energy of 30 keV and the target minimally charges. With 30% of backscattered emissions

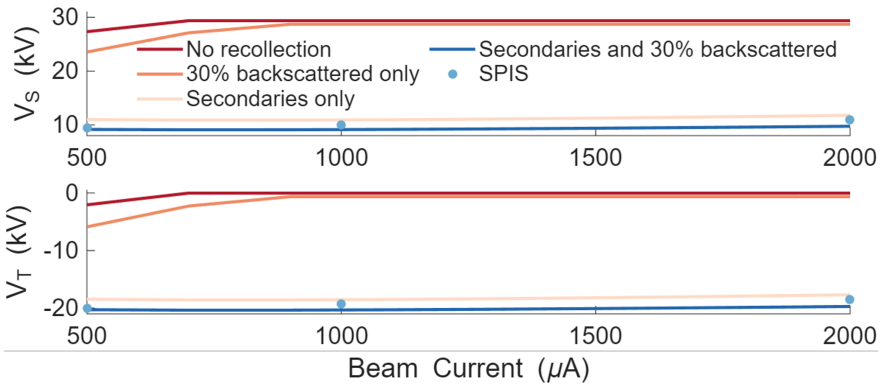

Figure 6.8: Charging and forces with different recollections of 2 m spacecraft with a 10 m separation distance and a 30 keV beam.

recollected, approximately the maximum amount seen in the characterization, the servicer charges a few kilovolts more negative. When secondary electron emissions are recollected, the servicer charges significantly more negative, only charging to approximately 11 keV. With both emissions recollected, the servicer charges to approximately 10 keV. Therefore, secondary electron recollection is more significant than backscattered recollection, and the backscattered current can likely excluded in most cases. Because a collimated beam and close separation distance are typically assumed for electrostatic actuation computations, it is also reasonable to assume that all emitted secondaries are recollected by the servicer during charging operations ($\kappa_{se} = 1$). For a more accurate computation, the characterization results can be interpolated to determine the κ values.

The same charging scenario is also simulated in SPIS. The spacecraft have a 0.15 m resolution on the surface, the boundary is 1000 m from the spacecraft with a resolution of 50 m, approximately 1/3 the Debye length. A 0 V Dirichlet boundary is set for the electric field boundary, and an open boundary is defined for the particles. The simulation is run for 500, 1000, and 2000 μA beam currents, and the results are scattered in Fig. 6.8. As shown, the results with recollection and sheath overlap included closely align with the results with only secondaries and both secondaries and backscattered electrons recollected, indicating that recollection is properly included in the analytic approximation.

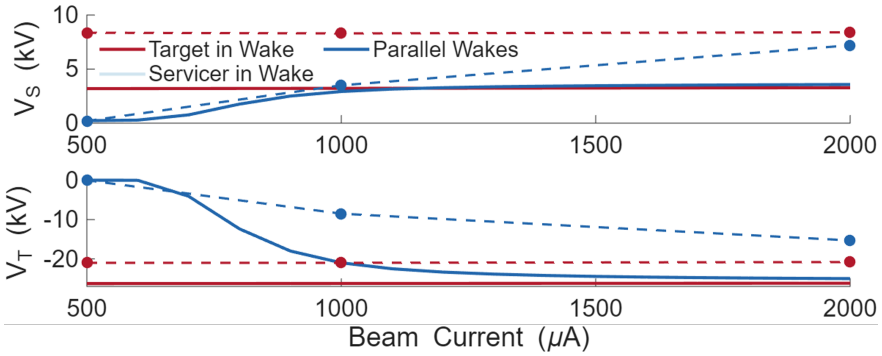

Figure 6.9: Servicer and target potentials in Solar Wind. Dashed lines indicate the SPIS solutions and solid lines indicate analytic solutions.

6.5 Ion current within a wake

As was shown in Chapter 4, if an object is in the wake of a spacecraft, the ion current collection is reduced and the object charges more negatively. Simulations of the electrostatic tractor in SPIS also indicate that this behavior is expected during electrostatic tractor operations. Figure 6.9 shows the servicer and target potentials for varying spacecraft positions. The spacecraft are in the mean solar wind environment, both have a 2 m radius, a 10 m center-to-center separation distance, and a 30 keV beam is equipped on the servicer .The spacecraft have a surface resolution of 0.15 m, boundary resolution of 5 m, and the boundary is 80 m from the spacecraft. The dashed lines indicate the SPIS solutions and the solid lines indicate analytic solutions. For additional visualization, Fig. 6.10 shows the steady state ion density about the spacecraft for a beam current of 1000 μA. When the target is in the servicer's wake, it charges more negatively at lower beam currents than the other two positions in SPIS. Upon evaluation, it is seen that there is no ion current to the target when it is in the servicer's wake in the tested scenarios, so the ion current to the target is set to zero to determine the analytic solution for the target in the wake. This is a simplified assumption because there are conditions when the target is expected to collect ion current even when it is in the servicer's wake. Therefore, the ion current to a target in a positive servicer's wake is characterized.

Several studies have numerically and experimentally investigated the change in ion current

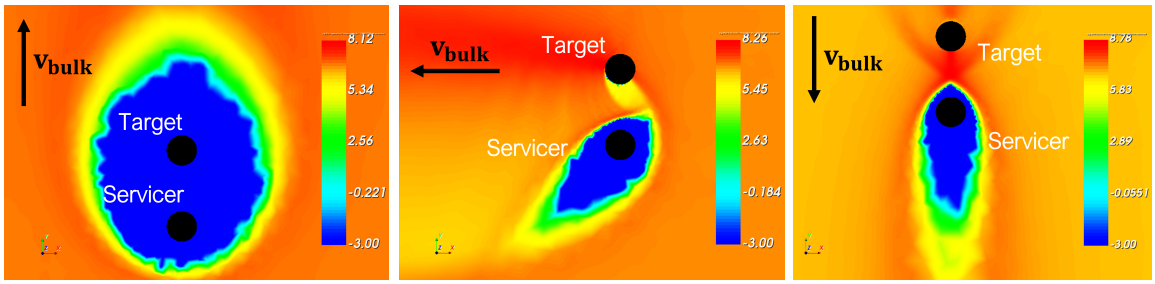

(a) Target in wake (b) Parallel wakes (c) Servicer in wake

Figure 6.10: Wake formation ($\log_{10}$ of the ion density) around spacecraft in varying relative positions during electrostatic tractor operations.

to an object in a wake and the structure of the spacecraft wake. Biasca and Wang [24] characterize the ion current to a highly negative object in the wake of a larger unbiased body in representative LEO plasma using PIC simulations. Histograms of the particle collections are presented to provide insight into the potential at which the probe begins to collect ion current, but the complicated ion trajectories prevent an approximation of the initial collection point from being developed. Wang et al. [198] shows that severe charging can occur when an object in is the wake of a body in the LEO auroral region. Enloe et al. [56] experimentally investigate the ion current to instruments within an expanding ion wake and show that results in SIMION for the initial collection point correlate reasonably well to the experimental solutions. Albarran and Barjatya [1] use SPIS to simulate the wake behind a cubesat in LEO space and implement a simple Matlab particle tracking code to roughly simulate the wake formation.

These works emphasize the difficulty of characterizing the wake formation and change in current. Wake characterization work has generally been completed with representative LEO parameters, since the majority of spacecraft missions with wake formations have taken place in this region. LEO is a thin sheath regime, while the wake formations around lunar spacecraft are possible in the thin and thick sheath regime.[2] Since lunar spacecraft may often be in the thick sheath regime, this work focuses on characterizing the ion current and wake formation for spacecraft in the thick sheath regime in cislunar space.

[2] An overview of the thin and thick sheath regimes is presented in Chapter 4.

6.5.1 SPIS Setup

It is proposed that the ion current to a negative target in the wake of a positive servicer can be approximated by implementing a current reduction factor f and the initial potential at which current is collected V_0 into the SOML equation as

$$I_i(V) = f q_e A_{\text{ram}} n_i v_{\text{bulk}} \left(1 - \frac{2q_e(V - V_0)}{m_i v_{\text{bulk}}^2}\right) \quad \text{for } V < 0. \tag{6.28}$$

To determine these parameters, a constant potential servicer and target are simulated in SPIS, and the ion current to the target is recorded. By simulating a range of target potentials, the current versus potential curve is generated and can be fit to Eqn. 6.5.1 determine f and V_0. Simulations are conducted in SPIS in the solar wind dayside environment.

A 0 V Dirichlet boundary condition is implemented, and the external boundary is set far enough from the spacecraft to allow the potential to naturally reach zero before reaching the boundary (again typically ≈6-10λ_D).The spacecraft surface resolution is 0.1 m, and the external boundary resolution is 5 m, about half the Debye length. Open boundaries are defined for the particles. The ambient electrons and ions are modeled as PIC. The maximum integration time for all particles is set to 5E-7 s, approximately the time it takes the ions to cross the smallest mesh tetrahedral. The total run time is at least 2E-4 s, the time it takes the ions to cross the entire computational space. The simulations take from 5 to 45 minutes on a 32 GB desktop.

6.5.2 Results and Discussion

Figure 6.11 shows the ion current density versus target potential for varying separation distances, servicer potentials, and spacecraft size ratios. The solid orange line indicates the SOML current, and the dotted-and-dashed orange line indicates the SPIS results when no servicer is present. These lines show good correlation, indicating that the SPIS results are representative of the cislunar solar wind environment. As expected, the ion current to the target when a servicer is generating a wake is a fraction of the SOML current.

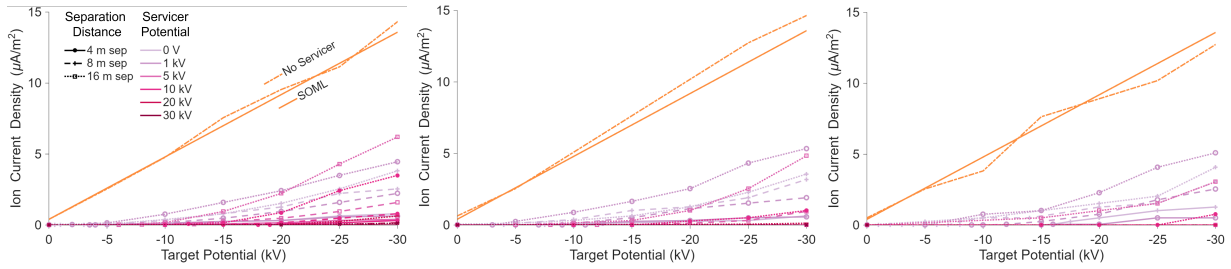

(a) 2:1 ratio (b) 4:1 ratio (c) 8:1 ratio

Figure 6.11: Ion current collected by targets of varying servicer-to-target radius ratios in the wake of a servicer. Orange lines indicate current collected without a servicer present.

Initial Collection Potential The target potentials at which ion current begins to be collected V_0 are shown in Fig. 6.12, with varying separation distances shown with different line styles and different servicer-to-target radii ratios shown with different colors. As the separation distance increases for the same ratio of servicer-to-target radii, the target potential required to begin ion current collected decreases in magnitude. In this case, the flowing ions have more time to be deflected into the surface of the target, requiring a smaller deflection angle and target potential. Similarly, a smaller target potential is required to begin collecting ion current when the radii ratio is larger. The potential generated by a spherical spacecraft is proportional to the craft radius (Eqn. (3.4) and (3.2)), so a larger target generates a farther reaching potential than a smaller target at the same surface potential.

Reduction Factor Nn Fig. 6.11, the ion current to the target does not appear to increase linearly with the target potential. This is verified when the collected ion current in SPIS is divided by the expected SOML ion current to show the reduction factor in Fig. 6.13(a). In fact, the reduction factor appears to increase linearly with the target's potential. Since the reduction factor f is linearly proportional to V_T, the target's ion current is proportional to V_T^2 instead of V_T. Under these conditions, the ion current to the target in the wake will catch up to the ion current without the servicer present if the target becomes negative enough. In this case, the target essentially collapse the wake about the servicer entirely, and the ion current to the target is negligibly impacted by the presence of the leading servicer. As seen in Fig. 6.11, this does not happen in the range of potentials

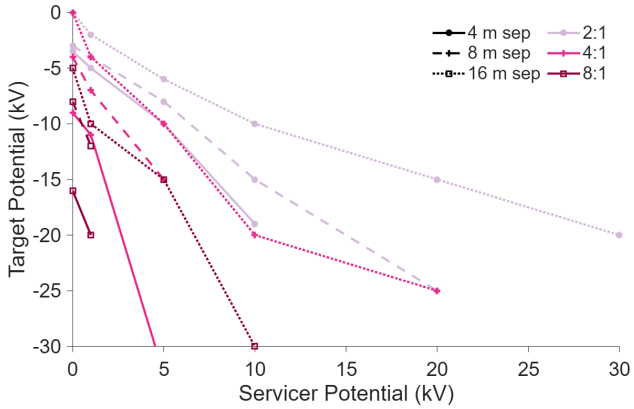

Figure 6.12: Target potential at which ion current begins to be collected (V_0)

tested, so it is likely the target would have to become exceedingly negative to reach this point in cislunar plasma. The ion current to the target with the linear reduction factor f and characterized V_0 is shown over some of the ion current results in Fig. 6.13(b). The fit shows good correlation to the results from SPIS, indicating that this is a good approximation for the ion current to a target in the wake of a servicer in solar wind plasma.

The slopes and y-intercepts of the linear reduction factor fits are shown in Fig. 6.14. In general, the slope is smaller for a more positive servicer, which makes sense because a more positive servicer generates a larger wake, which then limits the rate at which a target can collect ion current. In addition, the slope is larger for a larger separation distance, which corresponds to the initial current collection results because a larger separation distance allows the target to more easily change the ion trajectory and increase the ion current. In general, the y-intercept appears to be larger in magnitude for a larger separation distance, but there is not a clear relationship between the intercept and servicer potential or spacecraft size.

6.5.3 Analysis of Wake Behavior

6.5.3.1 Single Spacecraft Wake Modeling

The characterization results can be included within the charging equations and interpolated to determine the appropriate current when the target is in the servicer's wake. It would be ideal

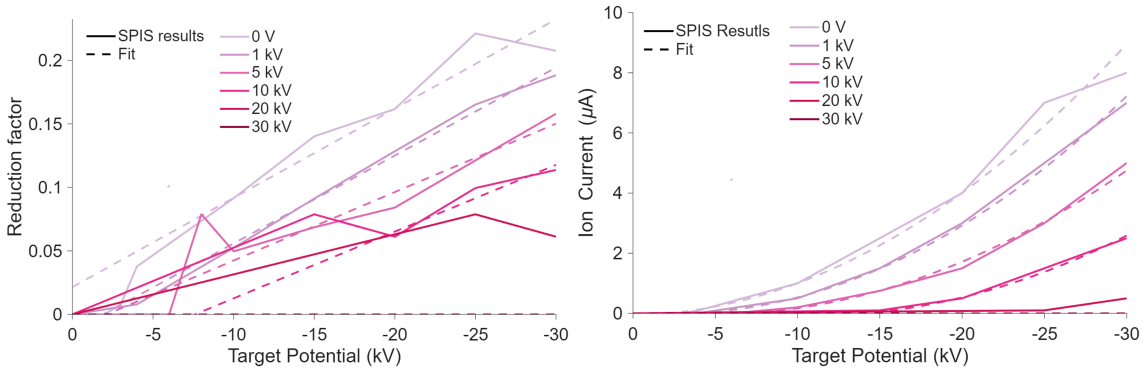

(a) Reduction Factor (b) Ion Current

Figure 6.13: The reduction factor and current for a 2:1 servicer-to-target radii ratio and 8 m separation distance for varying servicer potentials.

to also have the capability to determine if the target is collecting ion current outside the range of parameters tested without conducting a significant number of SPIS simulations. Therefore, the wake behavior is investigated to determine if it is possible to predict the initial collection point using a simplified particle trajectory integrator in Matlab. As previously mentioned, the initial ion collection point has been investigated in previous studies, but a conclusive solution has not been found [24, 56, 161].

Matlab Simulation To gain a better understanding of the wake behavior, the ion trajectories around a single spacecraft are modeled in Matlab. When evaluating the charging behavior of an object in a spacecraft wake, an approximation commonly implemented is that the wake size about an uncharged spacecraft is a ratio between the ion thermal velocity and bulk velocity. The ion thermal velocity is assumed to contribute to the closure of the wake, while the bulk velocity contributes to the length of the wake. Figure 6.15 shows a simplified wake shape about an uncharged with the two velocity components.

Once the spacecraft begins to charge, the trajectories of the ions change accordingly. As explained in Section 4.2.1, a more positive spacecraft can expand the size of the wake while a more negative spacecraft can decrease the size of the wake. To investigate this, flowing H^+ ions are propagated using an ode45 integrator in Matlab. The ions are initialized with velocities of v_{bulk}

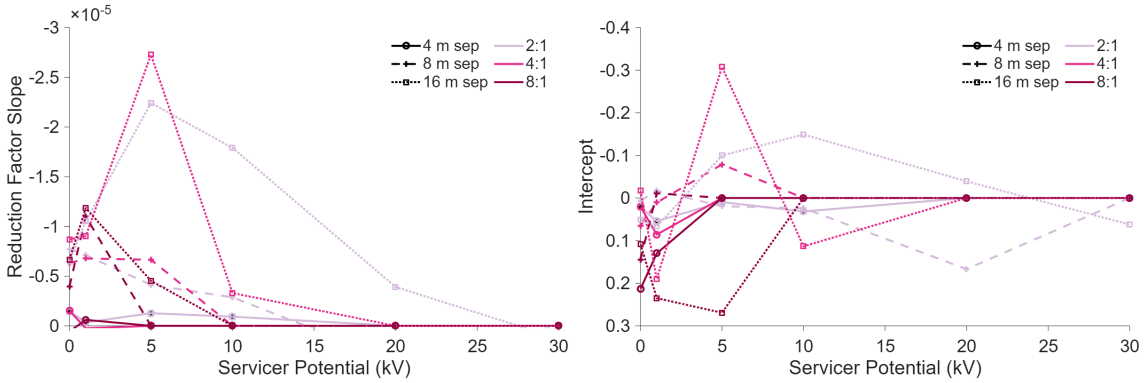

(a) Slope (b) Intercept

Figure 6.14: The reduction factor linear fit slope and intercept.

in the x-direction, and $\pm v_i$ and $\pm 2v_i$ in the y-direction. It is possible for twice the velocity of the thermal ions to contribute to the closure of the wake by assuming the ions are isotropic and cannot originate from inside the wake. In Fig. 6.15, this would mean that thermal ions in the $+\hat{y}$ region at the edge of the wake can travel in the $\pm\hat{x}$ and $-\hat{y}$ direction, but not the $+\hat{y}$ direction. In this case, the velocities in the $\hat{x}$ direction cancel out, and the sum of all the velocity components in the $-\hat{y}$ direction can be computed with the integral

$$-v_i\hat{y} = -v_i \int_0^{\pi} sin(\theta)d\theta = -2v_i. \tag{6.29}$$

Once the particles have been initialized, the acceleration of the ions due to the electric field generated by a spherical spacecraft is computed as

$$\vec{a}_e = \frac{q_e\vec{E}}{m_i}, \tag{6.30}$$

where $\hat{E}$ is the electric field found using Eqn. (3.5) in vector notation as

$$\vec{E}(\vec{r}) = \frac{V_{\mathrm{SC}}R_{\mathrm{SC}}}{r^2}e^{\frac{-(r-R_{\mathrm{SC}})}{\alpha\lambda_D}}\left(1+\frac{\vec{r}}{\alpha\lambda_D}\right), \tag{6.31}$$

where $\vec{r}$ is the vector from the center of the sphere to the particle location. The scaling parameters found using SPIS in Chapter 3 are implemented for α.

As mentioned, the ion wakes generated around the spacecraft do not expand indefinitely due to the movement of the thermal velocity component. To account for the closure of the wake, the

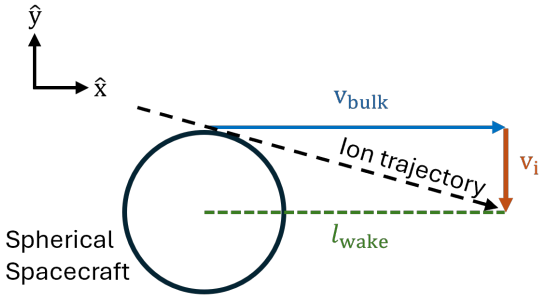

Figure 6.15: Ion trajectory at edge of wake formation about an uncharged spacecraft

thermal velocity of ions is assumed to be directed into the center of the wake, and the magnitude of the thermal velocity component about a charged sphere at each propagation step is

$$v_i = \int_{\phi(r)}^{\infty} E_i f_{E_i}(E_i) \mathrm{d}E_i \quad \text{for } \phi(r) > 0, \tag{6.32a}$$

$$v_i = \int_{0}^{\infty} E_i f_{E_i}(E_i) \mathrm{d}E_i = \sqrt{\frac{2q_e T_i}{m_p}} \quad \text{for } \phi(r) \leq 0, \tag{6.32b}$$

where E_i is the ion energies and f_{E_i} is the maxwellian energy distribution found using Eqn. (6.2). Essentially, if the potential at the particle location is positive, only the fraction of the distribution of the ion thermal velocity that is more energetic than the potential value at that point is assumed to contribute to closing the wake. If the potential at that point is negative, the entire thermal velocity distribution contributes to the wake closure.

The resulting trajectories for spacecraft at varying potentials is shown in Fig. 6.16. As shown in SPIS, the wake can be divided into different regions. The "deep wake" has no ion density and is shown in blue, the "outer wake" is the outermost region of the wake with some ion density is shown in light yellow, and the "transitional wake" region between the two is shown in green. In Matlab, the ions initialized with thermal velocity $2v_i$ going into the wake trace the blue deep wake region, those initialized with v_i directed away from the wake outline the light yellow outer wake, and those initialized with v_i into the wake outline the green transition region. In the Matlab legend, a negative value indicates the velocity going into the wake while a positive value indicates velocity going away from the wake. This indicates that the initial trajectory of the ions determines shape and size of the different regions of the wake.

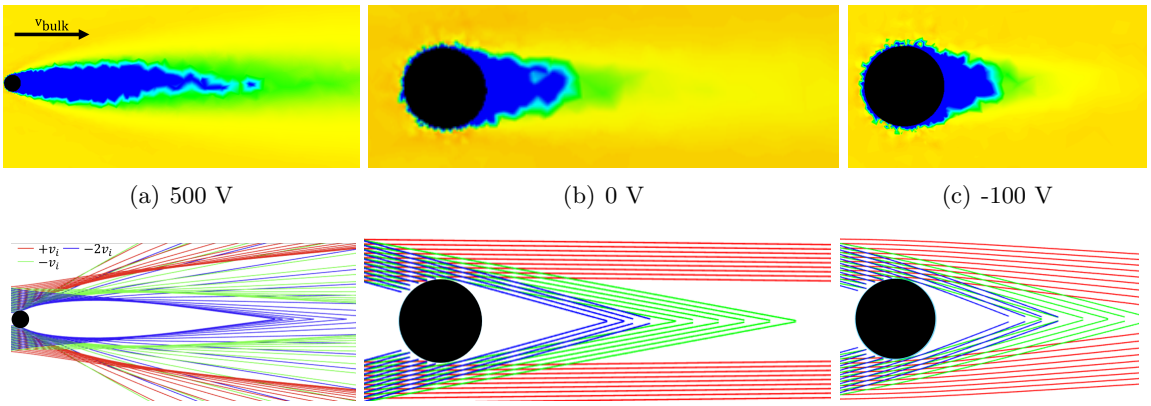

(a) 500 V (b) 0 V (c) -100 V

(d) 500 V (e) 0 V (f) -100 V

Figure 6.16: SPIS wake results ($\log_{10}$ of the ion density) and corresponding Matlab wake propagation.

The wake formations in SPIS also show undulations on the edge of the wake formation that are not captured in the Matlab code. This could be a result of the mesh sizing in SPIS because the ion density is resolved within one mesh element, physical turbulence in the fully PIC plasma, or a combination of the two.

Experimental Representation The different regions of the wake can be recreated in the ECLIPS chamber using the focusing lens developed in Chapter 5 to validate that the changing initial conditions results in the different wake regions. In this experiment, a 2.5 cm radius aluminum sphere is placed in the path of the ion gun to generate a wake, and the focusing lens is using the change the initial trajectory of the ions to simulate the varying initial conditions.

Figure 6.17 shows the wake experiment setup and expected beam trajectory around an uncharged spacecraft in SIMION. The initial divergence angle of the beam is assumed to be approximately 4.9° based on the characterization done in Section 5.2.2. This represents the conditions in which the ion thermal velocity is initialized in the direction facing out of the wake formation ($+v_i$) and the outer wake region is outlined. A 450 V focusing lens potential generates a beam with a convergence angle of 4.9°, representing the condition in which the thermal velocity is initialized going into the wake ($-v_i$) and the transitional region is outlined. Converging the beam more to simulate when twice the value of the ion thermal velocity is initialized going into the wake ($-2v_i$)

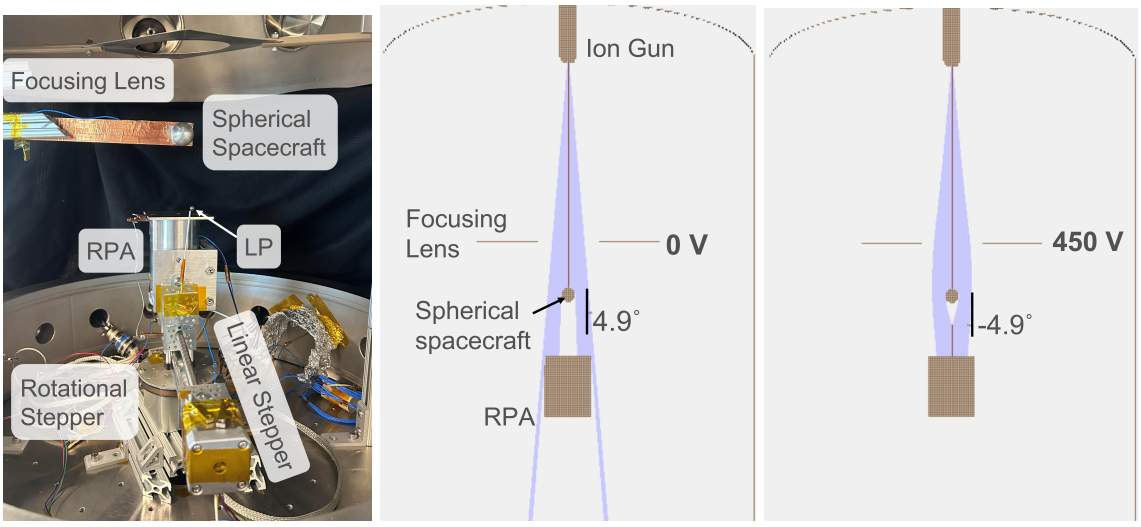

(a) 500 V (b) 0 V (c) -100 V

Figure 6.17: Setup of wake experiments

results to outline the deep wake causes all the ions to impact the ram side of the sphere. Future work is recommended to implement both the expanding and focusing lens to enable an experiment with the deep wake simulated.

Assuming a bulk flow of 400 km/s and a thermal ion flow perpendicular to the bulk flow (similar to Fig. 6.15), an ion temperature of ≈5.2 eV would generate a 4.9° angle between the ion trajectory and bulk flow direction vectors. These values are similar to solar wind conditions. These conditions are modeled in SPIS and compared to the experimental results. Figure 6.18 shows the SPIS and experimental results for a 0 V and 200 V spacecraft. The red vertical line in the SPIS results indicate the representative location in the wake where RPA measurements are conducted. The orange circle in the experimental results show the expected size of the wake region based on the SPIS results.

The experimental results indicate a larger wake than expected from SPIS. It is assumed that the experimental ion beam has a negligible thermal velocity component, so there is not a velocity component closing the wake. Future work is recommended to quantify the thermal velocity component. Because the experimental thermal velocity is assumed to be negligible, the wake formation

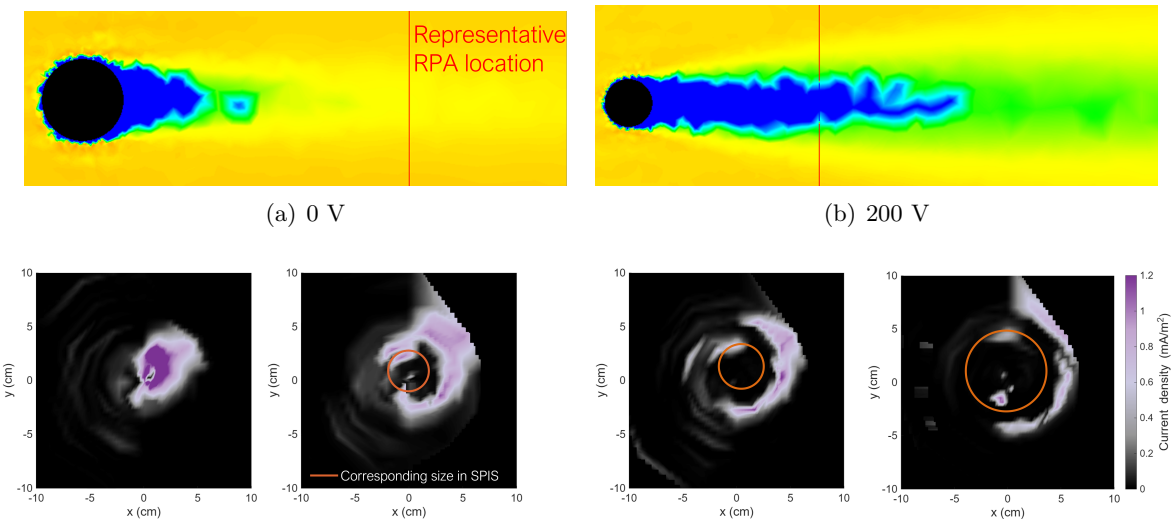

(a) 0 V

(b) 200 V

(c) 0 V sphere, 450 V lens

(d) 0 V sphere, 0 V lens

(e) 200 V sphere, 450 V lens

(f) 200 V sphere, 0 V lens

Figure 6.18: Wake experiment representative SPIS simulations (top) and RPA measurements of the current density (bottom)

is larger than the SPIS simulations which do have a thermal ion velocity component; however, the general behavior of the experimental and SPIS wakes is comparable. The 0 V spacecraft shows a completely closed transitional section of the wake at the RPA location in both SPIS and experiments, but the outer region of the wake persists to the RPA. Both the transitional and outer region of the wake are measured by the RPA behind the 200 V spacecraft. The outer region of the wake around the 200 V spacecraft is ≈1.75 times the transition region in SPIS and 1.6 times in the experiment. Therefore, the relative size of the regions of the wake correlates well between the experiment and SPIS solutions. This indicates that the difference in initial velocity does lead to the different wake regions. This also emphasizes that if the goal of a wake experiment is to capture the size of the wake or initial collection point of a target in the wake, it is important to generate representative initial conditions.

6.5.3.2 Target within Servicer's Wake Modeling

Now that the wake formation around a single spacecraft has been investigated and validated with experiments, the target sphere is modeled in the wake of the servicing sphere. Without a plasma present, the potential and electric fields can be superimposed to determine the potential. In a plasma, the changes to the plasma due to the sheath overlap complicates the potential solution, typically requiring a Poisson-Vlasov solution to determine the fields throughout the region of interest. As was shown in Chapter 3, as the spacecraft become more charged the effective Debye length increases and the potential solution approaches the vacuum solution. Therefore, the vacuum approximation for the fields around the highly charged servicer and target is implemented in this section, and the potential and electric field are superimposed.

The electric field around the two spacecraft is

$$\vec{E}(\vec{r_1}, \vec{r_2}) = k_c \left(\frac{q_1}{r_1^3} \vec{r} + \frac{q_2}{r_2^3} \vec{r_2} \right), \tag{6.33}$$

where the charges $q_{1,2}$ are found using Eqn. (6.2), and $\vec{r}_{1,2}$ are the vectors from the center of spheres to the particle location. With the electric field updated, the acceleration equation is again found using Eqn. (6.30).

The propagated trajectories and corresponding SPIS results about a servicer and target are shown in Fig. 6.19. There is good correlation between the Matlab solution and the outline of the wake regions in SPIS wake for varying spacecraft potentials, sizes, and separation distance. This indicates that the vacuum approximation is a reasonable assumption to make when propagating the ion trajectories about the charged spheres. A Matlab solution with Debye shielding is recommended for future work.

Now that the wake propagation model has been validated against SPIS wake simulations, the target potentials are swept through until ions impact the target to predict the initial collection point. Figure 6.20 shows the predicted initial collection potentials compared to the SPIS results. When the servicer is uncharged, the simulation underestimates the target potential required to collect ion current. With the vacuum assumption, the target's influence on the ion's trajectories may be

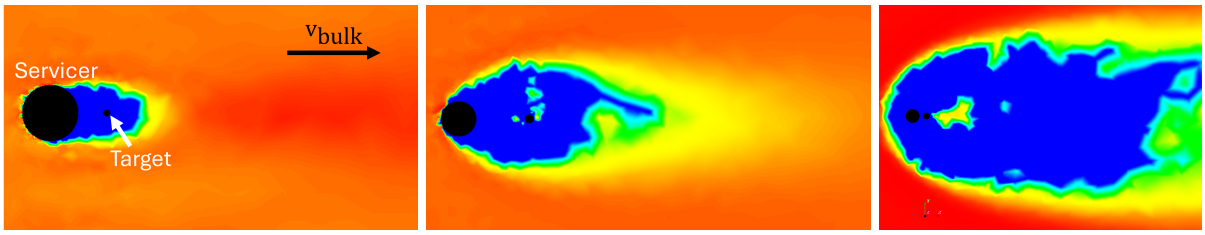

(a) 0 V ser., -8 kV tar., 4 m sep., 8:1 radii ratio (b) 1 kV ser., -7 kV tar., 8 m sep., 4:1 radii ratio (c) 10 kV ser., -19 kV tar., 8 m sep., 2:1 radii ratio

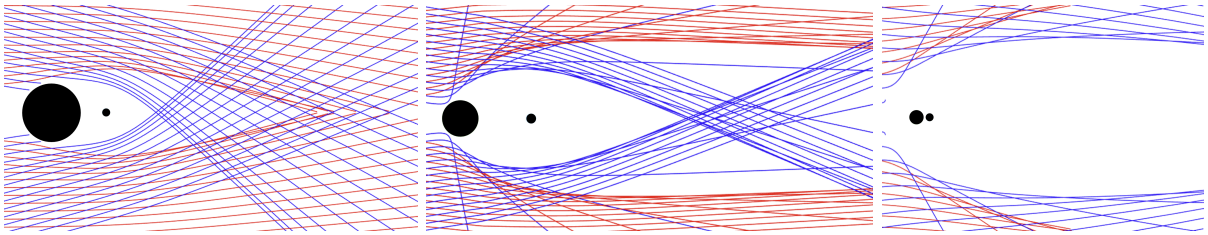

(d) 0 V ser., -8 kV tar., 4 m sep., 8:1 radii ratio (e) 1 kV ser., -7 kV tar., 8 m sep., 4:1 radii ratio (f) 10 kV ser., -19 kV tar., 4 m sep., 2:1 radii ratio

Figure 6.19: SPIS wake results ($\log_{10}$ of the ion density) and corresponding Matlab wake propagation about a servicer and target.

overestimated, resulting in early current collection. At larger servicer potentials, the propagator overestimates the target potential required to collect ion current. This is because in SPIS the wake begins to break up for large target potentials, as is seen in Fig. 6.19(c). When this simulation is run with higher resolution (the element sizes on the surface and boundary are halved), the wake breakup still occurs. Therefore, it is likely that this is physical, but future work is recommended to recreate this phenomena in experimental investigations. Because the Matlab propagator does not account for wake breakup, it overestimates the target potential required to collect ion current. Therefore, while the propagator is a new method that can provide fast insight into the general wake shape, particularly around a single spacecraft, SPIS should still be used to determine if wake breakdown has occurred and ions can reach an object in the wake.

6.5.4 Supercharging Feasibility

In general, it is not considered possible for the difference in potential between two spacecraft to exceed the beam energy if another source of energy is not present; however, a simulation in SPIS

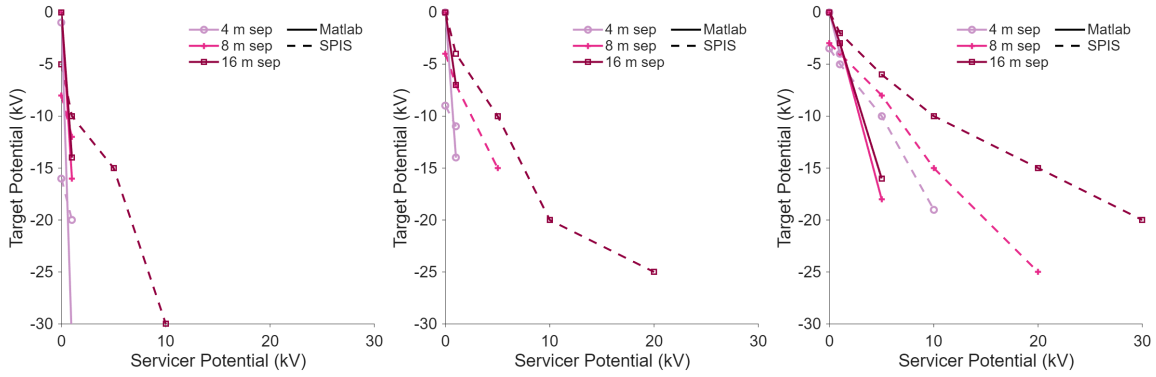

(a) 8:1 radii ratio (b) 4:1 radii ratio (c) 2:1 radii ratio

Figure 6.20: Initial collection target potentials predicted by Matlab propagator (solid lines) compared to results from SPIS (scatter points)

indicates that if the target is within the spacecraft wake it may be possible for the difference in potential to exceed the beam energy under certain conditions.

Figure 6.21 shows the electron beam density, ion density, and potential in a scenario in which the potential difference between the 10 m wide servicer and target is ≈1.3 keV when a 1 keV beam is used to charge the spacecraft. In this scenario, the target first charges to approximately the beam energy while remaining fully enveloped in the wake. Once the difference in potential matches the beam energy, the electron beam no longer impacts the target, the target is sufficiently negative to repel ambient electrons and is fully in the deep wake. Therefore, the sum of currents remains zero and the target remains at -1 kV. Because the electron beam is given an initial divergence angle of 2°, once it is repelled by the target some of the emissions also miss the servicer. This allows the servicer to continue charging more positive until current balance is achieved at 297 V. In this scenario, the target acts as an external source of energy that repels electrons from the sphere of influence of the servicer. This is also validated in a SIMION simulation with the same size and potential spacecraft and same separation distance, where a 1 keV electron beam is repelled by a -1 kV target and not fully recollected by a 297 V servicer.

For supercharging to occur, it is theorized that the beam must be wide enough that when it is repelled by the target not all of the emissions are recollected by the servicer, and the target

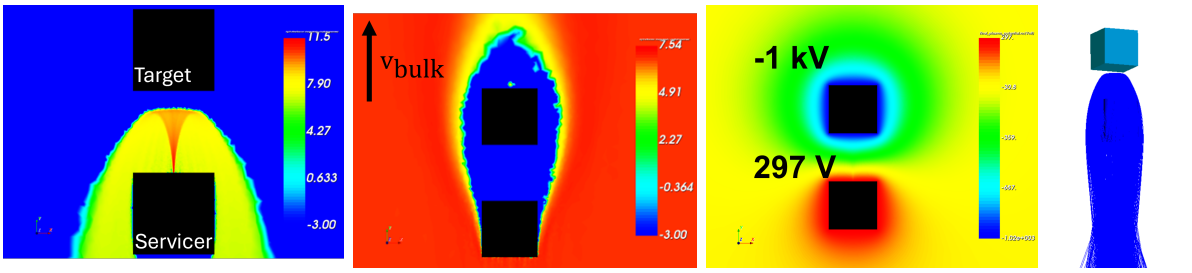

(a) $\log_{10}$ E-beam density (b) $\log_{10}$ ion density (c) Potential (d) SIMION beam

Figure 6.21: SPIS supercharging results for a 1 keV beam and SIMION beam trajectory validation.

must fully inside the deep wake such that it remains at the beam energy when it is no longer being impacted. Under these conditions, it may be possible to increase the potentials of the spacecraft without increasing the energy of the beam, which can lead to larger forces without requiring excess power. In addition, the target could be charged using the electron beam, and then the beam could be turned off or moved while keeping the target fully in the wake and charged. Future work is recommended to characterize this phenomena in cislunar mesothermal plasma.

6.6 Charging and Forces

Now that the charging equations have been expanded to account for sheath overlap, electron emission recollection, and wakes, the resulting charging and forces when using an electron beam to charge the spacecraft in various cislunar environments is investigated.

6.6.1 Beam Impacting Target

6.6.1.1 Initial Charging Currents

The current at which the target's potential begins to change is first investigated in the various cislunar environments. This can provide insight into the current that should be selected when conducting touchless potential sensing if it is undesirable to charge the target spacecraft. This has previously been studied in [82] and shown that the beam current at which the target's potential changes by more than 100 V is typically on the order of 1 μA in sunlight and 0.1 μA in eclipse

cislunar environments. The change in the target's potential for beam currents on the order of μA and a 30 keV beam is presented in Fig. 6.22 for 2 m and 4.5 m radius spacecraft. The 2 m spacecraft allows for comparison with the following charging investigation, and the 4.5 m spacecraft are of a similar size to the spacecraft used for the touchless potential sensing investigation in Chapter 2. In addition, testing two different size spacecraft provides insight into the impact of spacecraft size on change in potential.

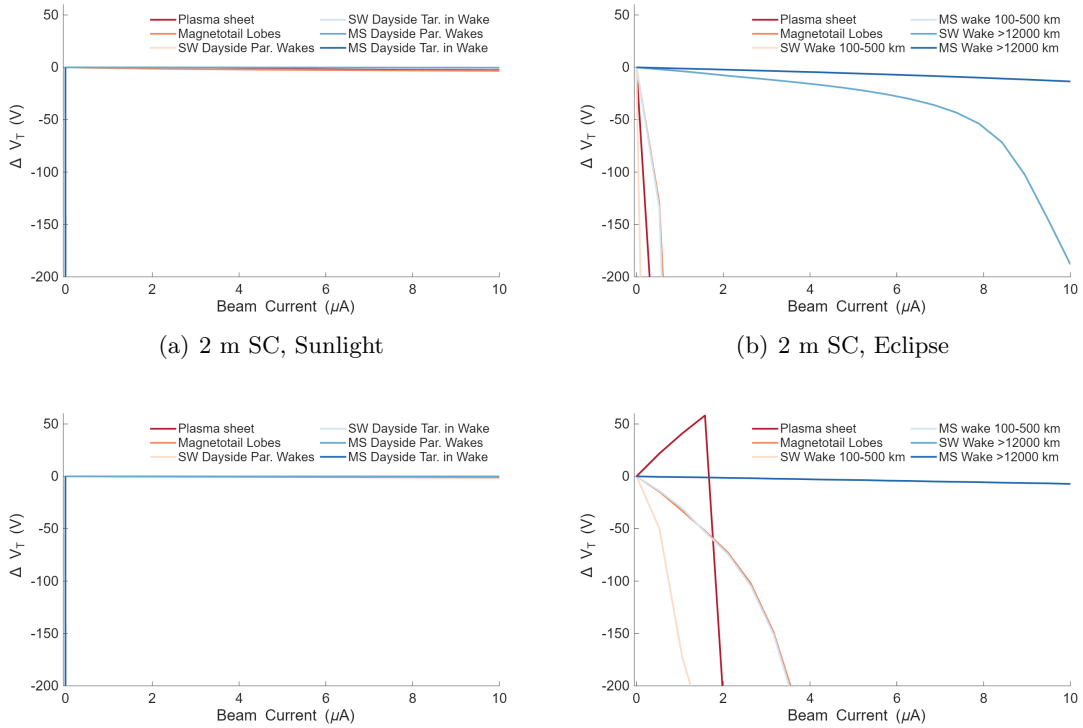

(a) 2 m SC, Sunlight

(b) 2 m SC, Eclipse

(c) 4.5 m SC, Sunlight

(d) 4.5 m SC, Eclipse

Figure 6.22: Change in target potentials for various sunlight and eclipse cislunar environments with a 30 keV beam.

In the sunlit environments when the target is not in the servicer's wake, the target's potential is negligibly changed up to a beam current of 10 μA. When the target is in the servicer's wake, the target appears to charge once any amount of beam current is defined due to the lack of photoelectron and ion current. In eclipse, the target's potential is minimally changed in the comparatively lower energy and higher density environments. In the higher energy environments, such as the magnetotail

lobes and plasma sheet, the target begins to charge for beam currents on the order of 0.1 μA for the 2 m spacecraft and 1 μA for the 4 m spacecraft. A larger target will have a larger magnitude of current from the plasma and radiation environment, assuming consistent fluxes, so the beam current will be lower compared to the ambient environment currents. Therefore, a larger current is necessary to begin charging a larger target.

6.6.2 Electrostatic Actuation Charging

The floating potentials, beam landing energy, and forces are computed in several of the cislunar environments for a 30 keV beam energy, 250 μA to 2000 μA current, 10 m separation distance, 1 m target, and 2 m servicer. Figure 6.23 shows the results as a function of the beam current. In the sunlit environments, the plasma sheet and magnetotail lobes show similar trends, with the servicer charging to ≈10 kV, the target charging to ≈20 kV, and forces near 0.5 mN. The solar wind and magnetosheath environments have lower servicer potentials near 1 kV and target potentials closer to the beam energy, resulting in forces near 0.1 mN.

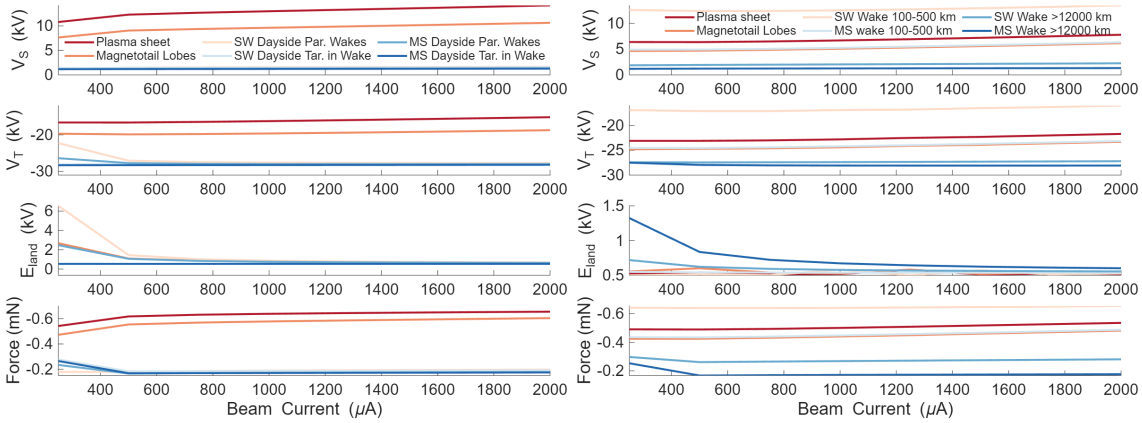

(a) Sunlight (b) Eclipse

Figure 6.23: Charging and forces solutions for various sunlight and eclipse cislunar environments with a 30 keV beam.

In the eclipsed environment, the plasma sheet, magnetotail lobes, and magnetosheath wake from 100-500 km behave similarly with servicer potentials near 5 kV and target potentials near -

25 kV. In these environments, the particles densities are all near 2E5 m^{-3}, the electron temperature is ≈5 times the ion temperature, and the environment is not mesothermal, leading to similar charging behavior. In the higher altitude wake regions, the lunar wake has begun to close and charging behavior resembles the sunlit solar wind and magnetosheath environments. The standout environment in this case is the solar wind wake region from 100-500 km. In this region, the plasma density is near 8E4 m^{-3}, lower than the other environments. As a result, the beam is a more prominent current, and the servicer and target both charge to a magnitude near 15 kV, creating the largest forces in the eclipse environments at 0.65 mN. In general, the electrostatic tractor performance in the sunlit and eclipse regions in the same environment is similar, but the performance varies significantly between environments.

In all environments, the beam landing energy settles at hundreds of volts at larger currents, which indicates that secondary electron emissions should be generated during electrostatic tractor interactions. This indicates that the beam energy would not need to be swept through for touchless potential sensing, simplifying the process to emit observable SE emission outlined in Chapter 2.

6.6.3 No Beam Impact

Now that an approximation for the charging behavior near another highly charged object is implemented in the charging equations, the charging behavior for a servicer and target when the beam is not impacting the target is investigated. This could be useful if impacting an active target may endanger sensitive instruments or components, or if debris is predicted to be nearby but the exact location is not known. In this scenario, the servicer is emitting a 2 mA, 30 keV beam, and the behavior is characterized for a 1 m target and 2 m servicer from 10 to 30 m of separation.

Figure 6.24 shows the resulting potentials and forces. In the sunlit environment, the servicer charges to approximately the beam energy in the plasma sheet and magnetotail lobes, which then charges the target positive as the servicer draws away electron emissions through the process described in Section 6.3.1. This creates a repulsive force instead of the attractive force proposed for electrostatic tractor operations. In the solar wind and magnetosheath regions, the servicer charges

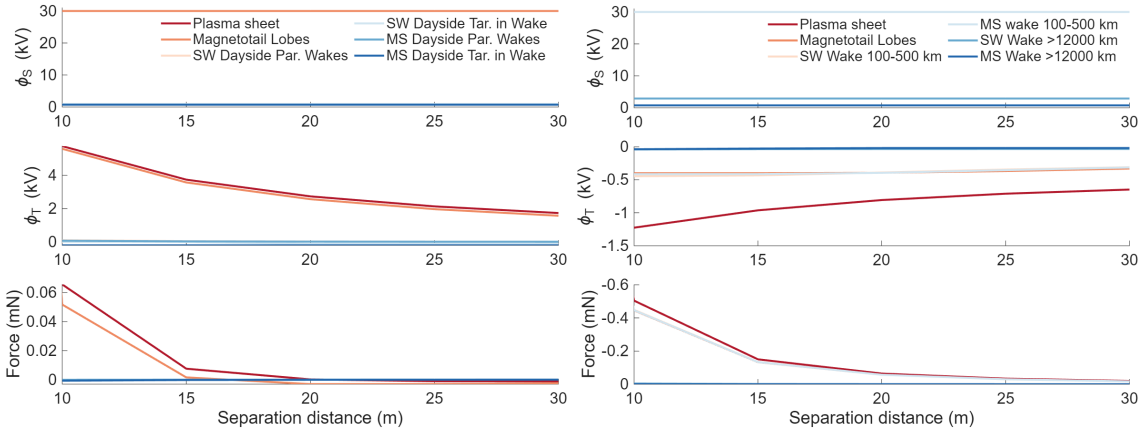

(a) Sunlight (b) Eclipse

Figure 6.24: Charging and forces solutions for various sunlight and eclipse cislunar environments when the beam does not impact the target.

to ≈1 kV and the target charges a up to few hundred volts positive when the wakes are parallel and up to a few hundred volts negative in the wake, similar to the results shown in Figs. 6.1(a) and 6.3, resulting in forces on the order of 0.01 mN. In eclipse, the target charges negatively due to the repulsion of ions by the positively charged servicer, and forces up to 0.5 mN occur at 10 m separation in the plasma sheet, magnetotail lobes, and low altitude solar wind and magnetosheath lunar wake, similar to the forces generated when the beam impacts the target in Fig. 6.23. In the high altitude lunar wake, the servicer charges to ≈1 kV, similar to the dayside results, creating smaller target potentials and forces than the more energetic regions. Therefore, in eclipsed energetic environments, electrostatic tractor operations could be conducted without impacting the target with the electron beam.

6.7 Conclusions

In this chapter, the charging equations for active charging scenarios are adapted to account for proximity interactions between multiple bodies. It is shown that a highly positive servicer can draw electron emissions away from a slightly positive object, charging it highly positive. In addition, the repulsion of ions by a highly positive body can charge a nearby object negative, and

a highly negative body can charge a nearby object positive due to the repulsion of electrons. If a target is impacted by an electron beam, the positive servicer can recollect the electron emissions from the target, resulting in servicer potentials several kilovolts lower than expected.

If the target is in the wake of the servicer, it can charge more negative due to the absence of ions, so the ion current to a target in a servicer's wake is characterized and analyzed. It is shown that a larger target farther from the servicer requires will collect more ion current at lower potentials compared to smaller targets or smaller separation distances from the servicer. In addition, a Matlab particle trajectory propagator is presented that splits the ion velocity components into the bulk flow and thermal velocity and shows excellent agreement with SPIS solutions. It is found that changing the initial trajectory of ions in Matlab simulations leads to different regions of the wake being outlined, which is validated in experiments with the focusing lens in the ECLIPS chamber. This presents a new method of generating the outline of a wake formation in a simple propagation code. The general shape of the wake about two spacecraft is also recreated in the Matlab propagator, but wake break up that occurs for large target potentials is not captued. As a result, the Matlab solutions underestimate the ion current to the target in the wake. The propagation results therefore provide a first look at the general wake formation about two spacecraft, but SPIS results are required to spot-check the ion current to a body in a wake.

Utilizing the proximity charging approximations, it is shown that the largest electrostatic forces are generated in energetic plasma environments. When the beam impacts the target, the force magnitudes are comparable in both sunlight and eclipse. When the beam does not impact the target, repulsive forces are generated in sunlit environments. In energetic eclipse environments, attractive electrostatic forces of similar magnitudes are generated when the beam does and does not impact the target. This enables electrostatic tractor operations even if impacting the target is undesirable or difficult.

Chapter 7

Conclusions and Future Work

7.1 Overview and contributions of this work

While the amount of debris is lower in cislunar space compared to regions such as LEO and GEO, the consequences of debris accumulation around the moon require methods to safely manage spacecraft at their end of life to be implemented now. To maneuver debris, decrease the risk of arcing during docking, and investigate lunar dust behavior for missions around the moon, electrostatic actuation and touchless potential sensing technology is proposed for application in cislunar space. This technology has been investigated for application in GEO space, but spacecraft-plasma interactions around the moon present new phenomena that have not been considered in previous studies. Therefore, outstanding questions related to this technology are addressed, and the impact of cislunar plasma is determined.

Touchless potential sensing using electron emissions has previously been validated in vacuum chamber experiments and complementary charged particle tracing simulations. It has been shown that these emissions are difficult to detect, particularly when the target has multiple components or is differentially charged. In Chapter 2, it is shown that around a uniform target, the electron emission trajectories are consistent regardless of changes in the servicer's and target's potentials, which allows the trajectories to be predetermined and implemented in guidance controls. If differential potentials develop on the target, the electron emission trajectories can vary significantly. In this case, it is best to increase the servicer's distance from components that can be biased positively, or the x-ray method can be implemented until finer resolution measurements of the target's

potential can be achieved with the electron emission method. When an electron beam or VUV laser is used to generate electron emissions, it is best to increase the half angle of the instrument and deflect the equipment until electron emissions are detected. If the target is uniformly charged, similar observability of electron emissions is achieved with an electron beam or VUV laser, but if the target is differentially charged the VUV laser can more reliable emit detectable emissions.

Once the observability of electron emissions is addressed, the cislunar plasma environment impact on sensing is investigated. First, Debye shielding of potentials around a servicing spacecraft is characterized in Chapter 3. It is shown that large servicer potentials or spacecraft radii can increase the sphere of influence of a charged spacecraft, allowing it to pull in emitted electrons more efficiently; however, the more positive servicer also draws in ambient electrons more efficiently. As a result, minimizing the potential of the servicer is better for passive potential sensing operations despite the smaller sphere of influence. In a sunlit environment, a highly positive servicer can draw electron emissions away from a target, causing it to charge approximately to the value of the potential field generated by the servicer at the target's location. In an eclipsed environment, a highly positive servicer causes the target to charge more negative, which leads to decreased electron current and electron emissions. As a result, the separation distance proposed for passive sensing using a highly positive servicer in eclipse is approximately twice the effective Debye length.

The impacts of flowing plasma and barriers are then included in simulation studies in Chapter 4. It is shown that nonmonotonic sheath and spacecraft wake barriers can form around low potential spacecraft if their width is at least half the Debye length. In addition, barriers from electron beam emissions can form if the spacecraft potential is low and the beam current is high. Fortunately, a large beam current typically generates large spacecraft potentials, avoiding the formation of barriers due to electron beam emissions. It is shown in passive potential sensing simulations that less current is detected from a separation distance of one spacecraft width if the spacecraft are larger and barrier formations are expected. Despite the lower signal, passive potential sensing is still feasible, and the electron emissions can be differentiated from the ambient plasma environment when a low potential ($< 300\ V$) servicer is used. The largest limitation for passive potential sensing

occurs when the target is in the wake of a positive servicer because the target charges negative enough to repel ambient electrons. Without the ambient electrons impacting the target, no electron emissions are generated for sensing. In this case, the servicer's potential can be decreased to decrease the size of the wake or active potential sensing methods can be deployed. Active potential sensing simulations also indicate that the detected electron emission current can be orders of magnitude larger than the ambient electron current, showing that active potential sensing is also feasible.

To complement simulation results, Chapter 5 shows the development of wake experiments for the ECLIPS vacuum chamber. Thin electrostatic lenses are designed and characterized in the chamber to expand the ion beam and stop the expansion of the ions as they pass a representative spacecraft. It is found that if the expanding lens is off-center by sub-millimeter distances, the ion beam is significantly translated, complicating wake experiments. Fortunately, both the expanding and focusing lenses change the radius of the ion beam as expected, despite beam translations. The beam is then expanded wide enough to generate spacecraft wakes about a cube in the ECLIPS chamber. This work presents a novel analysis of simple electrostatic lenses installed externally from a charged beam. The lenses are used to generate spacecraft wakes for this investigation but could be applied to any environment where a beam needs to be widened, focused, or translated beyond its pre-existing capabilities.

Finally, Chapter 6 characterizes the proximity currents and charging behaviors using particle-in-cell simulations and experiments in the ECLIPS chamber. It is shown that a highly positive servicer can draw electron emissions away from a sunlit object, charging it significantly more positive than it would without the presence of the servicer nearby. Similarly, a highly charged object can repel ambient particles of the same charge, causing nearby objects to charge in the opposite direction to counteract this repulsion. These interactions can be used to charge a target without impacting it with an electron beam, and in energetic eclipsed environments the resulting electrostatic forces is similar regardless of if the beam impacts a target. In addition, the ion current to a target in the wake of the servicer is characterized for cislunar plasma. It is shown that smaller

targets closer to the servicer must charge more negative to begin collecting ion current. A novel Matlab ion trajectory simulation shows that different regions of the wake form depending on the initial trajectories of the ions. This result is validated in wake experiments in ECLIPS when the focusing lens is used to change the initial ion trajectory.

7.2 Directions for future work

Significant strides have been made to enable electrostatic actuation and touchless potential sensing in varying plasma environment, but further work is recommended to continue to generalize this technology to different regions, expand upon the results, and raise the TRL level of the proposed technology. To raise the TRL, vacuum chamber demonstrations should be conducted with floating spacecraft in a generated plasma. Furthermore, dielectric materials and solar cells have not been included in the analysis and their impact should be studied. The sensing strategies should also be integrated with guidance controls to manipulate the beam and servicer position to emit and detects electrons and x-rays for touchless potential sensing.

These investigations are presented assuming Maxwellian plasma distributions. It would be of interest to apply a kappa distribution to the plasma and determine the difference in performance in this higher energy distribution. In a similar manner, the wake formation investigation is completed assuming the spacecraft are smaller than the Debye length. If the spacecraft are larger, negative potential fields can develop in the wake, particularly in the enhanced wakes around highly positive servicers. This may have interesting impacts on the electrostatic forces and wake formation. Furthermore, the supercharging phenomena when the target is in the servicer's wake should be characterized more in depth.

The investigations on proximity operations relaxed several assumptions implemented in previous work. Future work could expand on the wake investigation and determine the change in ion current in mesothermal plasma when a highly charged spacecraft is nearby but is not generating a wake around the object of interest. Charging methods such as pulsed electron beams could also be implemented to determine how the charging behavior responds to oscillating plasma and electron

beam parameters. In general, robust charging controls should be developed to manipulate the servicer and target potentials despite variations in the ambient plasma or emission properties.

It would be exciting to apply the touchless potential sensing methods to determine the charging of the lunar surface itself. The lunar surface is expected to develop a charge, and because the regolith is assumed to be dielectric, negative surface potential can arise in shaded regions. This, combined with triboelectric charging, poses a danger for humans and rovers moving on the lunar surface. Touchless potential sensing could be used to determine the potential of a region of the moon before making contact, minimizing the danger of electrostatic discharges between the surface and astronaut or vehicle.

Bibliography

[1] Robert M. Albarran and Aroh Barjatya. Plasma density analysis of cubesat wakes in the earth's ionosphere. Journal of Spacecraft and Rockets, 53(3):393–400, 2016.

[2] J. Allison, K. Amako, J. Apostolakis, P. Arce, M. Asai, T. Aso, E. Bagli, A. Bagulya, S. Banerjee, G. Barrand, B.R. Beck, A.G. Bogdanov, D. Brandt, J.M.C. Brown, H. Burkhardt, Ph. Canal, D. Cano-Ott, S. Chauvie, K. Cho, G.A.P. Cirrone, G. Cooperman, M.A. Cortés-Giraldo, G. Cosmo, G. Cuttone, G. Depaola, L. Desorgher, X. Dong, A. Dotti, V.D. Elvira, G. Folger, Z. Francis, A. Galoyan, L. Garnier, M. Gayer, K.L. Genser, V.M. Grichine, S. Guatelli, P. Guèye, P. Gumplinger, A.S. Howard, I. Hřivnáčová, S. Hwang, S. Incerti, A. Ivanchenko, V.N. Ivanchenko, F.W. Jones, S.Y. Jun, P. Kaitaniemi, N. Karakatsanis, M. Karamitros, M. Kelsey, A. Kimura, T. Koi, H. Kurashige, A. Lechner, S.B. Lee, F. Longo, M. Maire, D. Mancusi, A. Mantero, E. Mendoza, B. Morgan, K. Murakami, T. Nikitina, L. Pandola, P. Paprocki, J. Perl, I. Petrović, M.G. Pia, W. Pokorski, J.M. Quesada, M. Raine, M.A. Reis, A. Ribon, A. Ristić Fira, F. Romano, G. Russo, G. Santin, T. Sasaki, D. Sawkey, J.I. Shin, I.I. Strakovsky, A. Taborda, S. Tanaka, B. Tomé, T. Toshito, H.N. Tran, P.R. Truscott, L. Urban, V. Uzhinsky, J.M. Verbeke, M. Verderi, B.L. Wendt, H. Wenzel, D.H. Wright, D.M. Wright, T. Yamashita, J. Yarba, and H. Yoshida. Recent developments in geant4. Nuclear Instruments and Methods in Physics Research Section A: Accelerators, Spectrometers, Detectors and Associated Equipment, 835:186–225, 2016.

[3] Nesrine Amiour, Thami Zeghloul, Mohamed Sofiane Bendilmi, and Lucian Dascalescu. Comparison and calibration of four instruments for the measurement of electric potential at the surface of non-planar bodies. Journal of Electrostatics, 134:104041, 2025.

[4] KA Anderson, LM Chase, RP Lin, JE McCoy, and RE McGuire. Solar-wind and interplanetary electron measurements on the apollo 15 subsatellite. Journal of Geophysical Research, 77(25):4611–4626, 1972.

[5] Daria Andrievskaia, Ignacio Cáceres, Paolo Guardabasso, and Stéphanie Lizy-Destrez. Analysis of lunar impacts for orbital debris mitigation. In 73rd International Astronautical Congress (IAC), Paris, France: International Astronautical Federation, 2022.

[6] Mats André, Anders I. Eriksson, Yuri V. Khotyaintsev, and Sergio Toledo-Redondo. The spacecraft wake: Interference with electric field observations and a possibility to detect cold ions. Journal of Geophysical Research: Space Physics, 126(9):e2021JA029493, 2021.

[7] Vassilis Angelopoulos. The artemis mission. The ARTEMIS mission, pages 3–25, 2014.

[8] Roberto Armellin, Pierluigi Di Lizia, M Rasotto, G Di Mauro, and M Landgraf. Disposal strategies for spacecraft in lagrangian point orbits. In The 24th AAS/AIAA Space Flight Mechanics Meeting, pages 26–30, 2014.

[9] V S Aslanov. Dynamics and control of a two-spacecraft coulomb formation: Challenges and prospects. Journal of Physics: Conference Series, 1441(1):012084, jan 2020.

[10] Vladimir Aslanov and Hanspeter Schaub. Detumbling attitude control analysis considering an electrostatic pusher configuration. AIAA Journal of Guidance, Control, and Dynamics, 42(4):900–909, April 2019.

[11] Vladimir Aslanov and Vadim Yudintsev. Dynamics of large space debris removal using tethered space tug. Acta Astronautica, 91:149–156, 2013.

[12] Christopher Baker and Robert Bingham. Plasma lens for ion-beam focusing. In APS Division of Plasma Physics Meeting Abstracts, volume 2023, pages JO03–009, 2023.

[13] Brian Baker-McEvilly, Surabhi Bhadauria, David Canales, and Carolin Frueh. A comprehensive review on cislunar expansion and space domain awareness. Progress in Aerospace Sciences, 147:101019, 2024.

[14] S. J. Bame, J. R. Asbridge, H. E. Felthauser, E. W. Hones, and I. B. Strong. Characteristics of the plasma sheet in the earth's magnetotail. Journal of Geophysical Research (1896-1977), 72(1):113–129, 1967.

[15] Brad F. Barakat and Michael T. Kezirian. Establishing requirements for lunar and cislunar orbital debris tracking. Journal of Space Safety Engineering, 11(3):446–453, 2024. Space Debris: Update to The State of the Art.

[16] Michele Bechini, Marco B. Quadrelli, Michèle Lavagna, and Joseph J. Wang. Hovering of an electrically actuated spacecraft in a small-body plasma field. Journal of Spacecraft and Rockets, 58(5):1461–1476, 2021.

[17] M. Bengtson, J. Hughes, and H. Schaub. Prospects and challenges for touchless sensing of spacecraft electrostatic potential using electrons. IEEE Transactions on Plasma Science, 47(8):3673–3681, 2019.

[18] M. Bengtson, K. Wilson, J. Hughes, and H. Schaub. Survey of the electrostatic tractor research for reorbiting passive geo space objects. Astrodynamics, 2(4):291–305, Dec 2018.

[19] M. T. Bengtson, K. T. Wilson, and H. Schaub. Experimental results of electron method for remote spacecraft charge sensing. Space Weather, 18(3):1–12, 2020.

[20] Miles Bengtson and Hanspeter Schaub. Electron-based touchless potential sensing of shape primitives and differentially-charged spacecraft. AIAA Journal of Spacecraft and Rockets, 58(6):1847–1857, Nov. – Dec. 2021.

[21] Trevor Bennett and Hanspeter Schaub. Contactless electrostatic detumbling of axi-symmetric geo objects with nominal pushing or pulling. Advances in Space Research, 62(11), December 2018.

[22] Trevor Bennett, Daan Stevenson, Erik Hogan, Lauren McManus, and Hanspeter Schaub. Prospects and challenges of touchless debris despinning using electrostatics. Advances in Space Research, 56(3):557–568, Aug. 2015.

[23] John Berryman and Hanspeter Schaub. Analytical charge analysis for two- and three-craft coulomb formations. Journal of Guidance, Control, and Dynamics, 30(6):1701–1710, 2007.

[24] Rodger Biasca and Joseph Wang. Ion current collection in spacecraft wakes. Physics of Plasmas, 2(1):280–288, 01 1995.

[25] JW Bonnell, FS Mozer, GT Delory, AJ Hull, RE Ergun, CM Cully, V Angelopoulos, and PR Harvey. The electric field instrument (efi) for themis. The THEMIS mission, pages 303–341, 2009.

[26] N. Boone and R. Bettinger. Simulation of debris events in selected low lunar orbits. Astronautical Sciences, 70(16), 2023.

[27] Nathan R. Boone and Robert A. Bettinger. Efficient disposal of low lunar orbiters on the lunar surface. Journal of Space Safety Engineering, 12(1):195–205, 2025.

[28] Nathan R. Boone, Robert A. Bettinger, and Bryan D. Little. Simulation of debris events in cislunar orbits near the moon. Journal of Spacecraft and Rockets, 62(6):2030–2046, 2025.

[29] Joseph E Borovsky and Juan Alejandro Valdivia. The earth's magnetosphere: A systems science overview and assessment. Surveys in geophysics, 39(5):817–859, 2018.

[30] Graziella Branduardi-Raymont, Steve F Sembay, Jonathan P Eastwood, David G Sibeck, Tony A Abbey, Patrick Brown, Jenny A Carter, Chris M Carr, Colin Forsyth, Dhiren Kataria, et al. Axiom: Advanced x-ray imaging of the magnetosphere. Experimental Astronomy, 33(2):403–443, 2012.

[31] Thomas W Burgoyne and Gary M Hieftje. An introduction to ion optics for the mass spectrograph. Mass Spectrometry Reviews, 15(4):241–259, 1996.

[32] TM Burinskaya. Non-monotonic potentials above the day-side lunar surface exposed to the solar radiation. Planetary and Space Science, 115:64–68, 2015.

[33] C. J. Capon, M. Brown, and R. R. Boyce. Scaling of plasma-body interactions in low earth orbit. Physics of Plasmas, 24(4):042901, 2017.

[34] Fausto Casale, Hanspeter Schaub, and James Douglas Biggs. Lyapunov optimal touchless electrostatic detumbling of space debris in geo using a surface multisphere model. Journal of Spacecraft and Rockets, 58(3), May–June 2021.

[35] Kaylee Champion and Hanspeter Schaub. Electrostatic potential shielding in representative cislunar regions. IEEE Transactions on Plasma Science, 51(9):2482–2500, Sept. 2023.

[36] Kaylee Champion and Hanspeter Schaub. Feasibility of cislunar spacecraft wake generation. In AIAA SciTech, National Harbor, Maryland, January 23–28 2023.

[37] Kaylee Champion and Hanspeter Schaub. Electron beam properties for touchless potential sensing of complex geometry spacecraft. In AIAA Science and Technology Forum and Exposition (SciTech), Orlando, FL, Jan. 8–12 2024.

[38] Kaylee Champion and Hanspeter Schaub. Ion optics for laboratory spacecraft wake generation. In Spacecraft Charging and Technology Conference, Avignon, France, June 17–21 2024.

[39] Kaylee Champion and Hanspeter Schaub. Passive potential sensing in cislunar space: Simulations using nascap-2k and SPIS. In AAS Spaceflight Mechanics Meeting, Kauai, Hawaii, Jan. 19–23 2025. Paper No. AAS 25-151.

[40] Francis F Chen. Langmuir probe diagnostics. In IEEE-ICOPS Meeting, Jeju, Korea. Citeseer, 2003.

[41] M. S. Chung and T. E. Everhart. Simple calculation of energy distribution of low-energy secondary electrons emitted from metals under electron bombardment. Journal of Applied Physics, 45(2):707–709, 1974.

[42] H. K. Connor, D. G. Sibeck, M. R. Collier, I. I. Baliukin, G. Branduardi-Raymont, P. C. Brandt, N. Y. Buzulukova, Y. M. Collado-Vega, C. P. Escoubet, M.-C. Fok, S.-Y. Hsieh, J. Jung, S. Kameda, K. D. Kuntz, F. S. Porter, S. Sembay, T. Sun, B. M. Walsh, and J. H. Zoennchen. Soft x-ray and ena imaging of the earth's dayside magnetosphere. Journal of Geophysical Research: Space Physics, 126(3):e2020JA028816, 2021.

[43] Steve Creech, John Guidi, and Darcy Elburn. Artemis: an overview of nasa's activities to return humans to the moon. In 2022 ieee aerospace conference (aero), pages 1–7. IEEE, 2022.

[44] Stef P. Crum, Brian C. Gunter, and Mariel Borowitz. Cislunar orbit collision probability analysis. Journal of Spacecraft and Rockets, 62(5):1519–1527, 2025.

[45] Poul Dahl. Introduction to electron and ion optics. Elsevier, 2012.

[46] V. A. Davis, M. J. Mandell, D. C. Ferguson, and D. L. Cooke. Modeling of dmsp surface charging events. IEEE Transactions on Plasma Science, 45(8):1906–1914, 2017.

[47] VA Davis and MJ Mandell. Nascap-2k version 4.4 scientific documentation. 2020.

[48] Von P Debye and E." Hückel. Zur theorie der electrolyte. Phyikalishce Zeitschrift., pages 185–206, 1923.

[49] J Deca, G Lapenta, R Marchand, and Stefano Markidis. Spacecraft charging analysis with the implicit particle-in-cell code iPic3D. Physics of Plasmas, 20(10), 2013.

[50] M. H. Denton, M. F. Thomsen, H. Korth, S. Lynch, J. C. Zhang, and M. W. Liemohn. Bulk plasma properties at geosynchronous orbit. Journal of Geophysical Research: Space Physics, 110(A7), 2005.

[51] Dominique Drouin, Alexandre Réal Couture, Dany Joly, Xavier Tastet, Vincent Aimez, and Raynald Gauvin. Casino v2.42—a fast and easy-to-use modeling tool for scanning electron microscopy and microanalysis users. Scanning, 29(3):92–101, 2007.

[52] IW Drummond. The ion optics of low-energy ion beams. Vacuum, 34(1-2):51–61, 1984.

[53] Roger Dudziak, Sean Tuttle, and Simon Barraclough. Harpoon technology development for the active removal of space debris. Advances in Space Research, 56(3):509–527, 2015. Advances in Asteroid and Space Debris Science and Technology - Part 1.

[54] E. Engwall, A. I. Eriksson, M. André, I. Dandouras, G. Paschmann, J. Quinn, and K. Torkar. Low-energy (order 10 ev) ion flow in the magnetotail lobes inferred from spacecraft wake observations. Geophysical Research Letters, 33(6), 2006.

[55] E. Engwall, A. I. Eriksson, and J. Forest. Wake formation behind positively charged spacecraft in flowing tenuous plasmas. Physics of Plasmas, 13(6):062904, 06 2006.

[56] CL Enloe, DL Cooke, S Meassick, C Chan, and MF Tautz. Ion collection in a spacecraft wake: Laboratory simulations. Journal of Geophysical Research: Space Physics, 98(A8):13635–13644, 1993.

[57] R. E. Ergun, D. M. Malaspina, S. D. Bale, J. P. McFadden, D. E. Larson, F. S. Mozer, N. Meyer-Vernet, M. Maksimovic, P. J. Kellogg, and J. R. Wygant. Spacecraft charging and ion wake formation in the near-Sun environment. Physics of Plasmas, 17(7):072903, 07 2010.

[58] A.I. Eriksson and J.-E. Wahlund. Charging of the freja satellite in the auroral zone. IEEE Transactions on Plasma Science, 34(5):2038–2045, 2006.

[59] Anders I Eriksson, Yuri Khotyaintsev, and Per-Arne Lindqvist. Spacecraft wakes in the solar wind. In Proceedings of the 10th Spacecraft Charging Technology Conference, volume 6, pages 18–21, 2007.

[60] Dale C Ferguson. Extreme space weather spacecraft surface charging and arcing effects. In Extreme events in geospace, pages 401–418. Elsevier, 2018.

[61] Dale C. Ferguson, Jeremy Murray-Krezan, David A. Barton, J. R. Dennison, and Stephen A. Gregory. Feasibility of detecting spacecraft charging and arcing by remote sensing. Journal of Spacecraft and Rockets, 51(6):1907–1913, 2014.

[62] B. Feuerbacher and B. Fitton. Experimental investigation of photoemission from satellite surface materials. Journal of Applied Physics, 43(4):1563–1572, 1972.

[63] Sean Fuller, Emma Lehnhardt, Christina Zaid, and Kate Halloran. Gateway program status and overview. Journal of Space Safety Engineering, 9(4):625–628, 2022.

[64] N. Yu. Ganushkina, M. W. Liemohn, and S. Dubyagin. Current systems in the earth's magnetosphere. Reviews of Geophysics, 56(2):309–332, 2018.

[65] Henry B. Garrett and Albert C. Whittlesey. Spacecraft design guidelines. In Guide to Mitigating Spacecraft Charging Effects, chapter 3, pages 26–61. John Wiley & Sons, Ltd, 2012.

[66] J Geiss, P Eberhardt, F Bühler, J Meister, and P Signer. Apollo 11 and 12 solar wind composition experiments: Fluxes of he and ne isotopes. Journal of Geophysical Research, 75(31):5972–5979, 1970.

[67] Luke Goembel and John P. Doering. Instrument for measuring spacecraft potential. Journal of Spacecraft and Rockets, 35(1):66–72, 1998.

[68] Joseph I. Goldstein, Dale E. Newbury, Joseph R. Michael, Nicholas W. M. Ritchie, John Henry J. Scott, and David C. Joy. Backscattered Electrons. Springer New York, New York, NY, 2018.

[69] Manuel Grande, BJ Kellett, C Howe, CH Perry, B Swinyard, S Dunkin, Juhani Huovelin, Lauri Alha, LC D'uston, S Maurice, et al. The d-cixs x-ray spectrometer on the smart-1 mission to the moon—first results. Planetary and Space Science, 55(4):494–502, 2007.

[70] Zhai Guang and Zhang Jing-rui. Space tether net system for debris capture and removal. In 2012 4th International Conference on Intelligent Human-Machine Systems and Cybernetics, volume 1, pages 257–261, 2012.

[71] S. Guillemant, V. Génot, J.-C. Matéo-Vélez, R. Ergun, and P. Louarn. Solar wind plasma interaction with solar probe plus spacecraft. Annales Geophysicae, 30(7):1075–1092, 2012.

[72] Stanislas Guillemant, Vincent Génot, Jean-Charles Mateo Velez, Pierre Sarrailh, Alain Hilgers, and Philippe Louarn. Simulation study of spacecraft electrostatic sheath changes with the heliocentric distances from 0.044 to 1 au. IEEE Transactions on Plasma Science, 41(12):3338–3348, 2013.

[73] V Tz Gurovich, JZ Gleizer, Yu Bliokh, and Ya E Krasik. Potential distribution in an ion sheath of non-maxwellian plasma. Physics of plasmas, 13(7), 2006.

[74] S. Haaland, B. Lybekk, K. Svenes, A. Pedersen, M. Förster, H. Vaith, and R. Torbert. Plasma transport in the magnetotail lobes. Annales Geophysicae, 27(9):3577–3590, 2009.

[75] J. S. Halekas, G. T. Delory, R. P. Lin, T. J. Stubbs, and W. M. Farrell. Lunar prospector observations of the electrostatic potential of the lunar surface and its response to incident currents. Journal of Geophysical Research: Space Physics, 113(A9), 2008.

[76] J. S. Halekas, G. T. Delory, R. P. Lin, T. J. Stubbs, and W. M. Farrell. Lunar surface charging during solar energetic particle events: Measurement and prediction. Journal of Geophysical Research: Space Physics, 114(A5), 2009.

[77] J. S. Halekas, R. P. Lin, and D. L. Mitchell. Large negative lunar surface potentials in sunlight and shadow. Geophysical Research Letters, 32(9), 2005.

[78] JS Halekas, GT Delory, RP Lin, TJ Stubbs, and WM Farrell. Lunar prospector observations of the electrostatic potential of the lunar surface and its response to incident currents. Journal of Geophysical Research: Space Physics, 113(A9), 2008.

[79] J.S. Halekas, Y. Saito, G.T. Delory, and W.M. Farrell. New views of the lunar plasma environment. Planetary and Space Science, 59(14):1681–1694, 2011. Lunar Dust, Atmosphere and Plasma: The Next Steps.

[80] Julian Hammerl, Andrea L'opez, 'Alvaro Romero Calvo, and Hanspeter Schaub. Touchless potential sensing of differentially charged spacecraft using x-rays. Journal of Spacecraft and Rockets, 60(2):648–658, March–April 2023.

[81] Julian Hammerl and Hanspeter Schaub. Effects of electric potential uncertainty on electrostatic tractor relative motion control equilibria. Journal of Spacecraft and Rockets, 59(2):552–562, 2022.

[82] Julian Hammerl and Hanspeter Schaub. Coupled spacecraft charging due to continuous electron beam emission and impact. Journal of Spacecraft and Rockets, 61(5):1258–1271, 2024.

[83] Julian Hammerl and Hanspeter Schaub. Pulsed electron beam for electric potential sensing and control. In Spacecraft Charging and Technology Conference, Avignon, France, June 17–21 2024.

[84] Daoru Han, Joseph J. Wang, and Xiaoming He. Immersed finite element particle-in-cell simulations of plasma charging at the lunar terminator. Journal of Spacecraft and Rockets, 55(6):1490–1497, 2018.

[85] P. Harvey, E. Taylor, R. Sterling, and M. Cully. The themis constellation. Space Science Reviews, 141:117–152, 2008.

[86] Jennifer T. Heath, Chun-Sheng Jiang, and Mowafak M. Al-Jassim. Measurement of semiconductor surface potential using the scanning electron microscope. Journal of Applied Physics, 111(4):046103, 02 2012.

[87] S. L. G. Hess, P. Sarrailh, J.-C. Matéo-Vélez, B. Jeanty-Ruard, F. Cipriani, J. Forest, A. Hilgers, F. Honary, B. Thiébault, S. R. Marple, and D. Rodgers. New spis capabilities to simulate dust electrostatic charging, transport, and contamination of lunar probes. IEEE Transactions on Plasma Science, 43(9):2799–2807, 2015.

[88] SD Hester and Ain A Sonin. A laboratory study of the wakes of ionospheric satellites. AIAA Journal, 8(6):1090–1098, 1970.

[89] GD Hobbs and JA Wesson. Heat flow through a langmuir sheath in the presence of electron emission. Plasma Physics, 9(1):85, 1967.

[90] Erik Hogan and Hanspeter Schaub. Space weather influence on relative motion control using the touchless electrostatic tractor. Journal of Astronautical Sciences, 63(3):237–262, 2016.

[91] Erik A. Hogan and Hanspeter Schaub. Impacts of hot space plasma and ion beam emission on electrostatic tractor performance. IEEE Transactions on Plasma Science, 43(9):3115–3129, Sept. 2014.

[92] Erik A. Hogan and Hanspeter Schaub. Impacts of tug and debris sizes on electrostatic tractor charging performance. Advances in Space Research, 55(2):630–638, January 15 2015.

[93] Yuan Hu and Joseph Wang. Plasma wake simulation for charged space platforms: Fully kinetic pic versus hybrid pic. IEEE Transactions on Plasma Science, 47(8):3731–3738, 2019.

[94] Ziyu Huang and Joseph Wang. Modeling lunar surface charging under space weather conditions derived from the artemis and omni data. IEEE Transactions on Plasma Science, 2023.

[95] Joseph A. Hughes and Hanspeter Schaub. Heterogeneous surface multisphere models using method of moments foundations. Journal of Spacecraft and Rockets, 56(4):1259–1266, 2019.

[96] Joseph A. Hughes and Hanspeter Schaub. Electrostatic tractor analysis using a measured flux model. Journal of Spacecraft and Rockets, 57(2):207–216, 2020.

[97] A. J. Hundhausen. Composition and dynamics of the solar wind plasma. Reviews of Geophysics, 8(4):729–811, 1970.

[98] U. Isensee and H. Maassberg. Particle-in-cell simulation of the plasma environment of a spacecraft in the solar wind. Advances in Space Research, 1(2):413–416, 1981.

[99] Lee EZ Jasper and Hanspeter Schaub. Effective sphere modeling for electrostatic forces on a three-dimensional spacecraft shape. In AAS/AIAA Spaceflight Mechanics Meeting, Girdwood, Alaska, 2011.

[100] Esa Kallio and Gábor Facskó. Properties of plasma near the moon in the magnetotail. Planetary and Space Science, 115:69–76, 2015. Solar wind interaction with the terrestrial planets.

[101] Justin C Kasper, Robert Abiad, Gerry Austin, Marianne Balat-Pichelin, Stuart D Bale, John W Belcher, Peter Berg, Henry Bergner, Matthieu Berthomier, Jay Bookbinder, et al. Solar wind electrons alphas and protons (sweap) investigation: Design of the solar wind and coronal plasma instrument suite for solar probe plus. Space Science Reviews, 204(1):131–186, 2016.

[102] I. Katz, G. A. Jongeward, V. A. Davis, M. J. Mandell, R. A. Kuharski, J. R. Lilley Jr., W. J. Raitt, D. L. Cooke, R. B. Torbert, G. Larson, and D. Rau. Structure of the bipolar plasma sheath generated by spear i. Journal of Geophysical Research: Space Physics, 94(A2):1450–1458, 1989.

[103] Lyon B. King, Gordon G. Parker, Satwik Deshmukh, and Jer-Hong Chong. Study of inter-spacecraft coulomb forces and implications for formation flying. Journal of Propulsion and Power, 19(3):497–505, 2003.

[104] Shoji Kitamura, Yukio Hayakawa, and Satomi Kawamoto. A reorbiter for large geo debris objects using ion beam irradiation. Acta Astronautica, 94(2):725–735, 2014.

[105] William C Knudsen, Karl Spenner, Jack Bakke, and Vit Novak. Pioneer venus orbiter planar retarding potential analyzer plasma experiment. IEEE Transactions on Geoscience and Remote Sensing, (1):54–59, 2007.

[106] HC Koons, JE Mazur, RS Selesnick, JB Blake, and JF Fennell. The impact of the space environment on space systems. Technical report, The Aerospace Corporation, 1999.

[107] V. I. Krassovsk. Exploration of the upper atmosphere with the help of the third soviet sputnik. Proceedings of the IRE, 47(2):289–296, 1959.

[108] Säm Krucker, Martin Bednarzik, Oliver Grimm, Gordon J Hurford, Olivier Limousin, Aline Meuris, Piotr Orleański, Karol Seweryn, and Konrad R Skup. The spectrometer/telescope for imaging x-rays on solar orbiter: Flight design, challenges and trade-offs. Nuclear Instruments and Methods in Physics Research Section A: Accelerators, Spectrometers, Detectors and Associated Equipment, 824:626–629, 2016.

[109] Shu T. Lai. An improved langmuir probe formula for modeling satellite interactions with near-geostationary environment. Journal of Geophysical Research: Space Physics, 99(A1):459–467, 1994.

[110] Shu T. Lai. Fundamentals of Spacecraft Charging: Spacecraft Interactions with Space Plasmas. Princeton University Press, 2012.

[111] Shu T. Lai, Herbert A. Cohen, Thomas L. Aggson, and William J. McNeil. The effect of photoelectrons on boom-satellite potential differences during electron beam ejection. Journal of Geophysical Research: Space Physics, 92(A11):12319–12325, 1987.

[112] Shu T. Lai and Catherine Miller. Retarding potential analyzer: Principles, designs, and space applications. AIP Advances, 10(9):095324, 2020.

[113] S.T. Lai and M.F. Tautz. Aspects of spacecraft charging in sunlight. IEEE Transactions on Plasma Science, 34(5):2053–2061, 2006.

[114] RM Langford, AK Petford-Long, and Peter Gnauck. Focused ion beam based sample preparation techniques. Microscopy and Microanalysis, 8(S02):46–47, 2002.

[115] Micah LaPointe, Benedikt Esser, Ivan Aponte, Zachary Cardenas, James Dickens, John Mankowski, Jacob Stephens, Donald Friesen, Crystal Nelson, Neil Koone, David Hattz, and Andreas Neuber. Surface charge distribution mapping using an electrostatic probe. In 2021 IEEE Pulsed Power Conference (PPC), pages 1–5, 2021.

[116] Martin Lara. Design of long-lifetime lunar orbits: A hybrid approach. Acta Astronautica, 69(3):186–199, 2011.

[117] Frank B Leahy. SLS-SPEC-159, cross-program design specification for natural environments (DSNE). Technical report, National Aeronautics and Space Administration, 2021.

[118] Ronald G. Lee, Erica S. Worthy, Emily M. Willis, Gary L. Brown, Fabrice Cipriani, and Donald C. Barker. Development of a comprehensive physics-based model for study of nasa gateway lunar dust contamination. Acta Astronautica, 210:616–626, 2023.

[119] Chunlai Li, Hao Hu, Meng-Fei Yang, Jianjun Liu, Qin Zhou, Xin Ren, Bin Liu, Dawei Liu, Xingguo Zeng, Wei Zuo, Guangliang Zhang, Hongbo Zhang, Saihong Yang, Qiong Wang, Xiangjin Deng, Xingye Gao, Yan Su, Weibin Wen, and Ziyuan Ouyang. Nature of the lunar farside samples returned by the Chang'E-6 mission. National Science Review, page nwae328, 09 2024.

[120] Peixuan Li, Noah Hershkowitz, and Gregory Severn. Building langmuir probes and emissive probes for plasma potential measurements in low pressure, low temperature plasmas. JoVE, (171):e61804, 2021.

[121] D. R. Lide. CRC Handbook of Chemistry and Physics: 84th Edition. CRC Press, 2003.

[122] Helmut Liebl. Applied charged particle optics, volume 2012. Springer, 2008.

[123] Mingpei Lin and Ming Xu. Charged-spacecraft formation: Concept, deployment and coulomb-force control. IEEE Access, 8:59670–59677, 2020.

[124] G. Livadiotis. Collision frequency and mean free path for plasmas described by kappa distributions. AIP Advances, 9(10):105307, 2019.

[125] Robert B Lobbia and Brian E Beal. Recommended practice for use of langmuir probes in electric propulsion testing. Journal of Propulsion and Power, 33(3):566–581, 2017.

[126] Andrea L'opez, Julian Hammerl, and Hanspeter Schaub. Detecting space objects with binary wide field of view x-ray sensing. In AAS Astrodynamics Specialist Conference, Charlotte, NC, Aug. 7–10 2022. Paper No. AAS 22-602.

[127] E. A. Lucek, D. Constantinescu, M. L. Goldstein, J. Pickett, J. L. Pinçon, F. Sahraoui, R. A. Treumann, and S. N. Walker. The magnetosheath. Space Science Reviews, 118:95–152, 2005.

[128] Myron J Mandell, Victoria A Davis, David L Cooke, Adrian T Wheelock, and Christopher J Roth. Nascap-2k spacecraft charging code overview. IEEE Transactions on Plasma Science, 34(5):2084–2093, 2006.

[129] RA Masterson, Mark Chodas, Laura Bayley, Branden Allen, J Hong, Pronoy Biswas, Conor McMenamin, Kevin Stout, Ed Bokhour, Harrison Bralower, et al. Regolith x-ray imaging spectrometer (rexis) aboard the osiris-rex asteroid sample return mission. Space Science Reviews, 214(1):48, 2018.

[130] S Mathavaraj and Kuldeep Negi. Chandrayaan-3 trajectory design: Injection to successful landing. Journal of Spacecraft and Rockets, pages 1–8, 2024.

[131] Jordan Maxwell, Andrew Harris, and Hanspeter Schaub. Balancing differential drag with coulomb repulsion in low earth orbit plasma wakes. Acta Astronautica, 194:323–333, March 2022.

[132] Jordan Maxwell and Hanspeter Schaub. Low earth orbit plasma wake shaping and applications to on-orbit proximity operations. IEEE Transactions on Plasma Science, 47(10):4760–4769, 2019.

[133] Jordan Maxwell and Hanspeter Schaub. Charge-product control approach to electrostatic leader-follower in leo plasma wakes. Advances in Space Research, 67(1):3478–3488, June 2021.

[134] Matthew McCollum, Emily Willis, and Anne Diekmann. Artemis IV Docking in Radiation Belt Charging Environment. Huntsville, AL, August 2023.

[135] D McComas, F Allegrini, F Bagenal, P Casey, P Delamere, D Demkee, G Dunn, H Elliott, J Hanley, K Johnson, et al. The solar wind around pluto (swap) instrument aboard new horizons. Space Science Reviews, 140(1):261–313, 2008.

[136] JP McFadden, CW Carlson, D Larson, M Ludlam, R Abiad, B Elliott, P Turin, M Marckwordt, and V Angelopoulos. The themis esa plasma instrument and in-flight calibration. Space Science Reviews, 141(1):277–302, 2008.

[137] Melissa L McGuire, Steven L McCarty, and Laura M Burke. Power and propulsion element (ppe) spacecraft reference trajectory document. Technical report, NASA, May 2020.

[138] James Meador. Long-term orbit stability of the apollo 11 "eagle" lunar module ascent stage. Planetary and Space Science, 205:105304, 2021.

[139] C-I Meng and JD Mihalov. Average plasma-sheet configuration near 60 earth radii. Journal of Geophysical Research, 77(10):1739–1755, 1972.

[140] WJ Miloch, VV Yaroshenko, SV Vladimirov, HL Pécseli, and J Trulsen. Spacecraft charging in flowing plasmas; numerical simulations. In Journal of Physics: Conference Series, volume 370, page 012004. IOP Publishing, 2012.

[141] IG Mitrofanov, LM Zelenyi, VI Tret'yakov, and DV Kalashnikov. Luna-25: The first polar mission to the moon. Solar System Research, 55:485–495, 2021.

[142] Y Miyake, CM Cully, H Usui, and H Nakashima. Plasma particle simulations of wake formation behind a spacecraft with thin wire booms. Journal of Geophysical Research: Space Physics, 118(9):5681–5694, 2013.

[143] Naomi Murdoch, Dario Izzo, Claudio Bombardelli, Ian Carnelli, Alain Hilgers, and David Rodgers. Electrostatic tractor for near earth object deflection. In 59th International Astronautical Congress, volume 29, 2008.

[144] Mohamed Nassif, Collin Deans, and Ben Reed. Evaluating disposal and end-of-life strategies for cislunar and lunar missions to enable sustainable exploration. In AIAA SCITECH 2025 Forum, Jan. 2025.

[145] Norman F Ness. Interaction of the solar wind with the moon. In Solar-Terrestrial Physics/1970, pages 347–393. Springer, 1972.

[146] T. Nie and P. Gurfil. Lunar frozen orbits revisited. Celestial Mechanics and Dynamical Astronomy, 130(61), 2018.

[147] K. W. Ogilvie and M. A. Coplan. Solar wind composition. Reviews of Geophysics, 33(S1):615–622, 1995.

[148] K.W. Ogilvie and M.D. Desch. The wind spacecraft and its early scientific results. Advances in Space Research, 20(4):559–568, 1997. Results of the IASTP Program.

[149] L Olano and I Montero. Energy spectra of secondary electrons in dielectric materials by charging analysis. Results in Physics, 19:103456, 2020.

[150] WA Oran, Uri Samir, Nobie H Stone, and EG Fontheeim. Laboratory observations of electron temperature in the wake of a sphere in a streaming plasma. Planetary and Space Science, 23(7):1081–1083, 1975.

[151] Mikhail Ovchinnikov, Maksim Shirobokov, and Sergey Trofimov. Lunar satellite constellations in frozen low orbits. Aerospace, 11(11), 2024.

[152] LW Parker. Plasmasheath-photosheath theory for large high-voltage space structures. Space Systems and Their Interactions with Earth's Space Environment, Editors, HB Garrett and CP Pike, Progress in Astronautics and Aeronautics, 71:477–522, 1980.

[153] Andrew Poppe, Jasper S. Halekas, and Mihály Horányi. Negative potentials above the dayside lunar surface in the terrestrial plasma sheet: Evidence of non-monotonic potentials. Geophysical Research Letters, 38(2), 2011.

[154] Marco B. Quadrelli, Henry Garrett, Julie Castillo, Adrian Stoica, Masahiro Ono, Caleb Christianson, Dario Lusso, and Hanspeter Schaub. Active electrostatic flight for airless bodies. In 2017 IEEE Aerospace Conference, pages 1–16, 2017.

[155] John Ashworth Ratcliffe. An introduction to ionosphere and magnetosphere. CUP Archive, 1972.

[156] Santwana Raychaudhuri, Jacqueline Hill, Hong Young Chang, Eugene K. Tsikis, and Karl E. Lonngren. An experiment on the plasma expansion into a wake. The Physics of Fluids, 29(1):289–293, 01 1986.

[157] W. Riedler, K. Torkar, F. Rüdenauer, M. Fehringer, A. Pedersen, R. Schmidt, R. J. L. Grard, H. Arends, B. T. Narheim, J. Troim, R. Torbert, R. C. Olsen, E. Whipple, R. Goldstein, N. Valavanoglou, and Hua Zhao. Active Spacecraft Potential Control, pages 271–302. Springer Netherlands, Dordrecht, 1997.

[158] Ralph Roe. Mitigating In-Space Charging Effects-A Guideline. National Aeronautics and Space Administration, June 2022.

[159] 'Alvaro Romero Calvo, Kaylee Champion, and Hanspeter Schaub. Enabling ultraviolet lasers for touchless spacecraft potential sensing. IEEE Transactions on Plasma Science, 51(9):2468–2481, Sept. 2023.

[160] Álvaro Romero Calvo, Julian Hammerl, and Hanspeter Schaub. Touchless potential sensing of complex differentially-charged shapes using secondary electrons. AIAA Journal of Spacecraft and Rockets, 59(5):1623–1633, Sept. – Oct. 2022.

[161] Allen G. Rubin and Arthur Besse. Charging of a manned maneuvering unit in the shuttle wake. Journal of Spacecraft and Rockets, 23(1):122–124, 1986.

[162] C.M. Saaj, V. Lappas, H. Schaub, and D. Izzo. Hybrid propulsion system for formation flying using electrostatic forces. Aerospace Science and Technology, 14(5):348–355, 2010.

[163] Alberto A. Sagüés and Michael T. Walsh. Kelvin probe electrode for contactless potential measurement on concrete – properties and corrosion profiling application. Corrosion Science, 56:26–35, 2012.

[164] Trinesh Sana and SK Mishra. Plasma sheath around chandrayaan-3 landing site: A case study. The Planetary Science Journal, 4(9):158, 2023.

[165] N. L. Sanders and G. T. Inouye. Secondary emission effects on spacecraft charging: Energy distribution considerations. In Spacecraft Charging and Technology Conference, pages 747–755, 1978. NASA-2071, ADA-084626.

[166] Pierre Sarrailh, Jean-Charles Matéo-Vélez, Sébastien L. G. Hess, Jean-François Roussel, Benoit Thiébault, Julien Forest, Benjamin Jeanty-Ruard, Alain Hilgers, David Rodgers, Fabrice Cipriani, and Denis Payan. Spis 5: New modeling capabilities and methods for scientific missions. IEEE Transactions on Plasma Science, 43(9):2789–2798, 2015.

[167] Miroslava Schaffer, Julia Mahamid, Benjamin D Engel, Tim Laugks, Wolfgang Baumeister, and Jürgen M Plitzko. Optimized cryo-focused ion beam sample preparation aimed at in situ structural studies of membrane proteins. Journal of structural biology, 197(2):73–82, 2017.

[168] Hanspeter Schaub and Lee E. Z. Jasper. Orbit boosting maneuvers for two-craft coulomb formations. AIAA Journal of Guidance, Control, and Dynamics, 36(1):74–82, Jan. – Feb. 2013.

[169] Hanspeter Schaub and Daniel F. Moorer. Geosynchronous large debris reorbiter: Challenges and prospects. The Journal of the Astronautical Sciences, 59(1):161–176, Jun 2012.

[170] Hanspeter Schaub, Gordon G. Parker, and Lyon B. King. Challenges and prospect of coulomb formations. Journal of the Astronautical Sciences, 52(1–2):169–193, Jan.–June 2004.

[171] Hanspeter Schaub and Zolt'an Sternovsky. Active space debris charging for contactless electrostatic disposal maneuvers. Advances in Space Research, 43(1):110–118, 2014.

[172] Charles E Schlemm, Richard D Starr, George C Ho, Kathryn E Bechtold, Sarah A Hamilton, John D Boldt, William V Boynton, Walter Bradley, Martin E Fraeman, Robert E Gold, et al. The x-ray spectrometer on the messenger spacecraft. Space Science Review, pages 393–415, 2007.

[173] R. Schmidt, H. Arends, A. Pedersen, F. Rüdenauer, M. Fehringer, B. T. Narheim, R. Svenes, K. Kvernsveen, K. Tsuruda, T. Mukai, H. Hayakawa, and M. Nakamura. Results from active spacecraft potential control on the geotail spacecraft. Journal of Geophysical Research: Space Physics, 100(A9):17253–17259, 1995.

[174] JJ Scholtz, D Dijkkamp, and RWA Schmitz. Secondary electron emission properties. Philips journal of research, 50(3-4):375–389, 1996.

[175] Carl R Seubert, Laura A Stiles, and Hanspeter Schaub. Effective coulomb force modeling for spacecraft in earth orbit plasmas. Advances in Space Research, 54(2):209–220, 2014.

[176] Minghe Shan, Jian Guo, and Eberhard Gill. Deployment dynamics of tethered-net for space debris removal. Acta Astronautica, 132:293–302, 2017.

[177] Shuangyan Shen, Xing Jin, and Chang Hao. Cleaning space debris with a space-based laser system. Chinese Journal of Aeronautics, 27(4):805–811, 2014.

[178] Alexander Sjogren, Anders I Eriksson, and Christopher M Cully. Simulation of potential measurements around a photoemitting spacecraft in a flowing plasma. IEEE Transactions on Plasma Science, 40(4):1257–1261, 2012.

[179] Daan Stevenson and Hanspeter Schaub. Multi-sphere method for modeling spacecraft electrostatic forces and torques. Advances in Space Research, 51(1):10 – 20, 2013.

[180] Daan Stevenson and Hanspeter Schaub. Optimization of sphere population for electrostatic multi sphere model. IEEE Transactions on Plasma Science, 41(12):3526–3535, Dec. 2013.

[181] Laura A. Stiles, Hanspeter Schaub, Kurt K. Maute, and Daniel F. Moorer. Electrostatically inflated gossamer space structure voltage requirements due to orbital perturbations. Acta Astronautica, 84:109–121, 2013.

[182] KR Svencs and J Trøim. Laboratory simulation of vehicle-plasma interaction in low earth orbit. Planetary and space science, 42(1):81–94, 1994.

[183] Miklos Szilagyi. Electron and ion optics. Springer Science & Business Media, 2012.

[184] Stephen Taller, David Woodley, Elizabeth Getto, Anthony M Monterrosa, Zhijie Jiao, Ovidiu Toader, Fabian Naab, Thomas Kubley, Shyam Dwaraknath, and Gary S Was. Multiple ion beam irradiation for the study of radiation damage in materials. Nuclear Instruments and Methods in Physics Research Section B: Beam Interactions with Materials and Atoms, 412:1–10, 2017.

[185] B Thiébault, A Hilgers, E Sasot, H Laakso, P Escoubet, Vincent Génot, and J Forest. Potential barrier in the electrostatic sheath around a magnetospheric spacecraft. Journal of Geophysical Research: Space Physics, 109(A12), 2004.

[186] Benoit Thiebault, Benjamin Jeanty-Ruard, Pierre Souquet, Julien Forest, Jean-Charles Mateo-Velez, Pierre Sarrailh, David Rodgers, Alain Hilgers, Fabrice Cipriani, Denis Payan, et al. Spis 5.1: An innovative approach for spacecraft plasma modeling. IEEE Transactions on Plasma Science, 43(9):2782–2788, 2015.

[187] K. Torkar, H. Arends, W. Baumjohann, C. P. Escoubet, A. Fazakerley, M. Fehringer, G. Fremuth, H. Jeszenszky, G. Laky, B. T. Narheim, W. Riedler, F. Rüdenauer, W. Steiger, K. Svenes, and H. Zhao. Spacecraft potential control for double star. Annales Geophysicae, 23(8):2813–2823, 2005.

[188] K Torkar, R Nakamura, Martin Tajmar, C Scharlemann, H Jeszenszky, G Laky, G Fremuth, CP Escoubet, and K Svenes. Active spacecraft potential control investigation. Space Science Reviews, 199:515–544, 2016.

[189] K. Torkar, W. Riedler, C. P. Escoubet, M. Fehringer, R. Schmidt, R. J. L. Grard, H. Arends, F. Rüdenauer, W. Steiger, B. T. Narheim, K. Svenes, R. Torbert, M. André, A. Fazakerley, R. Goldstein, R. C. Olsen, A. Pedersen, E. Whipple, and H. Zhao. Active spacecraft potential control for cluster – implementation and first results. Annales Geophysicae, 19(10/12):1289–1302, 2001.

[190] David Tskhakaya, Konstantin Matyash, Ralf Schneider, and Francesco Taccogna. The particle-in-cell method. Contributions to Plasma Physics, 47(8-9):563–594, 2007.

[191] Satoshi Ueda, Takahiro Ito, and Shin-ichiro Sakai. A study on guidance technique for precise lunar landing. Proceedings of 31st ISTS, 2017.

[192] Richard Vondrak, John Keller, Gordon Chin, and James Garvin. Lunar reconnaissance orbiter (lro): Observations for lunar exploration and science. Space science reviews, 150:7–22, 2010.

[193] James D. Walker, Sebastian Hampl, and Hanspeter Schaub. Development of Experimental Methods for Active Charge Control Using Combined Remote Sensing Methods, May 2025.

[194] James D. Walker and Hanspeter Schaub. Electron gun-based active charge control of nearby spacecraft. IEEE Transactions on Plasma Science, 53(12):3756–3770, Dec. 2025.

[195] Jiong Wang and DE Hastings. Ionospheric plasma flow over large high-voltage space platforms. i: Ion-plasma–time scale interactions of a plate at zero angle of attack. Physics of Fluids B: Plasma Physics, 4(6):1597–1614, 1992.

[196] Joseph Wang and DE Hastings. Ionospheric plasma flow over large high-voltage space platforms. ii: The formation and structure of plasma wake. Physics of Fluids B: Plasma Physics, 4(6):1615–1629, 1992.

[197] Joseph Wang and Ziyu Huang. Multiscale numerical simulations of plasma charging effects for astronaut at the lunar terminator. IEEE Transactions on Plasma Science, 51(9):2561–2570, 2023.

[198] Joseph Wang, P Leung, H Garrett, and G Murphy. Multibody-plasma interactions-charging in the wake. Journal of Spacecraft and Rockets, 31(5):889–894, 1994.

[199] X Wang, H-W Hsu, and M Horányi. Identification of when a langmuir probe is in the sheath of a spacecraft: The effects of secondary electron emission from the probe. Journal of Geophysical Research: Space Physics, 120(4):2428–2437, 2015.

[200] X Wang, J Pilewskie, H-W Hsu, and M Horányi. Plasma potential in the sheaths of electron-emitting surfaces in space. Geophysical Research Letters, 43(2):525–531, 2016.

[201] Emily Willis, Anne Diekmann, and Michael Guy. Plasma charging of crewed spacecraft in lunar orbit. In Space Environment Engineering and Science Applications Workshop, Laurel, MD, September 2022.

[202] K. T. Wilson, M. T. Bengtson, and H. Schaub. X-ray spectroscopic determination of electrostatic potential and material composition for spacecraft: Experimental results. Space Weather, 18(4):e2019SW002342, 2020.

[203] Kieran Wilson, Álvaro Romero-Calvo, and Hanspeter Schaub. Constrained guidance for spacecraft proximity operations under electrostatic perturbations. Journal of Spacecraft and Rockets, 0(0):1–13, 2022. *in press.*

[204] Kieran Wilson, Álvaro Romero-Calvo, Miles Bengtson, Julian Hammerl, Jordan Maxwell, and Hanspeter Schaub. Development and characterization of the eclips space environments simulation facility. Acta Astronautica, 194:48–58, 2022.

[205] Kieran T. H. Wilson, Miles Bengtson, and Hanspeter Schaub. Remote electrostatic potential sensing for proximity operations: Comparison and fusion of methods. Journal of Spacecraft and Rockets, 59(5):1425–1436, Sept. – Oct. 2022.

[206] Kieran T. H. Wilson, Julian Hammerl, and Hanspeter Schaub. Using plasma-induced x-ray emission to estimate electrostatic potentials on nearby space objects. Journal of Spacecraft and Rockets, 59(4):1402–1405, July–Aug. 2022.

[207] Kieran T. H. Wilson and Hanspeter Schaub. X-ray spectroscopy for electrostatic potential and material determination of space objects. IEEE Transactions on Plasma Science, 47(8):3858–3866, Aug. 2019.

[208] Kieran T. H. Wilson and Hanspeter Schaub. Impact of electrostatic perturbations on proximity operations in high earth orbits. AIAA Journal of Spacecraft and Rockets, 58(5):1293–1302, Sept. – Oct. 2021.

[209] Hermann Wollnik. Ion optics in mass spectrometers. Journal of mass spectrometry, 34(10):991–1006, 1999.

[210] Mikhail Yavor. Chapter 6 electrostatic energy analyzers. In Optics of Charged Particle Analyzers, volume 157 of Advances in Imaging and Electron Physics, pages 213–258. Elsevier, 2009.

[211] William Yu, Joseph Wang, and Kevin Chou. Laboratory measurement of lunar regolith simulant surface charging in a localized plasma wake. IEEE Transactions on Plasma Science, 43(12):4175–4181, 2015.

[212] Yanwen Zhang, Miguel L Crespillo, Haizhou Xue, Ke Jin, Chien-Hung Chen, CRISTIANO LINO Fontana, Joseph T Graham, and William J Weber. New ion beam materials laboratory for materials modification and irradiation effects research. Nuclear Instruments and Methods in Physics Research Section B: Beam Interactions with Materials and Atoms, 338:19–30, 2014.

[213] Hua Zhao, R Schmidt, CP Escoubet, K Torkar, and W Riedler. Self-consistent determination of the electrostatic potential barrier due to the photoelectron sheath near a spacecraft. Journal of Geophysical Research: Space Physics, 101(A7):15653–15659, 1996.

[214] Jianxun Zhao, Xinpeng Wei, Xiaoping Du, Xiaoming He, and Daoru Han. Photoelectron sheath and plasma charging on the lunar surface: Semianalytic solutions and fully-kinetic particle-in-cell simulations. IEEE Transactions on Plasma Science, 49(10):3036–3050, 2021.

[215] E Zinner, RM Walker, J Borg, and M Maurette. Measurement of heavy solar wind particles during the apollo 17 mission. In Conference on Solar Wind Three 3, pages 27–32. Non Mentionne, 1974.